Development of Novel Π-conjugated Polymer Semiconductors for Organic Solar Cells

by

Han Meng

A thesis
presented to the University of Waterloo
in fulfillment of the
thesis requirement for the degree of
Master of Applied Science
in
Chemical Engineering

Waterloo, Ontario, Canada, 2018

AUTHOR'S DECLARATION

I hereby declare that I am the sole author of this thesis. This is a true copy of the thesis, including any required final revisions, as accepted by my examiners.

I understand that my thesis may be made electronically available to the public.

Abstract

Bulk heterojunction polymer solar cell (PSC) is a promising photovoltaic technology for clean and renewable energy sources due to its superior advantages such as mechanical flexibility, light weight, low-cost fabrication, and large-area manufacturing compatibility. In this work, two classes of polymers, PzDP and TPT based polymers, were designed and synthesized for the application of PSC. Firstly, two copolymers PzDP24-T and PzDP16-BDT were prepared via Stille-coupling polymerization, which exhibited narrow bandgaps and low-lying energy levels. The PzDP24-T polymer showed n-type dominant charge transport properties with electron mobility up to 2.9×10^{-2} cm^2 V^{-1}, whereas PzDP16-BDT exhibited ambipolar charge transport behavior with balanced electron/hole mobilities up to 2.2×10^{-3} cm^2 V^{-1} s^{-1}/2.5×10^{-3} cm^2 V^{-1} s^{-1} in OTFTs. These PzDP-based polymers were then used as acceptor with PTB7-Th as the donor in all-PSCs. The PzDP24-T/PTB7-Th devices showed relatively low power conversion efficiency (PCE) (~ 0.3%), which caused poor morphology because of insufficient solubility. After the optimization of the backbone structure to PzDP16-BDT, the PCE of PzDP16-BDT/PTB7-Th based devices improved to 1.57%. On the other hand, the inferior bulk charge transport properties for PzDP-based polymers limited the overall PCEs. Secondly, a novel pyridazine-based conjugated monomer TPT was synthesized and incorporated into D-A copolymer (TPT-BDT). Compared to the analogue pyridine-based polymers, the TPT-BDT polymer showed a similar or deeper energy levels of -3.66 eV/-5.55 eV, which suggested the utilization of pyridazine can efficiently modulate the HOMO and LUMO. However, the TPT-BDT showed no performance for hole/electron mobilities in OTFTs due to highly twisted backbone. In addition, as the pyridazine is a ligand of palladium catalyst, the molecular weight of the polymer is low (~ 10 kDa). The relatively low molecular weight is found to be the reason of the severe PCEs (~ 0.11%) for TPT-BDT/$PC_{61}BM$ solar cells.

Acknowledgements

I would like to thank my supervisors, Dr. Yuning Li and Dr. Bo Cui. Their patient guidance and valuable advices allow me to develop my research skills and gain advancement in the last two years.

In addition, I would like to thank Dr. Bill O'Keefe and Dr. Romain Perrier-Cornet from Canadian General-Tower (CGT) for their valuable technical advice. I would also thank the Ontario Centre of Excellence (OCE), the Natural Sciences and Engineering Research Council (NSERC) of Canada, and CGT for the financial support for this work.

I am very much thankful for Yinghui He, who taught me all the organic synthesis skills. Special thanks go to Xiaocheng Zhou and Zhifang Zhang, who helped me for testing the solar cell devices. I also thank Arthur Hendsbee and Jenner Ngai, who supported me for OTFT devices, AMF and XRD measurement, as well as useful suggestions for my synthetic challenges.

Finally, I would like to thank my family and friends for their permanent support.

Table of Contents

List of Figures

List of Table

List of Scheme

List of Symbols

e: elementary charge, 1.60218×10^{-19} C

FF: fill factor

J_{SC}: short-circuit current

L: channel length

M_n: numerical average molecular weight

PCE: power conversion efficiency

R_S: series resistance

R_{SH}: shunt resistance

V_{OC}: open-circuit voltage

V_{TH}: threshold voltage

V_G: gate voltage

V_{DS}: drain-source voltage

μ: charge carrier mobility

W: width, gate width

List of Abbreviations

AFM	Atomic Force Microscopy
BGBC	Bottom Gate Bottom Contact
CB	Chlorobenzene
CV	Cyclic Voltammetry
D-A	Donor-Acceptor
DDTS	Dodecyl trichlorosilane
DFT	Density Functional Theory
GPC	Gel Permeation Chromatography
HOMO	Highest Occupied Molecular Orbital
LUMO	Lowest Unoccupied Molecular Orbital
NBS	N-Bromosuccinimide
o-DCB	o-dichlorobenzene
OFET	Organic Field Effect Transistor
OPV	Organic Photovoltaics
OTFT	Organic Thin Film Transistor
OSC	Organic Solar Cell
PDI	Polydispersity Index
RMS	Root Mean Square
TGBC	Top Gate Bottom Contact
UV-Vis	Ultraviolet-Visible
XRD	X-ray Diffraction

Other abbreviations and symbols are defined in the text.

Chapter 1 Introduction

1.1 Research Background

Today fossil fuels still dominate the energy consumption in the world (**Figure 1-1**). As non-renewable sources, once fossil fuels are consumed, they will not be replenished.[1] Furthermore, burning fossil fuels accounts for the majority of the emitted carbon dioxide, causing serious environmental problems such as global warming. Thus, it is urgent to explore a sustainable and environmentally friendly energy source.[2] Solar energy, as a renewable, clean and abundant source of energy, becomes a trending topic in the past decades.[3] The utilization of solar power is essential for us to respond to the exhaustion of petroleum and coal as well as environmental problems.[4]

One of the important solar energy conversion approaches is the solar cell technology (**Figure 1-2**). A solar cell consists of a semiconductor device that absorbs solar light and converts it into electric current directly.[5] Since the first solar cell was created by Charles Fritts in 1883,[6] significant progress has been made in the development and commercialization of solar cells particularly in the very recent years. Nowadays, solar cells can be classified into three types according to generation:[7] The first generation of solar cells are made of crystalline silicon which are the most popular one in the market due to its good performance and high stability[8], for example, Keiichiro Masuko achieved a conversion efficiency of 25% for crystalline silicon-based solar cells in 2014.[9] However, high manufacturing cost of crystalline silicon is a challenge for the development of crystalline silicon solar panels.[10] The second generation of solar cells are thin film solar cells, which are based on amorphous silicon, copper indium gallium diselenium (CIGS) and cadmium sulphide (CdTe). Compared to the first generation solar cells, thin film solar cells have a lower production cost because of lower material consumption of thin film and replacement of expensive silicon wafers.[11] However, thin film solar cells generally exhibit half the efficiency of crystalline-based solar cells.[12] The third generation of solar cells typically use many solution processable materials, such as organic materials (small molecules or polymers) and inorganic substances (CdTe, for instance), relating to a variety of thin film technologies. Although, at present, the third generation of solar panels

are still in research field, they have already showed great potential for the future of solar energy.[13] Organic solar cells or organic photovoltaics (OPVs), above all, offer a variety of outstanding features: Firstly, the solution processability enables organic solar cells to be produced in a simple, continuous and large-scale process by using printing tools.[14] On the other hand, solution processed solar cells are less costly than inorganic solar cells since their manufacture can avoid some high energy methods such as vacuum deposition.[15] Secondly, organic solar cells are suitable for portative electronic devices in special applications (such as aerospace), because light weight and flexibility are typical nature advantages for most organic materials.[16] Thirdly, the raw materials of organic solar cells are various, so organic solar panels' structures can be designed to adapt to different applications. Hence, those features give organic solar cells a promising prospect and may revolutionize the future of solar energy.

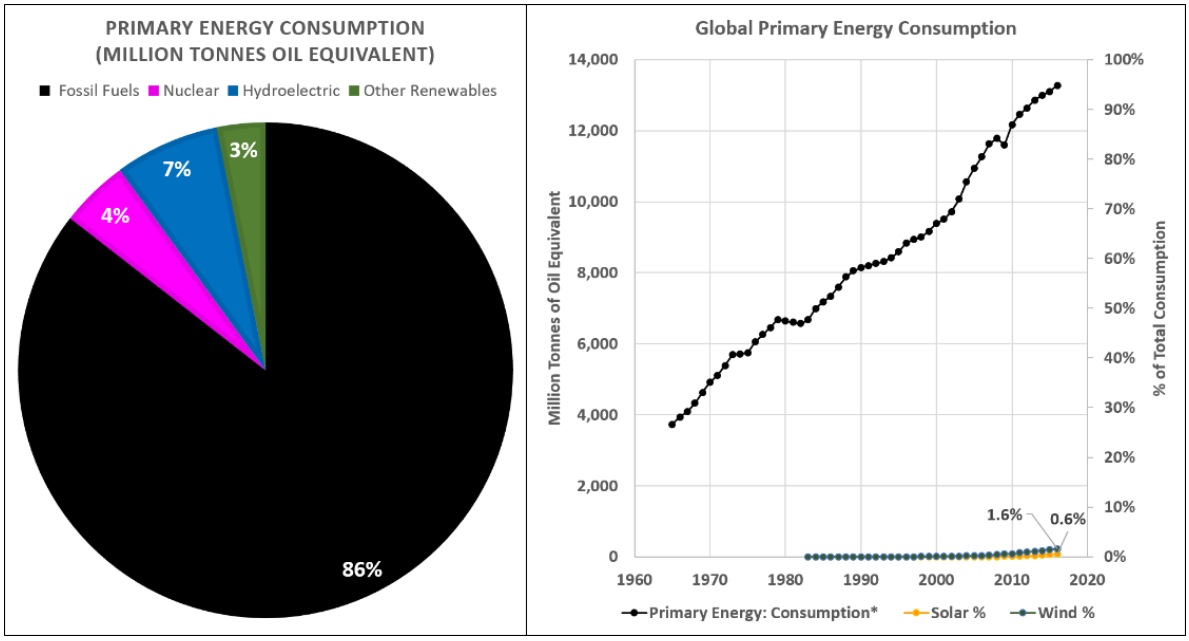

Figure 1-1 1965-2016 Global primary energy consumption.[17]

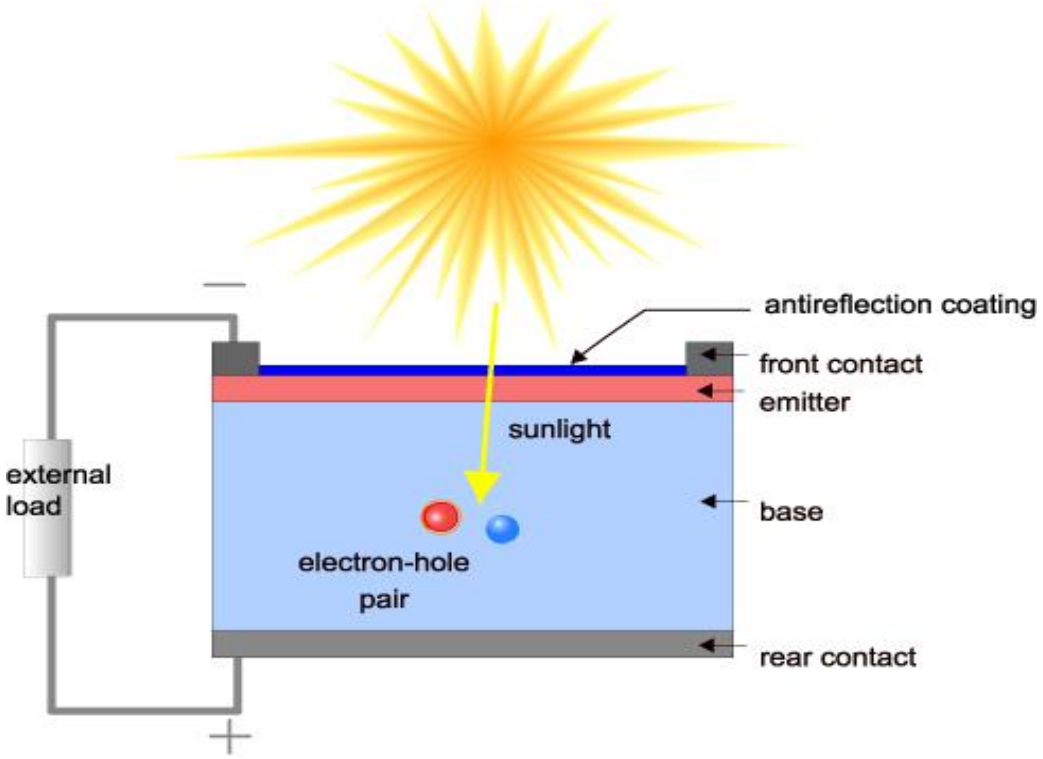

Figure 1-2 Typical solar panel configuration.[18]

1.2 Organic Solar Cells

An organic solar cell is a sort of photovoltaic electronic device that employs organic semiconductors (polymers or small molecules) as active layers for light absorption and photoelectric conversion.[19] In 1959, Kallamann and Pope developed the first organic solar cell by applying a single crystal of anthracene that sandwiched between two electrodes, which obtained photovoltaic efficiency of 0.00002%. Although the researchers could not explain the principle completely, they built a foundation for organic materials in photovoltaics.[20] A great advance of organic solar cell was achieved by Tang in 1986 with a power conversion efficiencies (PCEs) of 1%.[21] The structure and principle of this solar cell can be simply showed in **Figure 1-3**: Two organic planar heterogenetic layers are sandwiched between ITO-coated glass (contacts to anode) and silver (contacts to cathode). The two active organic layers consist of copper phthalocyanine (CuPc) and perylene tetracarboxylic derivative (PDI), displaying as electron donor and electron acceptor respectively. However, for the limited exciton dissociation length (less than 10 nm) in the planar heterojunction (PHJ) device, the

photovoltaic current is only contributed by the interface of single donor and acceptor layers.[22][23] Therefore, generally PCE of PHJ solar cell is not high. In order to overcome the drawback of PHJ device, bulk heterojunction (BHJ) solar cell was invented (**Figure 1-4b**). In a BHJ device, the organic layer is a blend of donor and acceptor within separated nanophases, providing a larger interfacial area and thus a shorter distance for exciton diffusion.[24] In 1995, the first BHJ was reported by Heeger et al, with a blend of MEH-PPV as an electron donor and C60 fullerene derivative ($PC_{61}BM$) (**Figure 1-5**) as an electron acceptor, indicating an outstanding PCE.[25] The utilization of fullerene derivative is an enormous improvement for OPV because of their high electron mobility and high electron affinity. For instance, the OSC device based on poly-3-hexylthiophene (P3HT) and $PC_{61}BM$ can show high-efficiency (5%) and excellent characteristics, such as thermal and chemical stability, which makes it a potential candidate for the mass-fabrication of OSCs.[26] In recent years, π-conjugated polymers also have been developed rapidly. For example, in 2018, the tandem OSC based on PTB7-Th:O6T-2F:$PC_{71}BM$ can obtain PCE of 17.3%, offering more viable choices of materials for OSC.[27]

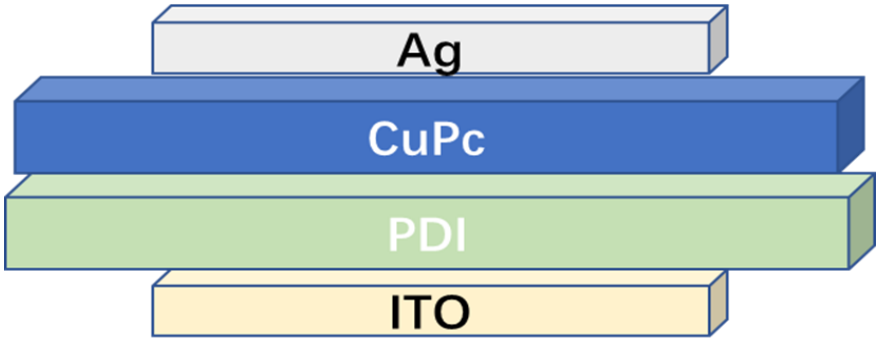

Figure 1-3 Device structure of OPV reported by Tang.[28]

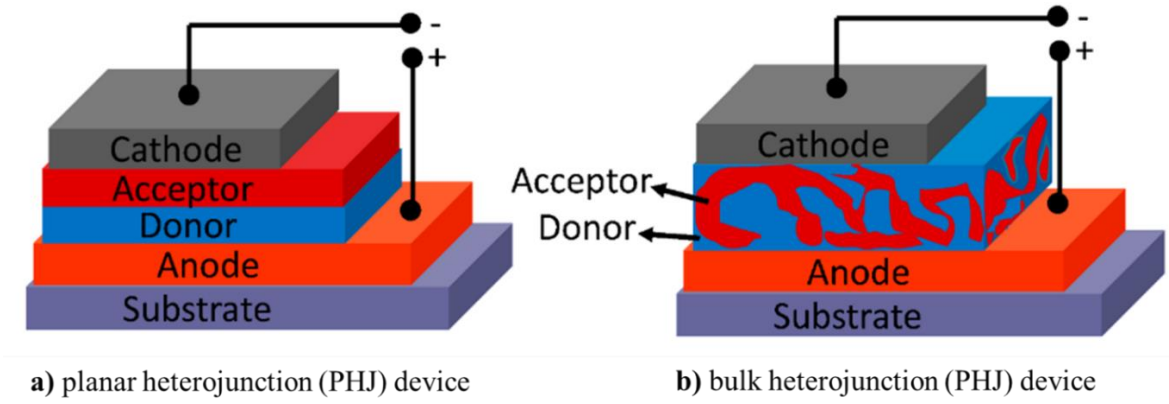

Figure 1-4 Device structures of (a) planar heterojunction, (b) bulk heterojunction.[29]

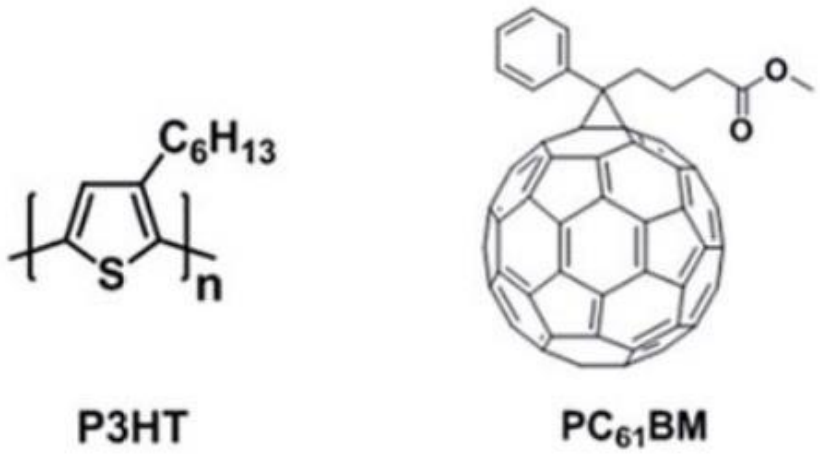

Figure 1-5 The structures of P3HT and $PC_{61}BM$.

In OSC, the photovoltaic conversion includes four consecutive steps (**Figure 1-6**): 1) light absorption, 2) exciton diffusion and dissociation, 3) charge transport and 4) charge collection.[14] Each of those steps is important in determining the overall PCE, requiring the optimization of material design, device fabrication.

Firstly, light absorption generates excitons: when the photon penetrates the front contact of a solar cell and is absorbed by the organic layers, an electron excites from the highest occupied molecular orbital (HOMO) to the lowest unoccupied molecular orbital (LUMO) from the donor and then an efficient exciton (a pair of electron and hole) is created. However, exciton

in organic semiconductors have to overcome the binding energy to dissociate free carriers because of the low dielectric coefficient, whereas the inorganic semiconductors can produce free carriers directly. Afterwards the exciton diffuses in the organic layers with a length of 10 - 20 nm. At the interface between donor and acceptor, due to the offset of the lowest unoccupied molecular orbital (LUMO) of the donor and the highest occupied molecular orbital (HOMO) of the acceptor, an electron will transfer from the exciton to the LUMO of the acceptor, leading to charged interface at the junction of donor and acceptor.[30] After getting rid of coulombic attraction, a free electron and a hole will be generated and flow to different electrodes.[31]

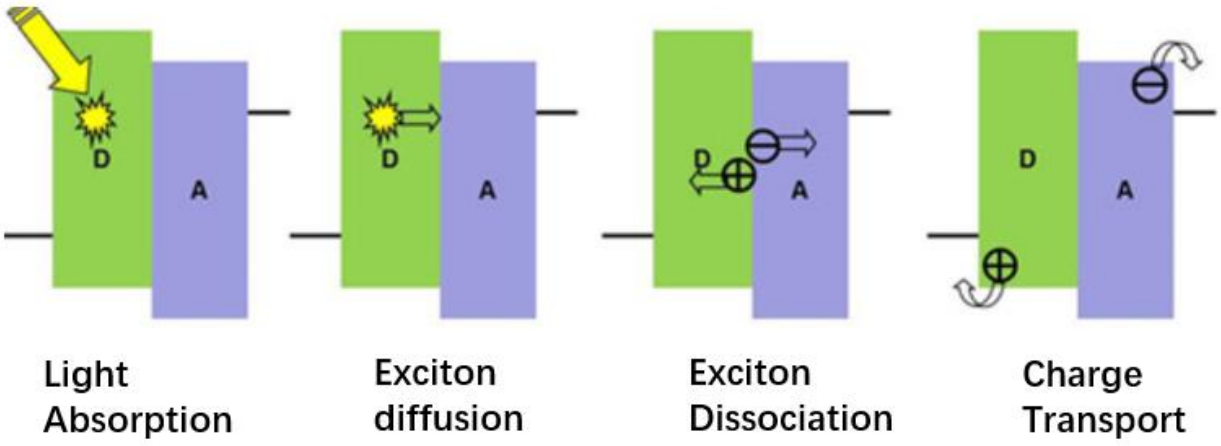

Figure 1-6 Functional mechanism of organic photovoltaic conversation.[32]

The characteristics of an organic solar cell (OSC) are determined by several parameters: power conversion efficiency (PCE), the open circuit voltage (V_{OC}), short circuit current density (J_{SC}), fill factor (FF) and external quantum efficiency. Above all, the most intuitive factor PCE is directly relevant to V_{OC}, J_{SC} and FF, which can be quantitatively analyzed from the voltage-current density (V-J) curve. (**Figure 1-7**)

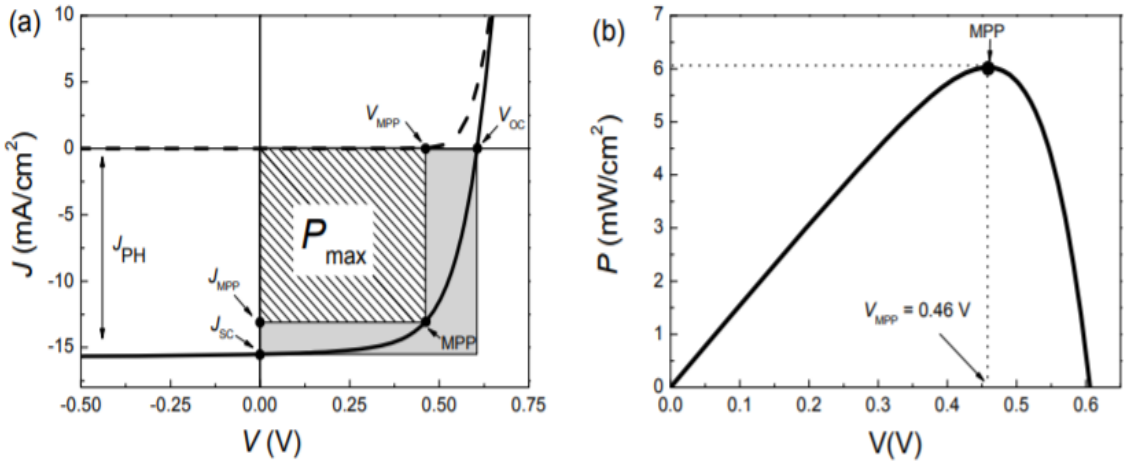

Figure 1-7 (a) Typical J-V characteristics. (b) Power density as a function of applied voltage.[33]

As showed in **Figure 1-7**, V_{OC} is the voltage when the external circuit of solar cell disconnects or J is 0, namely the maximum output voltage.

Heeger expressed the equation of V_{OC} through their discovery of recombination in polymer-fullerene bulk heterojunction solar cells:[34]

$$V_{OC} = \frac{1}{e}\left(E_{HOMO}^{Donor} - E_{LUMO}^{Acceptor} - D\right) - \frac{KT}{e}\ln\frac{N_e N_h}{N_c}$$

where N_e is termed the electron density in the fullerene domains, N_h is termed the hole density in the polymer domains under open circuit conditions, and N_c is the density of states (DOS) at the conduction band edge of the polymer and fullerene. The energy shift, D, increases from disorder inside the phase separated acceptor and donor domains.

Sequentially, Scharber proposed the relationship between V_{OC} and HOMO and LUMO of donor and acceptor, by summarizing 26 types of BHJ solar cells:

$$V_{OC} = \frac{1}{e}\left(E_{HOMO}^{Donor} - E_{LUMO}^{Acceptor}\right) - 0.3eV$$

According to this equation, the V_{OC} has a linear proportion to the diffidence between E_{HOMO}^{Donor} and $E_{LUMO}^{Acceptor}$, which supplies the design rules for BHJ solar cell.[35]

J_{sc} is the current density when the voltage across the solar cell is zero or the solar cell is short circuited. J_{SC} can be indicated by the equation:

$$J_{sc} = \mathrm{ne}\mu\mathrm{E}$$

Where n is charging density, e is elementary charge, μ is carrier mobility, and E is electric-field strength.

FF represents the degree of extraction of the free carriers from photovoltaic devices to electrodes.[36] FF is defined as the ratio of the maximum power from the solar cell to the product of V_{OC} and J_{SC}. At a particular point, according to the J-V curve, the maximum power (Pm) is obtained, then the PCE at this point can be calculated by:

$$\frac{P_m}{P_{in}} = \frac{J_m V_m}{P_{in}} = \frac{J_{sc} V_{oc} FF}{P_{in}}$$

As a result, FF can be expressed by:

$$\mathrm{FF} = \frac{J_m V_m}{J_{sc} V_{oc}}$$

Where P_{in} is the light power incident on the device, J_m is the current of the maximum power, V_m is the voltage of the maximum power.

Parasitic resistances such as series resistance (R_s) and shunt resistance (R_{sh}) can also impact on the J-V curve. When the R_s and R_{sh} are considered, the J-V characteristics can be represented as:

$$\mathrm{J} = J_L - J_O \exp\left(\frac{q(V + JR_S)}{nKT}\right) - \frac{V + JR_S}{R_{SH}}$$

Where J_L is the photocurrent, J_o is the dark current, q is the elementary charge, n is the ideality of diode and V is the applied voltage. Combining the equations, we can obtain that the FF will increase with the rise of R_{sh} and the decline of R_s. Apart from this, charge carrier mobility, interface recombination, film morphology and miscibility of blends also influence FF significantly.[37][38]

With all above parameters the PCE can be calculated as the product of V_{OC}, J_{SC}, and FF divided by input power (100 mW/cm^2 for the standard AM 1.5G spectrum multiplied by the area of the cell):

$$\mathrm{PCE} = \frac{J_{SC} V_{OC} FF}{P_{in}}$$

Thus, V_{OC}, J_{SC} and FF can determine the overall solar cell efficiency. The backbones and their conjugated systems are related to the basic properties of polymers such as band gap and energy position, thereby responding to V_{OC} and J_{SC}. A polymer with a low band gap and a broad absorption band can absorb more photons, which will lead to high J_{SC} for OPV device. For instance, a semiconductor with a low band gap 1.1 eV can harvest 77% of solar light, whereas a big band gap 2 eV only absorb 30% at most.[39] However, excessively low bandgap requires an increase of the HOMO level of donor and will decrease V_{OC}. According to Shockley's work, there is a theoretical optimal bandgap for light harvesting to coordinate V_{OC} and J_{SC}, which is around 1.3 eV.[40] Apart from bandgap, the energy levels of donor and accept also require to be matched. The LUMO of the donor should be at least 0.3 eV higher than the LUMO of the acceptor so that the driving force can overcome the binding energy to dissociate free carriers.[41] Thus, it is necessary to reach a balance to guarantee the low bandgap for donors while matching the energy levels of corresponding acceptors. In addition, optimizing side chains and introducing substituents such as, fluorine, cyano and heteroatoms can also influence J_{SC} and V_{OC} evidently.[42] Besides, morphology of organic active layer and network between donor and acceptor are also the important factors to affect those parameters. For BHJ solar cell, a domains width (20 nm) of donor and acceptor that is twice as the exciton diffusion length (**Figure 1-8**) is beneficial to exciton transport and free carries generation.[43]

The diversity of parameters poses challenges to get the best performance for OPV. However, on the other hand, it gives us more opportunities to design or optimize novel materials with fine energy levels, light absorption, blend morphology and transport characteristics to achieve higher efficiency cells.

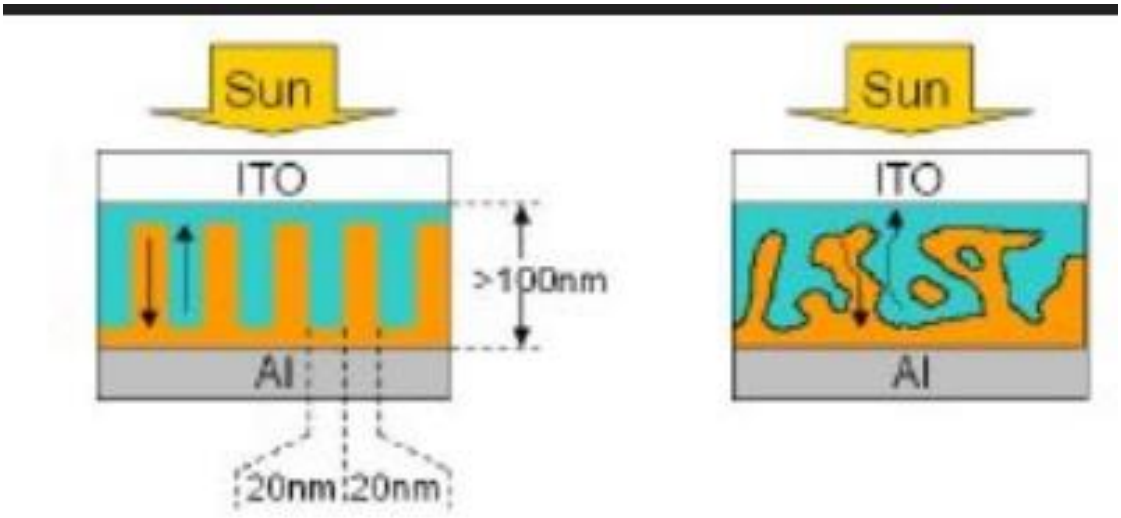

Figure 1-8 Ideal BHJ domain and real BHJ solar cell.[43]

1.3 π-Conjugated Polymers for Organic Solar Cells

The first famous π-conjugated polymers for OSCs is poly[2-methoxy-5-(2-ethylhexyloxy)-1,4-phenylenevinylene] (MEH-PPV) (**Figure 1-9**) that reported by Hegger and co-workers,[25] and another PPV-based polymer, MDMO-PPV (**Figure 1-9**), obtained a PCE of 3.3% with $PC_{61}BM$ as the acceptor.[44] The large bandgap (> 2 eV) and low mobility of PVV-based polymers are the bottleneck for high PCE.[45] Subsequently, regioregular poly(3-hexylthiophene) (P3HT) (**Figure 1-9**) attracted attention in solar cell, achieving PCE up to 5% with $PC_{61}BM$ as the acceptor because of its smaller band gap, better conjugated structure as well as morphology optimization.[34][46] Even at present, P3HT is still a star for PSC research due to its thermal and chemical stability and commercial available feather.[26] However, the restricted absorption (below 650 nm) and the high-lying HOMO level of P3HT limits the efficiency of P3HT-based solar cell.[47][48] In 2003, Andersson reported PFDTBT polymers (**Figure 1-9**) with the alternating donors (fluorene) and acceptors (dithienyl-benzothiadiazole), matching with $PC_{61}BM$ for a PCE 2.2%.[49] Since the PCE was not very high, this was the first time that donor-acceptor polymers were introduced in OPV, opening a new thread for OSC materials. In recent years donor-acceptor polymers composed of electron rich segments and electron deficient units along their polymer backbones, has been developed rapidly.[50] For

donor-acceptor polymer, the alternation of electron rich moieties (such as thiophene and bithiophene) and electron deficient units (such as diketopyrrolopyrrole) can determines the optical bandgaps, the energy levels and the carrier mobility: Firstly, the partial charge separation of donor and acceptor elevates the HOMO and lows the LUMO of donor-acceptor polymers, leading to a lower band gap (**Figure 1-10**).[51] Secondly, the intermolecular distance between donor-acceptor polymers is shortened by the attraction between donor and acceptor moieties of adjacent molecules, which is benefit to charge transport.[52] Thus, the donor-acceptor polymers have attracted growing attraction and demonstrated high PCE in OPV. For example, The discovery of the new polymer family, PTB-based polymers that consist of electro-rich BDT unit and electron-poor TT unit, was a significant breakthrough in OSC field.[36] The introduction of a fluorine atom into the TT unit of PTB-based polymers caused a great improvement of PCE. Especially, poly-thieno [3,4-b]-thiophene-co-benzodithiophene (PTB7) polymer stands out as one of the most promising donor for OSC and a benchmark in this field.[42] For example, in 2016, Wan et al optimized PTB7-Th (**Figure1-9**)/$PC_{71}BM$ cell that achieved high PCE up to 10.8%[53]. Recently, a highly efficient ternary cells based on PTB7-Th, COi8DFIC and $PC_{71}BM$ offered PCE 14.08%.[54]

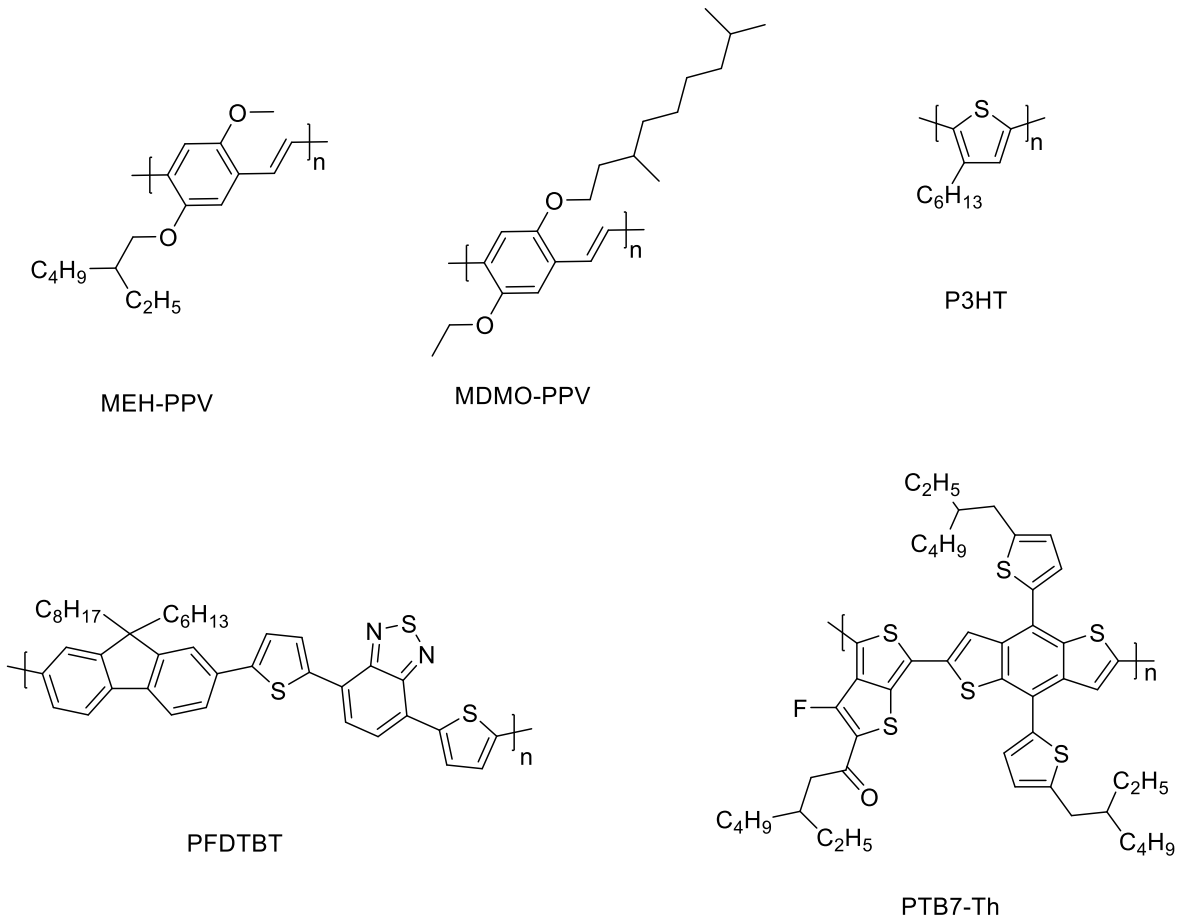

Figure 1-9 The structure of MEH-PPV, MDMO-PVV, P3HT, PFTBT and PTB7-Th.

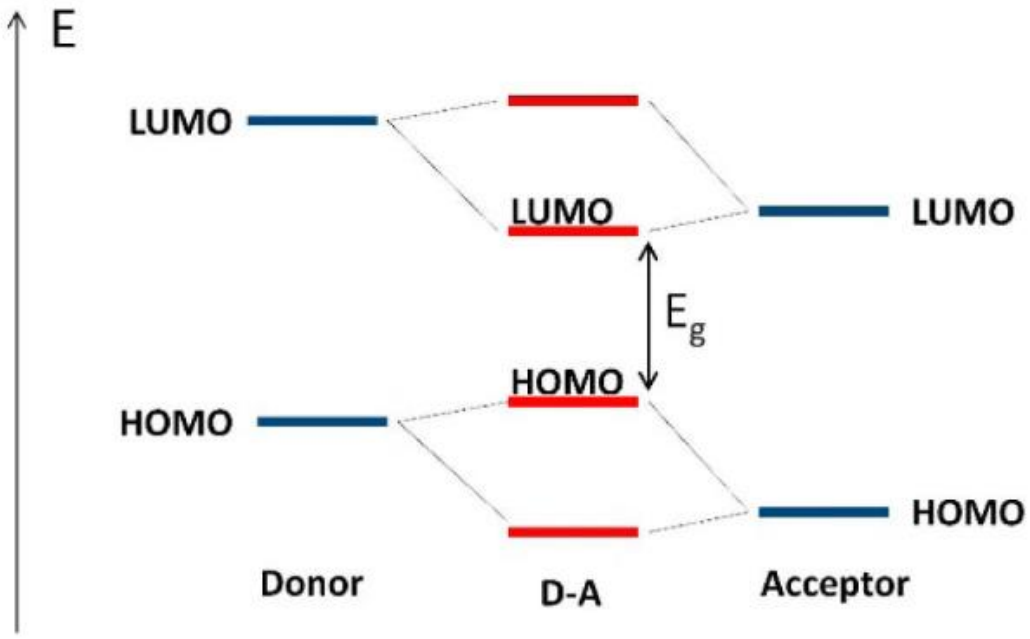

Figure 1-10 Molecular orbital theory explanation for band gap reduction in D-A copolymer.

1.4 All-polymer Solar Cell

Since the first BHJ solar cell was reported by Heeger, fullerenes, particularly $PC_{61}BM$ and $PC_{71}BM$-based derivatives, have been the mainstream acceptor in BHJ OSCs.[55] In fact, acceptor based on non-fullerene materials generally obtained lower PCE than fullerene-based acceptor in OPV during a long time. However, the gap between fullerene and non-fullerene solar cells keeps shrinking significantly result from the synthetic methods, materials design strategies and device engineering protocols developed.[56] On the other hand, although fullerenes in OPVs have sensible advantages, such as excellent electron transport characteristics, adequate LUMO energy level, anisotropic charge transport and high electron affinity,[57] fullerenes and their derivatives also suffer from several inevitable drawbacks: First of all, it is difficult for fullerenes to absorb red and near-infrared region due to weak optical light absorption, although $PC_{71}BM$ derivatives provide better absorption than $PC_{61}BM$s (**Figure 1-1**).[58][59] Secondly, high electron affinity of fullerene determines their excessively

low LUMO, which limits the operating voltage of organic SCs.[60] Moreover, fullerene molecules have high degree of functionalization, so the increase of their LUMO level is not easy.[61] Thirdly, in organic active layer, fullerenes prefer to aggregate under light and thermal, so that the performance of fullerene OSCs will decline in a short term.[62][63] Finally, the cost of fullerene production is high.[64] Those above disadvantages stimulated the exploitation of non-fullerene SCs, which normally use conjugated polymers or small molecules as acceptor instead of fullerenes. On the other hand, all-polymer solar cells (all-PSCs), consisting of polymer-donor and polymer-acceptor materials, achieved considerably more efficiencies and attracted more attention in recent years. Compared with fullerenes, polymer semiconductors have easily tunable absorption of visible light to enhance light-harvesting at long wavelengths. Also, owing to the diversity of chemical structure, polymer materials possess efficient tuning of energy levels, one of the key factors of high PCE in OPVs.[65] In addition, polymer/polymer blends offer prominent flexibility in controlling solution viscosity, providing the feasibility of large-sale OSC fabrication in industrial coating process.[66] Besides, the all-PSCs could display superior mechanical robustness and thermal stability compared with the fullerene-PSC and OPV.[67] Due to the intensive efforts in structure engineering and device optimization, the PCE of all-PSCs have dramatically increased in recent years, which is over 10%.[68] To achieve high performance all-PSCs, it is necessary to design and synthesis new polymer acceptor materials that have the following features: 1) good solubility, 2) well-matched energy levels for efficient charge transfer, 3) small bandgap for good light harvest, 4) high electron mobility for efficient charge transport, and 5) favorable miscibility with donor materials for ideal phase-separated BHJ structure.

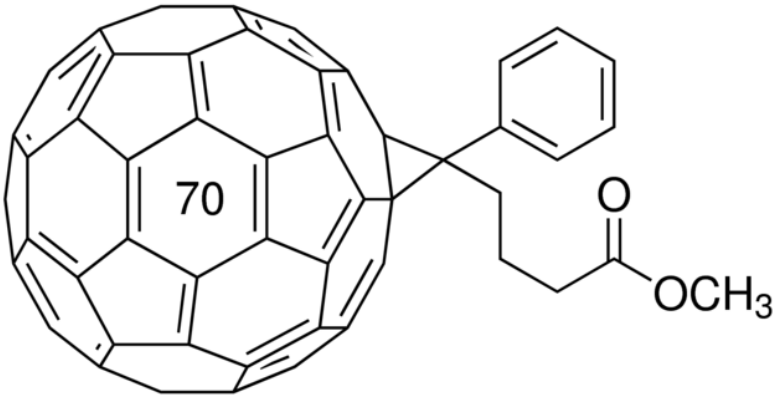

Figure 1-11 The structure of $PC_{71}BM$.[69]

1.5 Characterization of Polymers

To acquire a scientific work, there are several techniques used to investigate the properties of materials during polymer synthesis and explain the obtained results. The techniques applied for this work are simply presented below.

Nuclear magnetic resonance (NMR) spectroscopy is widely used to determine organic chemical identity and structure. Many atomic nuclei have a property called spin. When a magnetic field is applied, the NMR active nuclei, such as ^{1}H and ^{13}C, will induce resonance frequencies. Due to the difference of electron distribution, the resonance frequencies will vary in different signals. By counting the chemical shifts resulted from resonance signals relative to the resonance frequency of the reference substance, such as tetramethylsilane (TMS), NMR spectrum can be obtained. Compared with chemical shifts table, the chemical structure and purity can be analyzed and determined.[70]

For resulted polymers, gel permeation chromatography (GPC) is an important technique to determine their number average molecular weight (Mn), weight average molecular weight (Mw) and polydispersity index (PDI). In GPC column, the porous gel particles, such as cross-linked polystyrene, can separate the polymers on the basis of their size in solution. Molecules with smaller hydrodynamic volumes (low molecular weight) are enable to pass more pores in the column, and therefore they consume more time or volume in the column. Based on the elution behavior of the polymer standards of known molecular weight with narrow distributions (e.g., polystyrenes), the number of polymers with different molecular weight (Mn

and Mw) can be obtained as a function of retention time or volume.[71] Further, PDI can be calculated by Mw/Mn, which is an index of the molecular weight distribution.

Thermal gravimetric analysis (TGA) is a method of thermal analysis, which detects the change of mass as the temperature increases. In this work, TGA is used to evaluate the thermal stability of polymers so that the temperature range can be determined in further application. Differential scanning calorimetry (DSC) is another thermoanalytical measurement for phase transition properties. In DSC experiment, the sample and reference are maintained at the same temperature. When the sample undergoes phase transition, the sample will absorb or release heat in order to retain the same temperature with the reference.[72] Hence, from the curve of heat flow and temperature, exothermic or endothermic process will be monitored. DSC can identify the crystallization and the glass transition temperatures of polymers, which is a valuable approach to investigate the relationship between thermal properties and charge transport properties.

For organic semiconductor, the ultraviolet-visible spectroscopy (UV-Vis) is routinely used to study the optical properties. The UV-Vis absorption spectrum of dilute solution and thin film of polymer can provide many useful characteristics, such as aggregation properties and light absorbance range. In addition, the optical bandgap (E_g) of polymer represents the minimum amount of energy required for a photon to excite an electron from HOMO to LUMO, which can be determined from the onset absorption (λ_{onset}) by the equation[73]:

$$E_g = \frac{h \times c}{\lambda_{onset}} \times e$$

where h is Plank's constant, c is the speed of light and e is the energy of an electron.

Cyclic voltammetry (CV) is a type of electrochemical measurement, where the working electrode potential is ramped linearly versus time. During the cycles of ramps in potential, the reduction onset potential (V_{red}) is the energy at which electrons are injected to LUMO, whereas oxidation onset potential (V_{ox}) represents the energy at which electrons are removed from HOMO. Ferrocene with a known HOMO at -4.8 eV, whose an oxidation onset potential is set at 0 V, is often used as a reference.[74] As a result, the HOMO/LUMO can be obtained by the equations below:

$$\text{HOMO} = -V_{ox} - 4.8\ eV$$

$$\text{LUMO} = -V_{red} - 4.8\ eV$$

Density functional theory (DFT) is a computational quantum mechanical modelling method based on a determination of the electron density of the molecule. With the theoretical ground state investigated by DFT, the properties of a given chemical structure can be predicted, such as HOMO and LUMO energy levels, the electronic distribution and the atomic geometry.[75] Thus, DFT calculation is an efficient method to design polymer structures and interpret polymer properties.

X-ray diffraction (XRD) is a widely used technique of polymer characterization that can provide information concerning both the crystalline and amorphous states. In XRD measurement, the incident X-ray beams is scattered at polymer film with varying incident angles. The interaction of the incident rays with the polymer film will generate constructive interference only when the condition satisfies Bragg's law: $n\lambda=2d\sin\theta$.[76] Where d is the polymer packing distance, θ is the incident angle, n is any integer and λ is the wavelength of the X-ray beam. Hence, the polymer chain packing distance can be calculated from the diffraction peak. Atomic force microscopy (AFM) is another important measurement for the solid-state properties. In AFM measurement, a tip is attached to the free end of the cantilever, which is used to scan the sample surface. When the tip is brought into proximity of a sample surface, forces between the tip and the sample will cause a deflection of the cantilever. A laser beam is reflected off the back of the cantilever to a 4-quadrant photodiode detector. According to the surface morphology, the tip of the cantilever will bend and the detector can measure the deflection.[77] The created image is a computational visualization of the sample surface.

1.6 Project Objectives and Thesis Structure.

At present, the development of all-PSCs is still far behind that of fullerene/polymer solar cells due to the lack of the acceptor polymers with efficient n-type performance.[78] In order to develop polymeric semiconductors with stable n-type properties, a strong electron-deficient unit is needed to bring down the LUMO of D-A polymers.[79] Therefore, in Chapter 2, the objective of the work is to take advantage of the strong electron-withdrawing group

dipyrrolo[2,3-b:2',3'-e] pyrazine-2,6(1H,5H)-dione (PzDP) to design new polymer with low-lying energy levels. The resultant PzDP-based polymers will be characterized to study the optical and electronic properties. A suitable donor polymer (PTB7-Th) will be used to fabricate the all-PSCs, and several optimizations will be utilized to investigate the photovoltaic properties of the polymers. The results will be further analyzed by using XRD, AFM and SCLC measurements.

On the other hand, polythiophene (PT) derivatives have attracted considerable interest in OPV due to their high hole mobility and simple synthesis.[80] However, the most classical PT derivative, poly(3-hexylthiophene), exhibited a high-lying HOMO level and a large bandgap and thus caused limited performance in solar cells.[48] In order to solve these issues, in Chapter 3, a novel PT derivative 5,7-bis(octylthio)-1,4-di(thiophen-2-yl)thieno[3,4-d] pyridazine (TPT) will be synthesized and used for the first time to form a D-A polymer. The new building block TPT is attempted to obtain deep HOMO and narrow bandgap due to the strong electron-deficient nitrogen atoms in the backbone and internal charge transfer of D-A polymer. The characterization of related polymer TPT-BDT will be presented.

Finally, in Chapter 4, the thesis work will be summarized and then some future directions will be proposed for further improvement.

Chapter 2 Synthesis and Characterization of PzDP-based Polymers

2.1 Introduction

All-polymer solar cells, which contain conjugated polymers with n-type properties as electron-acceptors to replace fullerene derivatives, have been extensively studied in recent years.[81] However, the number of n-type polymers lags far behind p-type polymers, which have limited development of all-PSC.[82] Therefore, the design of n-type polymers is highly required and relevant for efficient all-PSCs. In particular, to achieve high performance, incorporating electron-deficient groups into the linear conjugated backbones, such as naphthalene diimide (NDI), perylene diimide (PDI) and diketopyrrolopyrrole (DPP) unit, is vital to design acceptor polymers for all-PSCs.[83] Among them, DPP-based polymers, are promising candidates for high-performance OPVs due to a high intrinsic charger transferability, low bandgaps, excellent thermal-stability and photostability, and impressive crystallinity.[84] For instance, DPP-based polymers have enable power conversion efficiencies of up to 9.4% when DPP-based polymers acted as electron donor and $PC_{71}BM$ was used as electron acceptor.[85] However, although several DPP-based polymers show their potential for use as electron acceptors in PSCs due to excellent electron mobilities in FETs, unit DPP have been used much less than NDI and PDI.[86] To apply DPP-based polymer as the electron acceptor in organic solar cells, the electron affinity is needed to be further modified to get low-lying energy levels.[82] For example, Wei designed DPP incorporating two thiazoles rings to obtain low-lying energy levels. The resulting DPP polymer can act as an electron acceptor in PSCs to reach a PCE of 2.9%.[87] Thus, following this principle, we explored PzDP, the analogous structure of DPP with stronger electron affinity for electron-acceptors in efficient photovoltaic devices.

PzDP compounds were first created by Hoechstetter as pigments and dyestuffs[88], which is a trinucleate heterocyclic consists of pyrazine that is sandwiched between two pyrrolinones to offer a large π-conjugated fused ring structure.[89] It can be regarded as a derivative of DPP isomer (**Figure 2-1**), which is a strongly electron withdrawing moiety. Attachment of electron-deficient pyrrolinone in DPP isomer unit can induce significantly more electron-accepting property than DPP unit, thereby enhancing stronger electron transport characteristics.

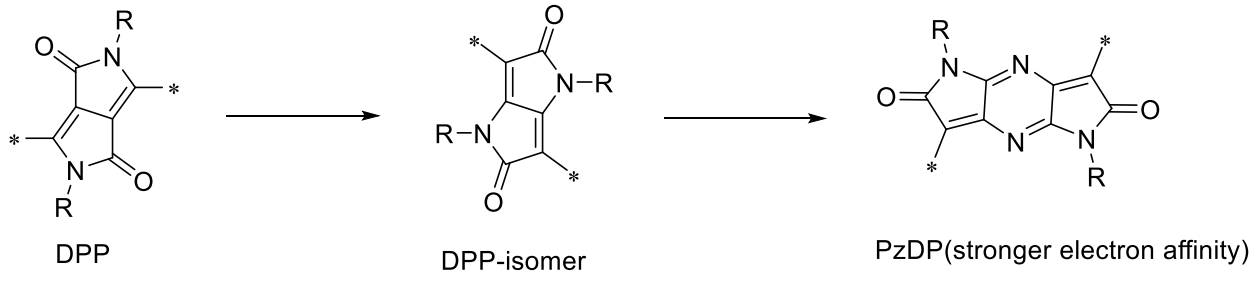

Figure 2-1 A structural comparison of DPP, iso-DPP and PzDP.

We first elucidated the coplanarity, electron distribution, and energy levels of the PzDP unit by conducting computational simulations on two model compounds: PzDP-Me and DPP-Me, whose nitrogen atoms were substituted by methyl groups for simplicity. The simulation results clearly showed that the PzDP-Me unit has a highly coplanar geometry with about 0° between the dipyrrolo-pyrazine-dione core and the benzene unit (**Figure 2-2**), which is crucial for forming closely packed π-π stack. The HOMO and LUMO energy levels of PzDP-Me are -5.75 eV/-3.40 eV, while the HOMO and LUMO of DPP-Me are -4.97 eV/-2.51 eV (**Figure 2-3**), which suggests the PzDP building block is significantly more electron deficient than the DPP. Hence, PzDP based polymers have promising potentiality to provide a stable n-type performance, which is necessary for the acceptor of all-PSCs.

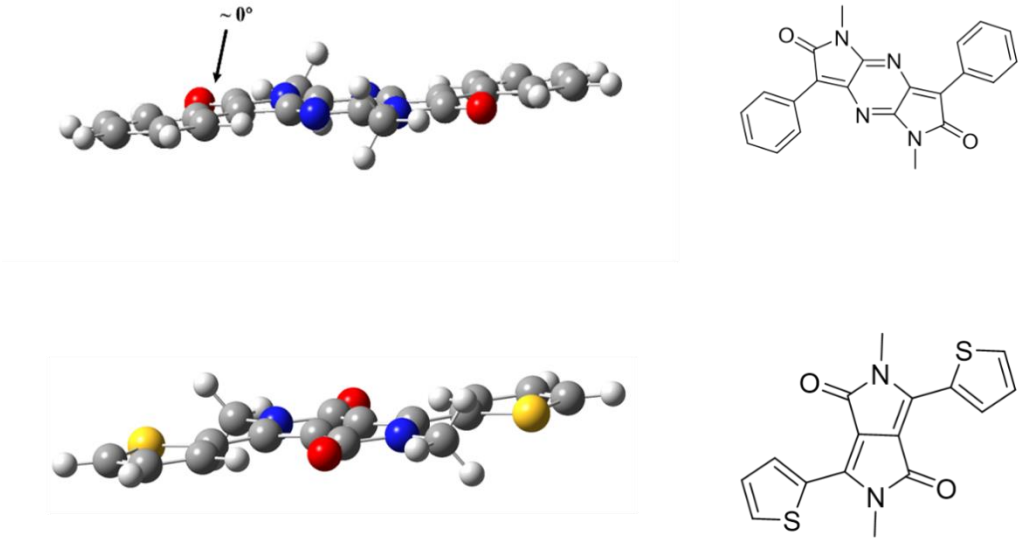

Figure 2-2 A geometry comparison of PzDP-Me and DPP-Me.

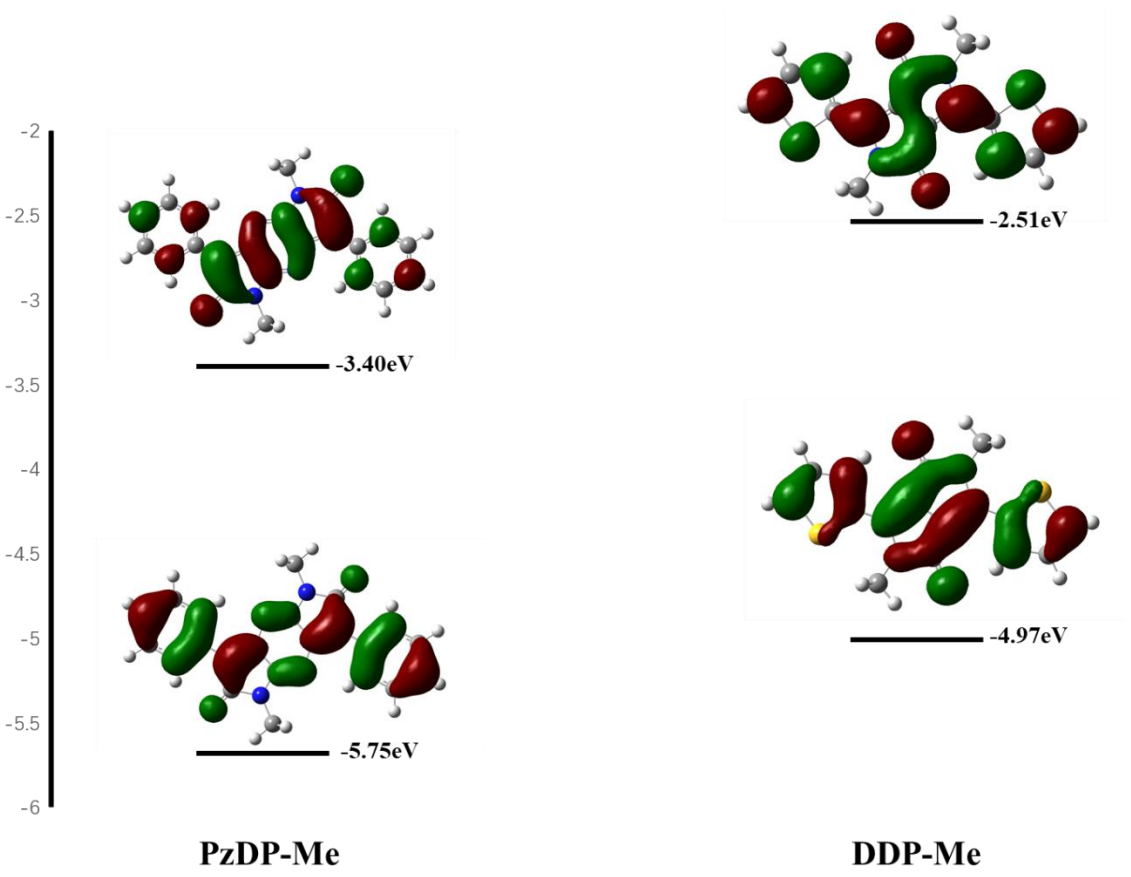

Figure 2-3 Predicted energy levels of PzDP-Me and DPP-Me.

2.2 Synthesis of PzDP Monomers and Related Polymers

The synthesis routes for PzDP monomers and polymers are outlined in **Scheme 2-1** and **Scheme 2-2**, respectively. Ethyl 2-(4-bromophenyl)-2-oxoacetate (Compound 1), 1,4-diacetylpiperazine-2,5-dione(Compound 2) and 2,2-bis((3,7-dimethyloctyl)oxy) ethyl bromide (Compound 3), 3,7-bis(4-bromophenyl)dipyrrolo[2,3-b:2',3'-e]pyrazine-2,6(1H,5H) dione) (Compound 4) were synthesized according to the literature methods.[90][91][92][89]. The compounds of each steps can be produced in high yield except compound 4 (25%). The low yield of compound 4 may be due to selectivity of its starting material (Compound 3), which is a mixture of cis-/trans- isomers. In addition, 4 branched alkyl chains were introduced to the

nitrogen atoms through base-catalyzed to solubilize the PzDP structure during polymerization and to optimize solubility of polymers. Moreover, all of the monomers were purified twice by silica gel column chromatography and recrystallized 3 times, aiming to improve molecular weight and obtain narrow dispersity.

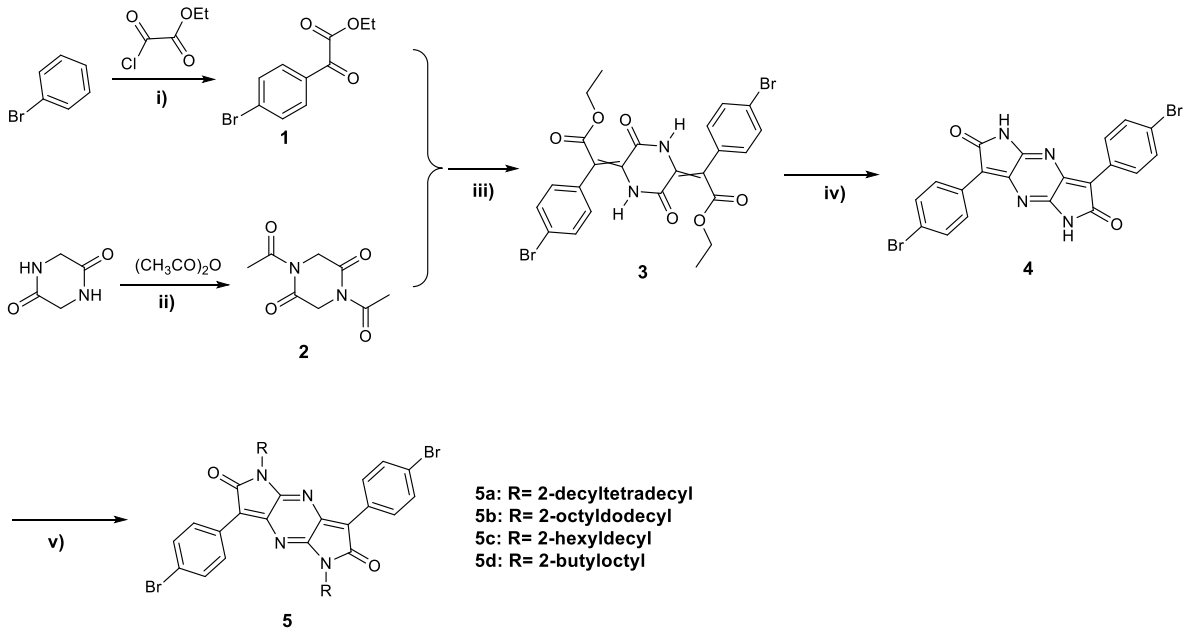

Scheme 2-1 Synthetic route towards PzDP monomers.

Reaction conditions: i) DCM/$AlCl_3$/0 °C/4 h, 75%; ii) Et_3N/60 °C/8.5 h, 79%; iii) Et_3N/55-60 °C/8.5 h, 79%; iv) $HCONH_2$/150 °C/overnight, 25%; v) DMF/K_2CO_3/130 °C /8 h, 51-63%.

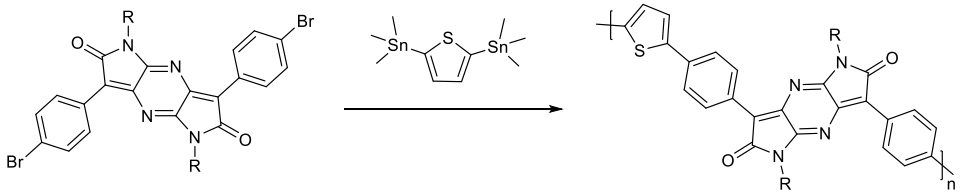

PzDP24-T: R= 2-decyltetradecyl
PzDP20-T: R= 2-octyldodecyl

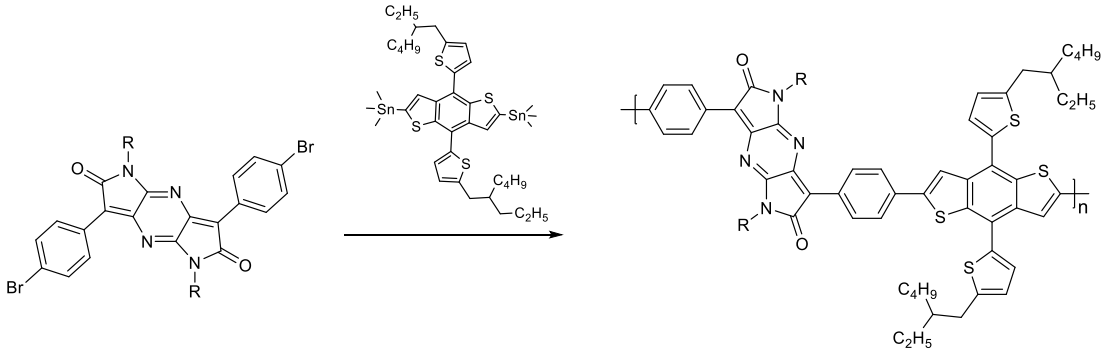

PzDP20-BDTTT8: R= 2-octyldodecyl
PzDP16-BDTTT8: R= 2-hexyldecyl
PzDP12-BDTTT8: R= 2-butyloctyl

Scheme 2-2 Synthetic route towards PzDP polymers.
Reaction conditions: Toluene/Pd $(PPh_3)_2Cl_2$/90-110 °C /48 h, 88-93%.

2.3 N-type Dominant Polymer PzDP24-T

2.3.1 Preparation of PzDP24-T

Three PzDP-T polymers were synthesized via Stille coupling polymerization of 5a - 5c with 2,5-bis(trimethylstannyl) thiophene using the toluene/Pd $(PPh_3)_2Cl_2$ system.[89] After being precipitated in methanol, the crude polymer was further purified by Soxhlet extraction with acetone, hexane and chloroform. In the backbone of PzDP-T, the benzene-thiophene units, as "weak donor", help maintain a low HOMO energy level, while PzDP, the electron deficient moieties as "strong acceptor", reduce the band gap by internal charge transfer.

The first PzDP-T polymer in this study is PzDP20-T, in which a branched alkyl chains 2-octyldodecyl was introduced to the nitrogen atom through base-catalyzed N-alkylation. However, 2-octyldodecyl is not enough to decrease the strong intermolecular interaction that

caused by the large fused PzDP core, so the PzDP-20-T is not soluble in some common organic solvent, such as chloroform and chlorobenzene, in spite of a low M_n. Consequently, PzDP-20-T was discarded in further research because it showed no solution processability.

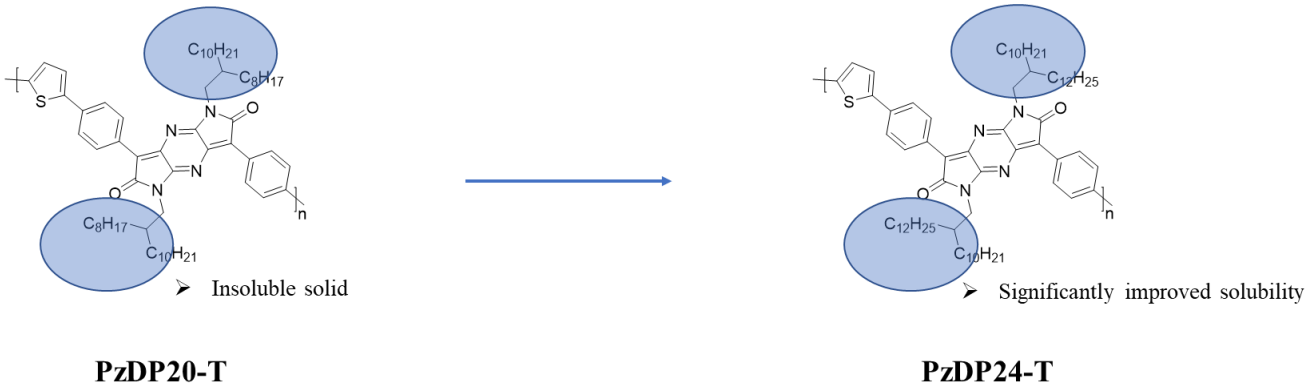

PzDP20-T **PzDP24-T**

Figure 2-4 The comparison PzDP-T copolymers with two different alkyl chains**.**

PzDP-24-T was then prepared via Stille coupling polymerization of 4b with 2,5-bis(trimethylstannyl) thiophene, and purified using Soxhlet extraction. After optimization of side chain from C20 to C24, the PzDP-24-T demonstrated significantly enhanced solubility and processability in chloroform and chlorobenzene. (**Figure 2-4**)

2.3.2 Characterization of PzDP24T

The molecular weight of PzDP24T was determined by high-temperature gel-permeation chromatography (HT-GPC) using 1,2,4-trichlorobenzene as an eluent and polystyrene as standards at 140 °C (**Figure 2-5**). The number average molecular weight (M_n) and PDI were measured to be to be 28.3 kDa and 3.12, respectively.

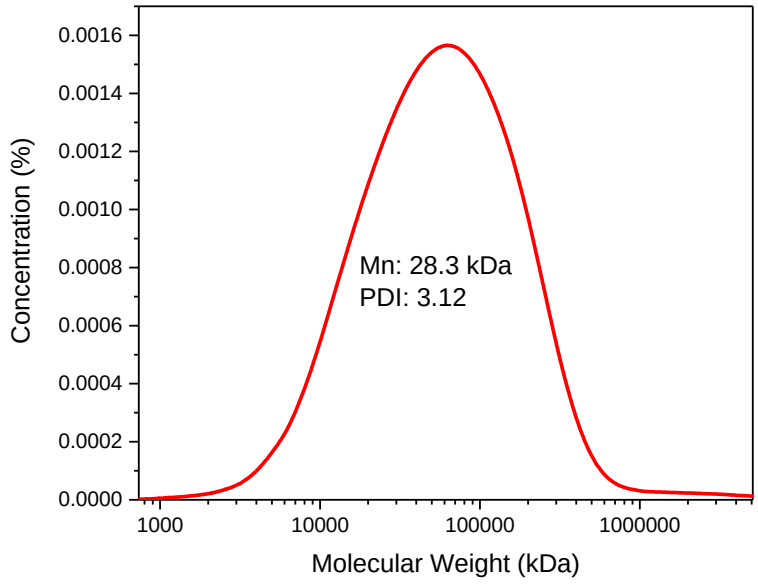

Figure 2-5 The molecular weight distribution for PzDP24-T obtained by HT-GPC**.**

The thermal stability of the polymer PzDP-24-T was characterized by thermogravimetric analysis (TGA), and **Figure 2-6** shows that the polymer exhibits excellent thermal stability with only 2% weight loss was observed at 440 °C under the inert atmosphere. In addition, neither exothermic nor endothermic transitions were observed in the range from -20 °C to 300 °C in the DSC measurement (**Figure 2-7**), suggesting the absence of crystalline domains.

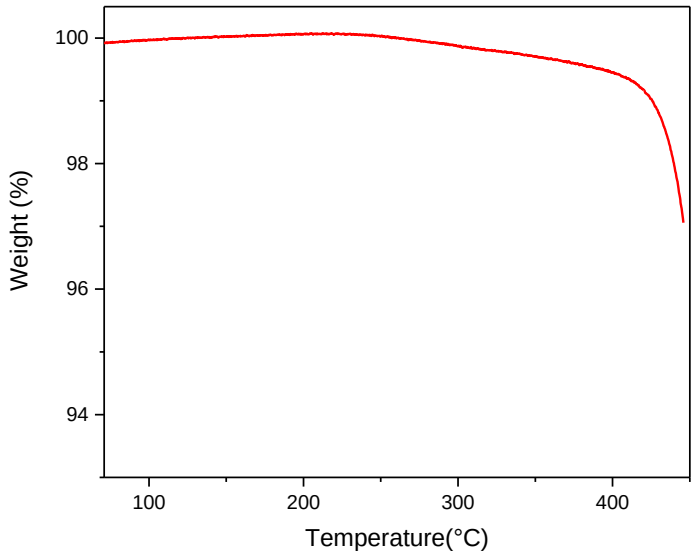

Figure 2-6 TGA curve of PzDP24-T measured with a heating rate of 10 °C min^{-1} under nitrogen.

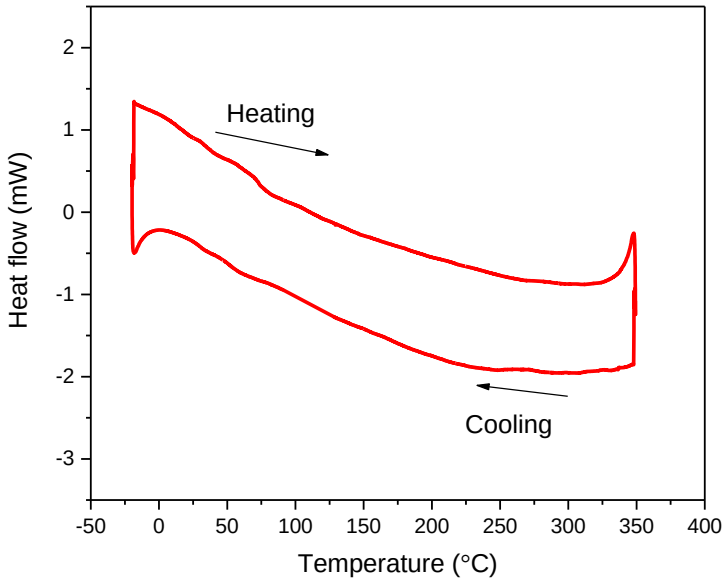

Figure 2-7 Differential scanning calorimetry (DSC) profiles of PzDP24-T obtained at a scanning rate of 10 °C min^{-1} under nitrogen.

PzDP-24-T exhibited a broad UV-vis-IR absorption spectrum range from 350 nm to 900 nm.

(**Figure 2-8**) The near-infrared absorption spectrum is ideal for applications in OPV for effective light harvesting. In the dilute solution (chloroform), the PzDP24-T showed a maximum absorption peak at 759 nm and an intense peak at 705 nm. Interestingly, in solid state (as-spun film), both peaks slightly blue shifted to 753 nm and 684 nm, respectively, which is an indication of the dominance of H-aggregate.[93] The optical band gaps of the polymer films are calculated to be 1.44 eV by using the absorption onsets, which is slightly wider than those (~ 1.3 eV) of the DPP-based polymers with thiophene linkages.[94]

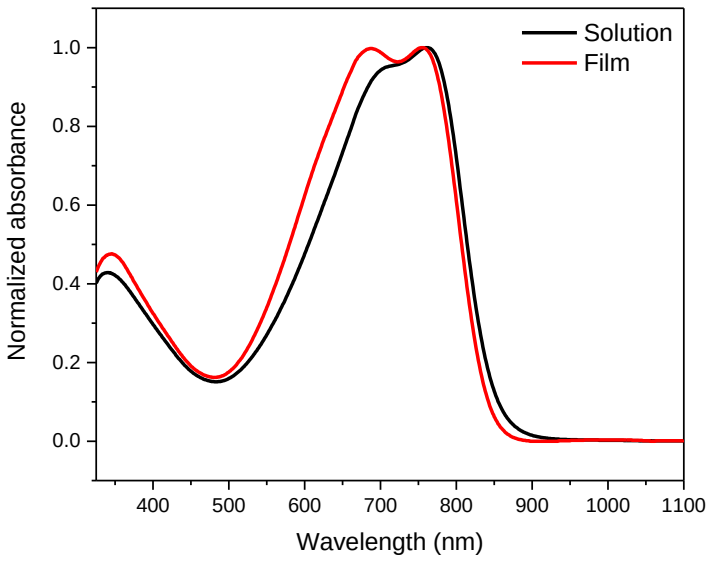

Figure 2-8 The absorption profile of in PzDP24-T diluted solution (chloroform) and thin film.

Cyclic voltammetry (CV) was carried out to investigate electrochemical property of the polymer (**Figure 2-9**). By using the oxidative onset potentials, the HOMO level of PzDP24-T was determined to be -5.77 eV, whereas the LUMO level was calculated from the reduction onset potentials to be -3.94 eV. Comparing to the HOMO/LUMO (-5.30 eV/-3.74 eV) levels of the DPP-based polymers with single thiophene linkages,[95] HOMO/LUMO levels of PzDP24-T were lowered by 0.47 eV and 0.26 eV, which indicates that the PzDP unit has stronger electron accepting effect than that of DPP moiety. The lower-lying LUMO of PzDP24-T can lead to more efficient photoinduced charge separation at the interfaces between donor and acceptor in OSC.

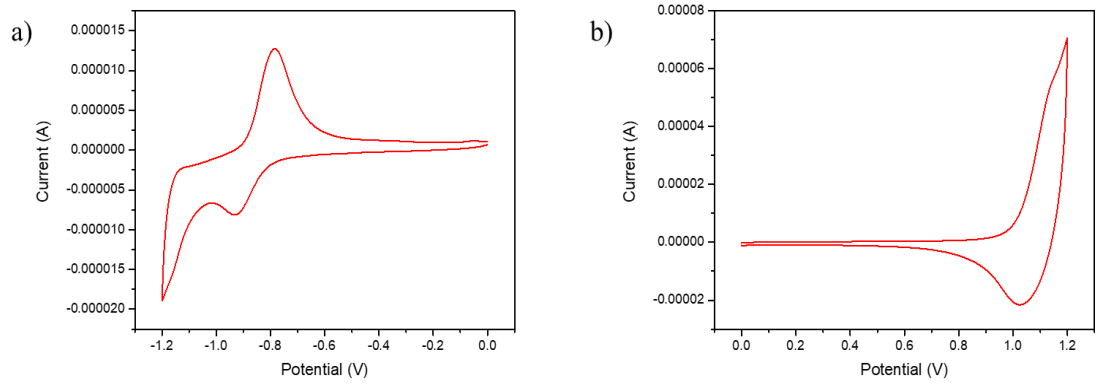

Figure 2-9 Cyclic voltammogram of PzDP24-T in a 0.1 M tetrabutylammonium hexafluorophosphate solution in acetonitrile.

PzDP24-T was characterized as channel semiconductors in bottom-gate, bottom-contact OTFT devices with gold being the drain and source electrodes. The polymer thin films were obtained by spin coating a polymer solution in chloroform onto DTS-modified SiO_2 dielectric layer, and optionally annealed at different temperatures (50 °C, 100 °C, 150 °C and 200 °C) a nitrogen filled glovebox. The polymer showed n-type dominant ambipolar charge transport behavior (**Figure 2-10**). The highest mobility was achieved at annealing temperature of 150 °C with electron mobility up to 0.029 $cm^2\ V^{-1}\ s^{-1}$ with an average of 0.025 $cm^2\ V^{-1}\ s^{-1}$ (**Table 2-1**). Moreover, the hole mobility for PzDP24T is relatively low with the best mobility 0.0021 $cm^2\ V^{-1}\ s^{-1}$ at 150 °C, which is different from DPP-polymers incorporating thiophene with well-balanced hole and electron mobilities. This likely arises from a limited hole injection because of the relatively deep HOMO level of PzDP24-T.

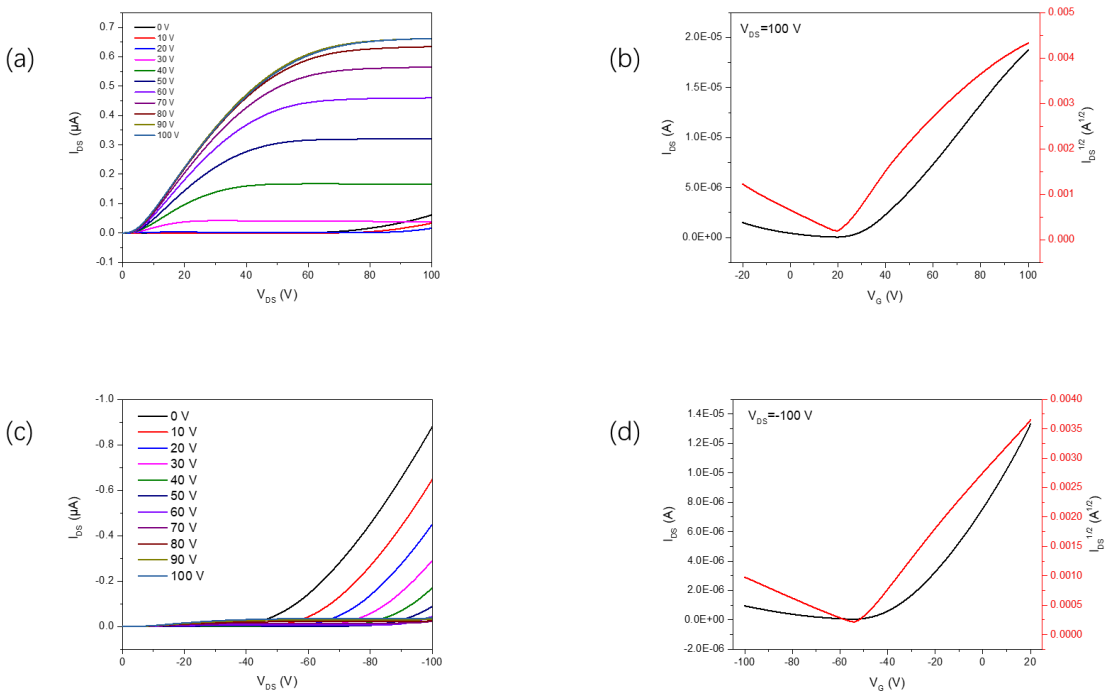

Figure 2-10 The output curves (a)/(c) in the electron/hole enhancement mode. The transfer curves (b)/(d) in the electron/hole enhancement mode. The BGBC OTFT devices with 150 °C-annealed PzDP24-T films. Device dimensions: channel length (L) = 30 μm; channel width (W) = 1000 μm.

Table 2-1 The summary of BGBC OTFT performance of PzDP24-T.

$T_{annealing}$ (°C)	Hole mobility [a] ($cm^2 V^{-1} s^{-1}$)	Electron mobility [a] ($cm^2 V^{-1} s^{-1}$)
RT	0.0013± 0.0002 (0.0015)	0.017± 0.001 (0.018)
50	0.0015± 0.0001 (0.0016)	0.019± 0.002 (0.021)
100	0.0015± 0.0003 (0.0018)	0.022± 0.001 (0.023)
150	0.0015± 0.0003 (0.0018)	0.025± 0.004 (0.029)
200	0.0013± 0.0002 (0.0015)	0.011± 0.003 (0.014)

[a] The average mobility ± standard deviation (maximum mobility) calculated from the saturation regions of five devices.

The low-lying energy levels, the narrow bandgap, good electron transporting characteristic, and the near-infrared absorption spectrum suggest PzDP24-T is a potential electron acceptor for polymer-polymer solar cells. We selected PTB7-Th as the complementary donor due to its relatively high-lying HOMO (-5.24 eV) and LUMO (-3.66 eV) levels[96], which provide a large enough energy offset (> 0.3 eV) with the HOMO and LUMO of PzDP24-T to facilitate efficient charge dissociation. (**Figure 2-11**)

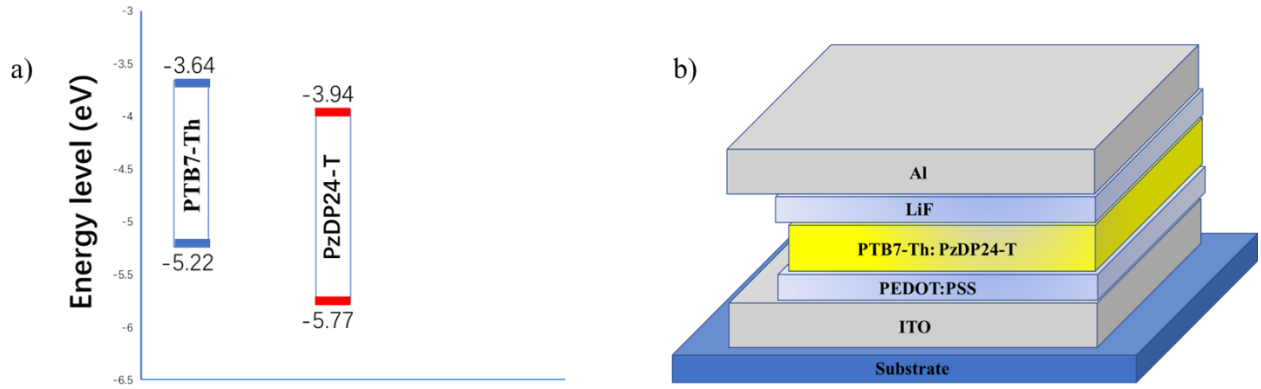

Figure 2-11 a) The energy level alignment of the PzDP24-T and PTB7-Th; b) Schematic representation of the solar cell device structure.

The device configuration was ITO/PEDOT: PSS/PTB7-Th: PNDIOT/LiF/Al. (**Figure 2-11**) As preliminary device fabrication, we used chlorobenzene as the processing solvent for the active layer. Initially, the optimal donor/acceptor ratio was determined 1:1 with a best PCE of 0.19% (**Table 2-2**). We noticed that it was difficult to process PzDP24/ PTB7-Th into a uniform thin film in chlorobenzene (10 mg/ml) because PzDP24-T was suffered from limited solubility in chlorobenzene. Then we tried to further change the spin coating solvent to dichlorobenzene to optimize the performance of the solar cell. For dichlorobenzene, the optimal donor/acceptor (D/A) ratio was determined to be 1:1, respectively, where the best PCE of 0.3% was realized (V_{OC} = 0.76 V, J_{SC} = 1.27 mA cm^{-2}, and FF = 0.31) (**Figure 2-12**). In addition, we tried to perform annealing treatment for 10 min on the polymer blend, as thermal annealing has proven to be a successful method to improve J_{SC} and FF.[97] However, the PCE of those devices decreased remarkably due to lower J_{SC} and FF (**Table 2-3**), which suggests thermal annealing is not required for PzDP24-T based solar cells.

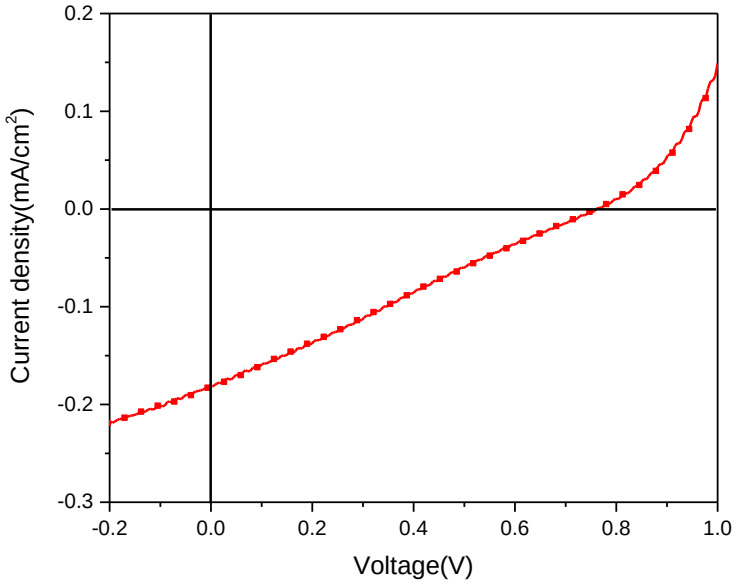

Figure 2-12 The J-V characteristic for the solar cell device based on PzDP24-T: PTB7-Th. The active layer (1:1 weight ratio) was spin-coated using a solution (10 mg/ml) in o-dichlorobenzene at 1500 rpm.

Table 2-2 The optimization of donor/acceptor ratio and solvent in the active layer.

Solvent	Donor/Acceptor ratio	J_{SC} (mA/cm^2)	V_{OC} (V)	FF	PCE (%)
CB	1:1	1.04	0.62	0.30	0.19
	1:1.5	1.02	0.59	0.27	0.16
	1.5:1	1.01	0.63	0.28	0.18
o-DCB	1:1	1.26	0.75	0.31	0.30
	1:1.5	1.02	0.67	0.30	0.21
	1.5:1	1.14	0.56	0.36	0.23

Table 2-3 Device performance optimization through post-treatment.

Post-treatment	J_{SC} (mA/cm^2)	V_{OC} (V)	FF	PCE (%)
None	1.26	0.75	0.31	0.30
Solvent-annealing	1.16	0.64	0.27	0.20

To further understand the low performance of PzDP24-T-based devices, we used AFM to investigate the morphology of the PzDP24-T: PTB7-Th blend under the same conditions to prepare the solar cell devices. (**Figure 2-13**) The AFM image showed PzDP24-T: PTB7-Th based cell has coarsened morphology with average root mean-square surface (RMS) roughness 6.23 nm in chlorobenzene. (**Figure 2-13a**) The large roughness could partially explain the low J_{SC} because it is detrimental to charge carrier transport and collection.[42] Moreover, large phase-separated fabric structure can be observed in the blend film with size over 1 μm. A plausible reason is the poor solubility of PzDP24-T polymer, giving insufficient donor/acceptor intermixing at nanometer scale. The oversized phase segregation has negative impact on the exciton dissociation at the D-A interface because the exciton diffusion length is around 10 nm, which indicates the ideal domain width should be about 20 nm.[98] In contrast, the blend film spin-coated in dichlorobenzene exhibited lower RMS value (5.14 nm) and smaller aggregation domains (**Figure 2-13b**), leading to relatively high J_{SC} and overall PCE. On the other hand, there is still room for further improvement of the photovoltaic properties by decreasing the domain sizes of the phase separation through strategies such as cosolvents[67] and processing additives[99].

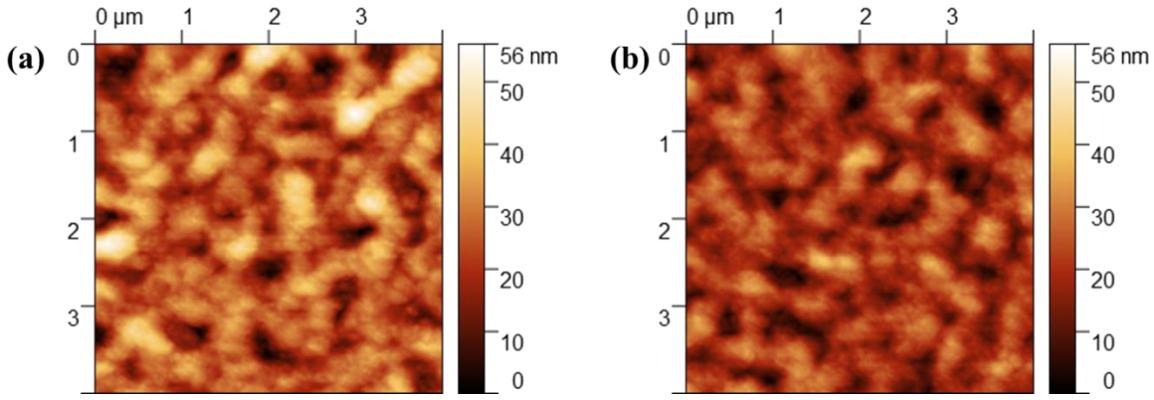

Figure 2-13 AFM height images (4 µm × 4 µm) of PTB7-Th: PzDP24-T blend films spin-coated on PEDOT: PSS/ITO substrates processed with (a) chlorobenzene (b) o-dichlorobenzene**.**

The blend surface morphology observed by AMF does not represent the entire bulk morphology due to the absence for vertical morphology. Thus, further investigation is necessary to understand the performance of PzDP24-T based devices. Then we measured the charge transport properties of the PTB7-Th: PzDP24-T blend films by the space-charge-limited current (SCLC) technique. The hole-only device was composed of ITO/PEDOT:PSS/polymer blend/MoO_3/Ag while electron-only device consisted of ITO/ZnO/polymer blend/LiF/Al. (**Figure 2-14**) The charge carrier mobility was calculated by fitting the J-V curves in the near quadratic region according to the modified Mott-Gurney equation:

$$J = \frac{9}{8}\mu\varepsilon\varepsilon_0\frac{V^2}{L^3}$$

Where L is the thickness of the polymer blend films, ε_0 is vacuum dielectric constant and ε is approximately 3 for organic semiconductors. Hole and electron mobilities of PTB7-Th: PzDP24-T blend films were determined to be 2.64×10^{-5} cm^2 V^{-1} s^{-1} and 9.18×10^{-7} cm^2 V^{-1} s^{-1} respectively (**Figure 2-15**). We noted that the electron mobility was over an order of magnitude lower than that of the hole mobility. It is known that the critical requirement for high performance solar cell to achieve balanced hole/electron carrier mobilities, so both charge carriers can be collected equally in unison.[100] The unbalanced hole/electron charge transport due to the low electron mobility could be the reason of low FF of the devices.[101]

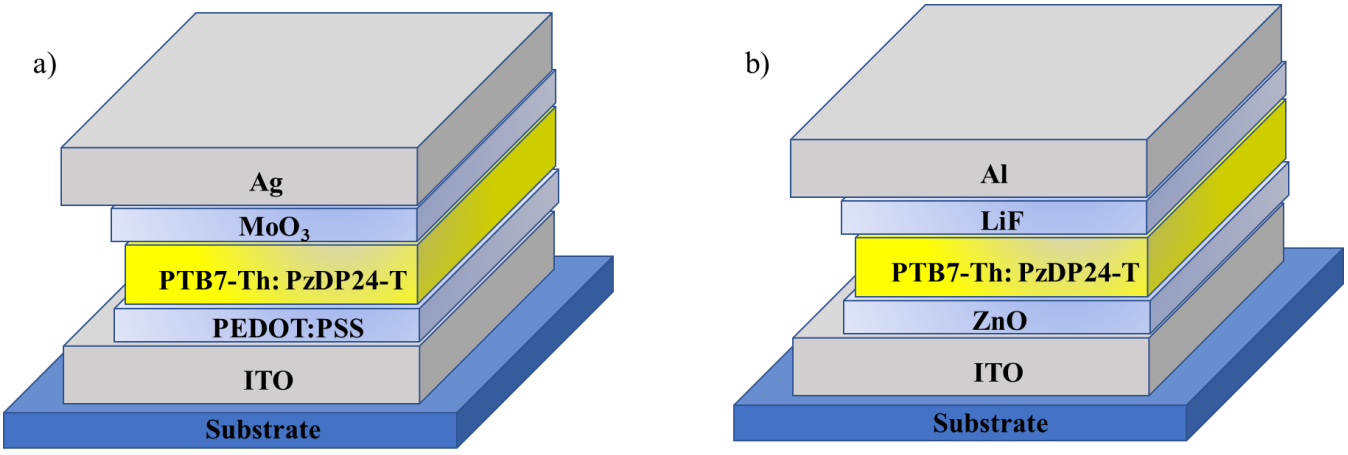

Figure 2-14 Schematic representation of the SCLC devices structure: a) hole-only; b) electron-only.

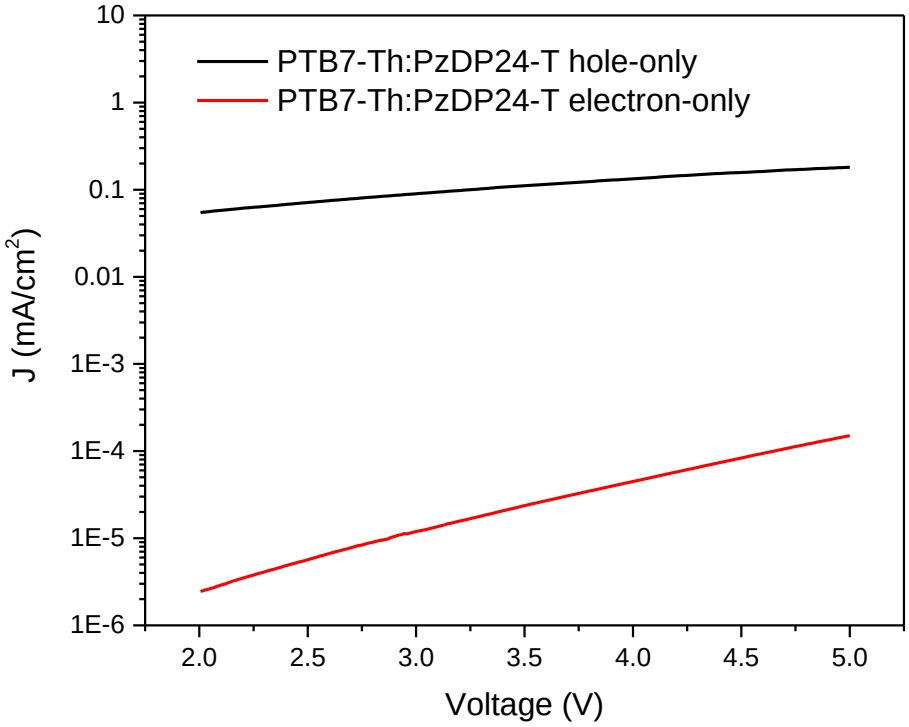

Figure 2-15 The J-V characteristics of the electron-only and hole-only devices for PTB7-Th: PzDP24-T.

In addition, reflective X-ray diffraction (XRD) measurement was used to investigate the

packing of individual neat film. The PzDP24-T neat film showed no appreciable long-range order diffraction peaks (**Figure 2-16**), indicating almost completely amorphous morphology. This result is also supported by DSC traces, which showed no glass transition and no melting peak. The reason of disorder packing property of PzDP24-T is probable that the zigzagged structure of thiophene have induced noncoplanar backbone and imposed large steric hindrances for the polymer chains.[102][103] These results suggested that polymer PzDP24-T film has poor crystallinity, which have negative impact on the J_{SC}. It have been evidenced that relatively good crystallinity is the typical target during device processing because of the high carrier mobility and high light absorption in ordered molecular systems.[104][105] For example, Marcel mentioned that, for P3HT: P(NDI2OD-T2) blends, relatively crystalline acceptor (P(NDI2OD-T2)) is benefit to the charge carrier separation.[106] Moreover, in the polymer blend of solar cell, as the electron transport is mainly undertaken by the acceptor (PzDP24-T), the intrinsic disordered packing property of PzDP24-T could explain the low electron mobility for SCLC, corresponding to unbalanced hole/electron charge transport.

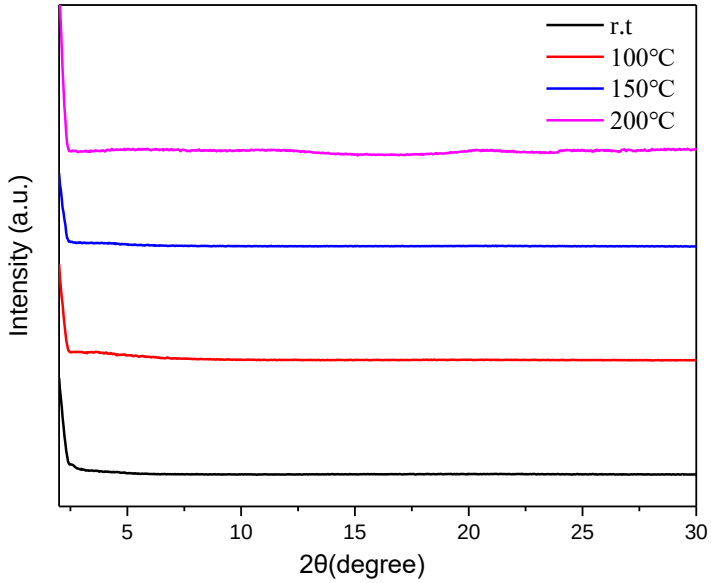

Figure 2-16 XRD spectra obtained from the spin-coated PzDP24-T thin films on DDTS-modified SiO_2/Si substrates annealed at different temperatures.

2.4 Balanced Ambipolar Polymers PzDP16-BDT

2.4.1 Preparation of PzDP16-BDT

Due to the very strong intermolecular interaction, PzDP-based polymers suffer from poor solubility in OPV application. According the previous study, the copolymer of C20-substituted PzDP and thiophene (T), PzDP20-T, was completely insoluble in several common solvents, whereas PzDP24-T also showed limited solubility. Moreover, further longer and branched side chains can result in diminishing lower charge transport property and lower overall performance.[42] Hence, in order to overcome this problem, we developed the D-A copolymer of PzDP unit and alkyl-thiophene-substituted benzo[1,2-b:4,5-b′]dithiophene (BDT), PzDP-BDT. Introducing BDT unit can not only improve the solubility of PzDP-based polymers due to the presence of alkyl side chains, but also provide promising merits. Firstly, BDT unit is a planar conjugated molecule and easily forms π-π stacking, which is benefit to high mobility.[107] Secondly, for BDT, the small steric hindrance between adjacent units makes it an ideal conjugated unit for high PCE material design.[108]

The additional side chains in BDT units allowed PzDP-BDT polymers substitute shorter side chains than PzDP-T. In this regard, we synthesized three PzDP-BDT polymers with these three side chains with different branch length via Stille coupling, which are named PzDP20-BDT, PzDP16-BDT and PzDP12-BDT, respectively (**Figure 2-17**). Among the three polymers, PzDP20-BDT yielded 95% in hexane whereas PzDP12-BDT was not soluble during Soxlet extraction, which exhibits the side chains were oversize or skimpy. Besides, PzDP16-BDT showed opportune and excellent solubility in several common organic solvent, such as chloroform, chlorobenzene and dichlorobenzene.

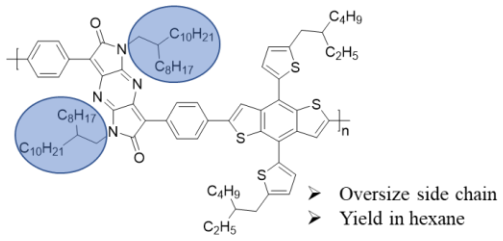

PzDP20-BDTTT8

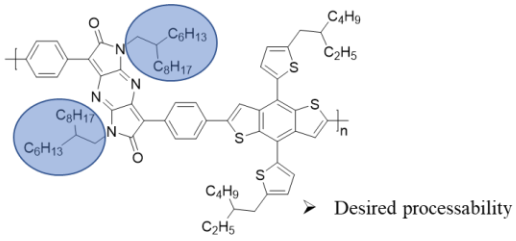

PzDP16-BDTTT8

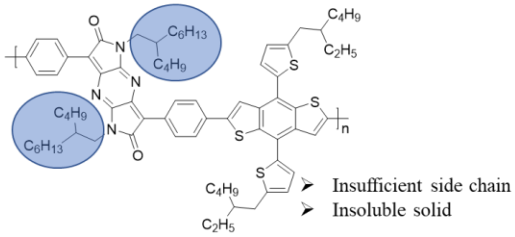

PzDP12-BDTTT8

Figure 2-17 The comparison PzDP-BDT copolymers with three different alkyl chains.

2.4.2 Characterization of PzDP16-BDT

The number average (Mn) and polydispersity index (PDI) was determined to be 24.6 kDa and 3.14, respectively, using HT-GPC at a column temperature of 140 °C with 1,2,4-trichlorobenzene as eluent and polystyrene as standards (**Figure 2-18**).

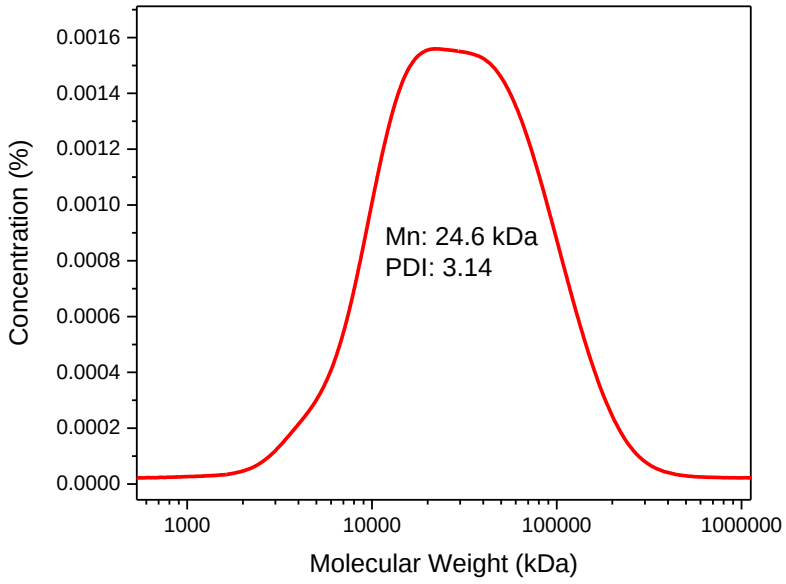

Figure 2-18 The molecular weight distribution for PzDP16-BDT obtained by HT-GPC.

The thermal stability and crystallinity of PzDP16-BDT was characterized by TGA and DSC, respectively. The polymer exhibited a good thermal stability with a 2% weight loss at 435 ℃ (**Figure 2-19**). DSC curve of PzDP16-BDT showed neither obvious exothermic nor endothermic signals, indicating the absence of crystalline domain (**Figure 2-20**).

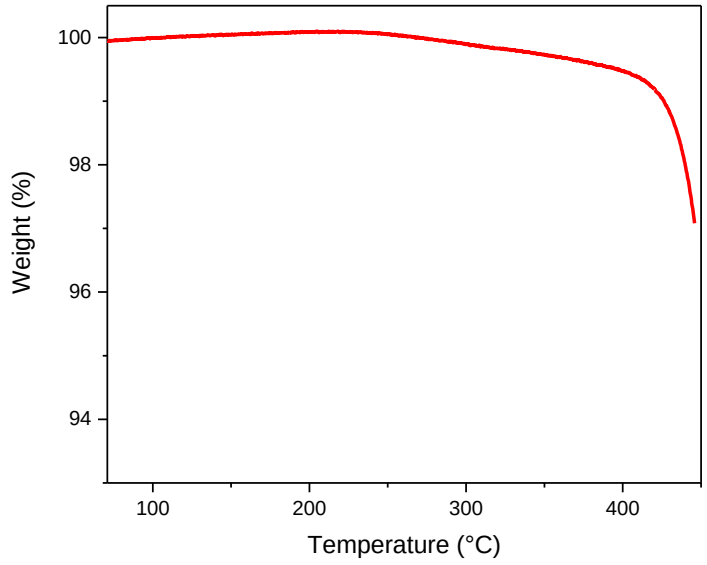

Figure 2-19 TGA curve of PzDP16-BDT measured with a heating rate of 10 °C min^{-1} under nitrogen.

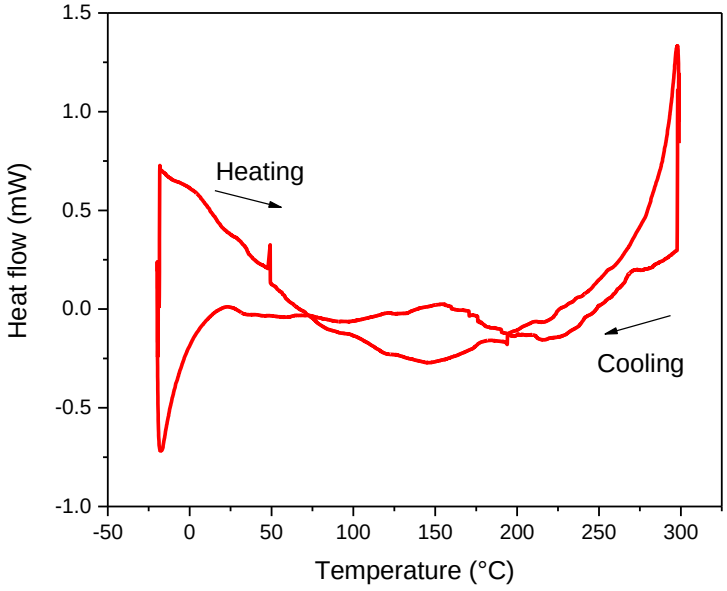

Figure 2-20 Differential scanning calorimetry (DSC) profiles of PzDP16-BDT obtained at a scanning rate of 10 °C min^{-1} under nitrogen.

Figure 2-21 shows the UV-vis-IR absorption spectra of PzDP16-BDT for both the dilute solution (~ 10^{-6} M in chloroform) and as-spun film. There are two distinctive peaks can be observed in both absorption spectra. The absorption bands in the high energy region from 300 nm to 400 nm are attributed to the delocalized excitonic π-π* transition. The broad bands in the low energy region from 650 nm to 800 nm are assigned to intramolecular charge transfer (ICT) interactions between the donor and acceptor units in the building blocks of polymers. PzDP16-BDT shows the maximum absorption wavelength at 754 nm in solution. In solid films, the maximum absorption peak is blue-shifted from 754 nm to 703 nm, which is an indication of the dominance of H-aggregate. The onset absorption edges as the thin films for PzDP16-BDT is 867 nm, corresponding to an optical bandgap of 1.43 eV.

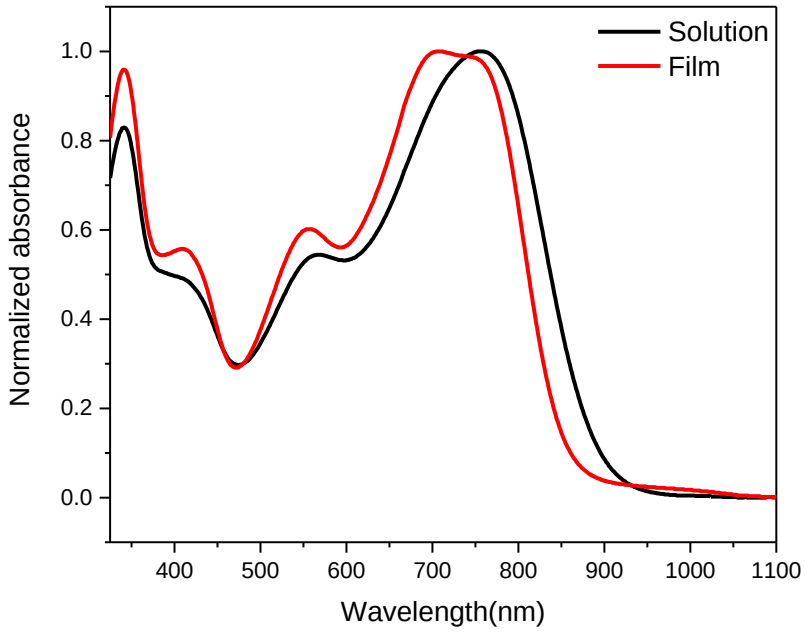

Figure 2-21 The UV-Vis-IR absorption spectra of PzDP16-BDT in diluted solution (chloroform) and in thin film.

As shown in **Figure 2-22**, both n-doping and p-doping processes of PzDP16-BDTTT are

reversible. The CV curve of PzDP16-BDT presents an onset reduction potential at -0.80 eV vs Ag/Ag^+ and an onset oxidation potential at 0.86 eV vs Ag/Ag^+. The HOMO and the LUMO levels of the polymer calculated to be -5.60 eV and -3.94 eV, respectively. Owing to the stronger electron accepting effect of the PzDP moiety, the energy levels are notably lower compared to those of their corresponding DPP-based polymers with the same BDT leakage, which is in good agreement with the previous study of PzDP24-T.

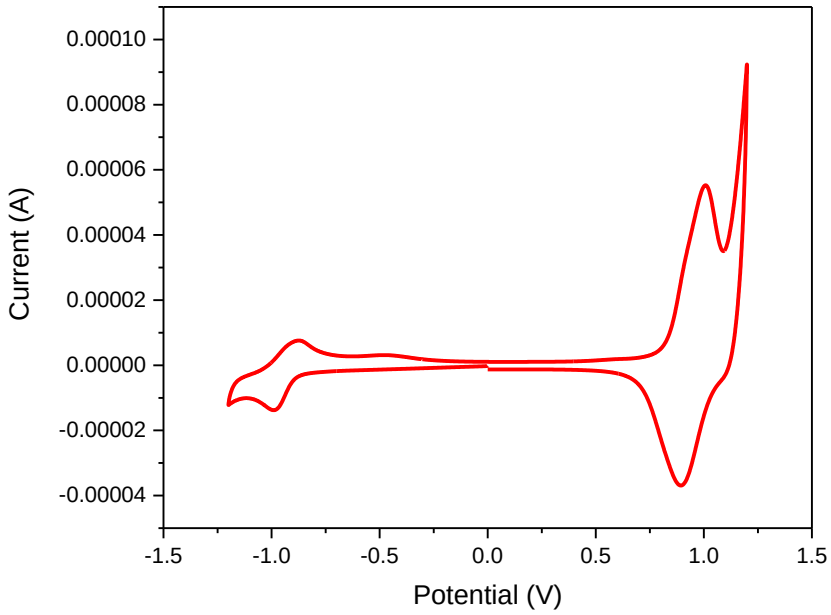

Figure 2-22 Cyclic voltammogram of PzDP16-BDT in a 0.1 M tetrabutylammonium hexafluorophosphate solution in acetonitrile.

The same device configuration applied in characterization of PzDP24-T was used to evaluate PzDP16-BDT as a channel semiconductor in BGBC OTFT. The polymer PzDP16-BDT showed balanced ambipolar charge transport behavior (**Table 2-4**). When PzDP16-BDT was annealed from 50 °C to 150 °C for 30 min, both hole and electron mobilities gradually increased. However, further increasing the annealing temperature to 200 °C caused degeneration for p-type/n-type carrier mobilities. The best performance was achieved at 150 °C with the highest hole and electron mobilities up to 0.0022 $cm^2\ V^{-1}\ s^{-1}$and 0.0025 $cm^2\ V^{-1}\ s^{-1}$,

respectively. It can be noticed that the polymer PzDP16-BDT showed lower charge performance than the polymer PzDP24-T. For the polymer PzDP16-BDT, the presence of side chains on BDT can significantly improve the solubility. However, in the solid state (film), the excessively strong side chain interaction might hinder the π-π stacking of the polymer main backbones.[109]

Table 2-4 The summary of BGBC OTFT performance of PzDP16-BDT.

$T_{annealing}$ (°C)	**Hole mobility [a] ($cm^2 V^{-1} s^{-1}$)**	**Electron mobility [a] ($cm^2 V^{-1} s^{-1}$)**
RT	0.00054± 0.00023 (0.00074)	0.00038± 0.00016 (0.00054)
50	0.00074± 0.00033 (0.00107)	0.00050± 0.00014 (0.00064)
100	0.0014± 0.0003 (0.0017)	0.00093± 0.0003 (0.0012)
150	0.0015± 0.0004 (0.0022)	0.0015± 0.001 (0.0025)
200	0.00012± 0.00021 (0.00033)	0.0012± 0.0003 (0.0015)

[a] The average mobility ± standard deviation (maximum mobility) calculated from the saturation regions of five devices.

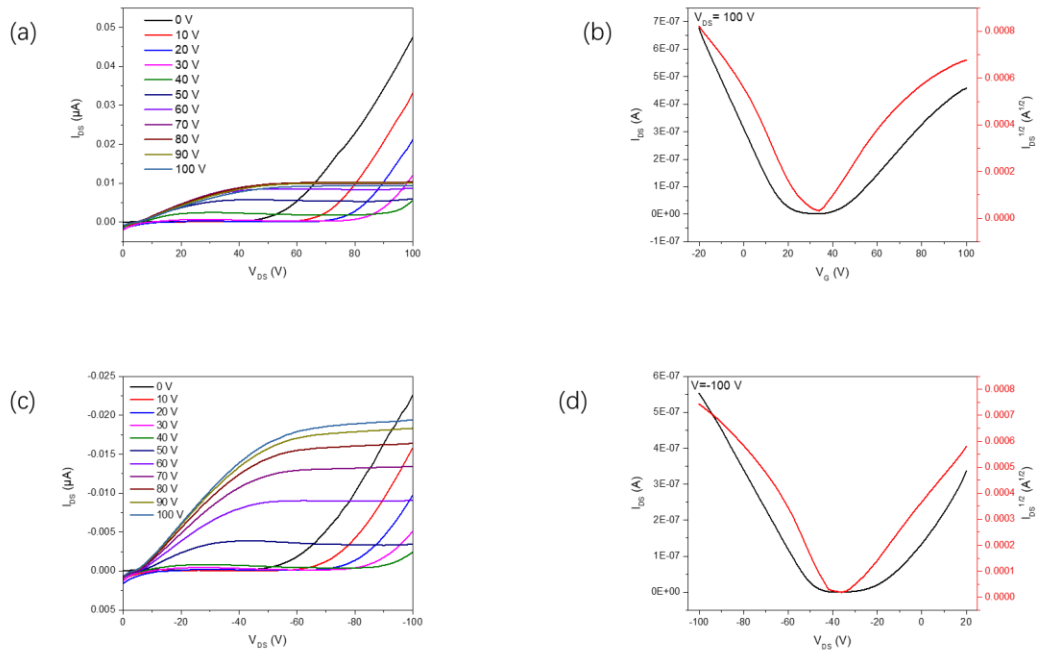

Figure 2-23 The output curves (a)/(c) in the electron/hole enhancement mode. The transfer curves (b)/(d) in the electron/hole enhancement mode. The BGBC OTFT devices with 150 °C-annealed PzDP16-BDT films. Device dimensions: channel length (L) = 30 μm; channel width (W) =1000 μm.

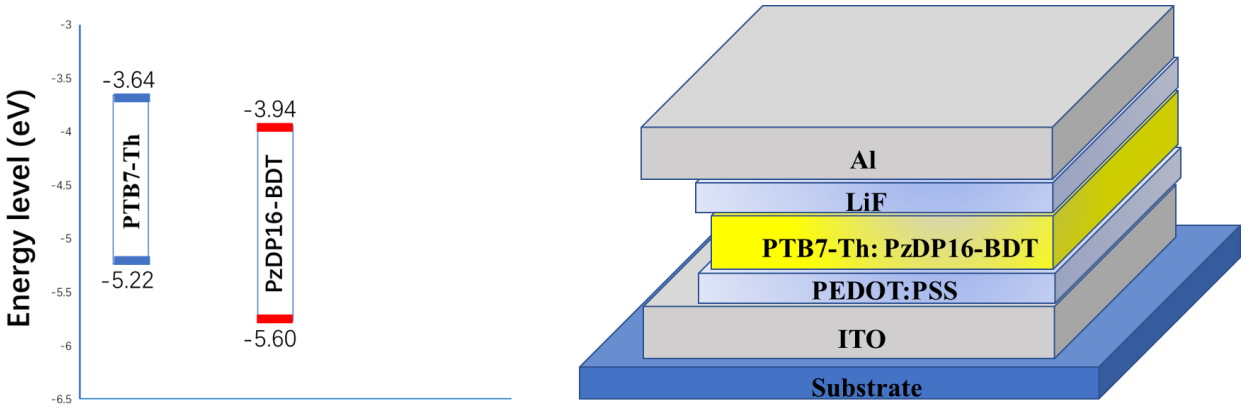

Figure 2-24 a) The energy level alignment of the PzDP16-BDT and PTB7-Th; b) Schematic representation of the solar cell device structure.

In addition, given that LUMO/HOMO offsets between PzDP16-BDT and PTB7-Th are larger than 0.3 eV, the polymer was used as electron acceptor with PTB7-Th as electron donor to

fabricate all-PSC with the same device structure of PzDP24-T. (**Figure 2-24**) Different D/A ratios (w/w) 1:0.8, 1:1 and 0.8:1, were scanned. Chlorobenzene and o-DCB were used as solvent to make the solutions. We also tried fabricating the devices in air and nitrogen conditions. The detailed photovoltaic data are listed in **Table 2-5** and **Table 2-6**. It can be seen that the optimum device for PzDP16-BDT/PTB7-Th is spin-coated in chlorobenzene with D/A ratio 1:0.8 under nitrogen, and the best power conversion efficiency (PCE) value of 1.55% (J_{SC} = 5.64 mA/cm^2, V_{OC} = 0.72, FF = 0.38) was obtained under this condition (**Figure 2-25**). Moreover, thermal annealing was also tried to improve the device performance. However, after annealing at 100 °C for 10 min, those devices showed a significant drop in performance. (**Table 2-7**)

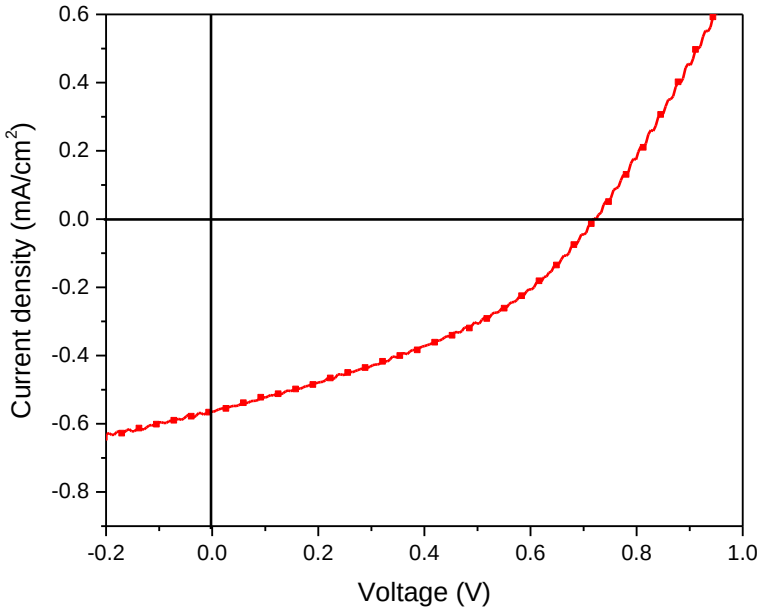

Figure 2-25 The J-V characteristic for the solar cell device based on PzDP24-T: PTB7-Th. The active layer (1:0.8 weight ratio) was spin-coated using a solution (12.5 mg/ml) in o-dichlorobenzene at 1500 rpm.

Table 2-5 Device performance optimization through donor/acceptor ratio.

Solvent	Donor/Acceptor ratio	Environment	J_{SC} (mA/cm^2)	V_{OC} (V)	FF	PCE (%)
CB	1:1	Nitrogen	4.80	0.70	0.34	1.15
CB	1:0.8	Nitrogen	5.64	0.72	0.38	1.55
CB	0.8:1	Nitrogen	3.73	0.72	0.37	1.00
o-DCB	1:1	Nitrogen	2.85	0.73	0.32	0.68
o-DCB	1:0.8	Nitrogen	3.17	0.72	0.35	0.80
o-DCB	0.8:1	Nitrogen	2.54	0.73	0.32	0.59

Table 2-6 The summary of device performance in different environment.

Solvent	Donor/Acceptor ratio	Environment	J_{SC} (mA/cm^2)	V_{OC} (V)	FF	PCE (%)
CB	1:0.8	Air	4.01	0.72	0.37	1.09
CB	1:0.8	Nitrogen	5.64	0.72	0.38	1.55
o-DCB	1:0.8	Air	2.53	0.72	0.31	0.60
o-DCB	1:0.8	Nitrogen	3.17	0.72	0.35	0.80

Table 2-7 Device performance optimization through post-treatment.

Post-treatment	Solvent	Donor/Acceptor ratio	J_{SC} (mA/cm^2)	V_{OC} (V)	FF	PCE (%)
None	CB	1:0.8	5.64	0.72	0.38	1.55
Annealing	CB	1:0.8	0.64	0.71	0.35	0.16

Atomic force microscopy (AFM) measurements were carried out to study the surface

morphology of the thin film blends. As shown in **Figure 2-26**, the PTB7-Th: PzDP16-BDT polymer blends spin-coated from o-dichlorobenzene show a phase separated surface morphology with large domain sizes of 200 - 300 nm as well as a large RMS of 3.5 nm (**Figure 2-26b**), which is not ideal for efficient exciton dissociation. In contrast, the film blends dissociated from chlorobenzene present a phase-separated surface morphology with domain sizes of around 100 nm and a relatively small RMS 0.86 nm (**Figure 2-26a**), which is more favorable for efficient charge photogeneration. These results are also in good agreement with the photovoltaic performance in terms of J_{SC}, FF values of these all-polymer solar cells. Compared with PzDP24-T-based devices, the observed optimized morphology of PzDP16-BDT is attributed to better miscibility of the acceptor polymer and donor polymer because of its enhanced solubility for solar cell fabrication.

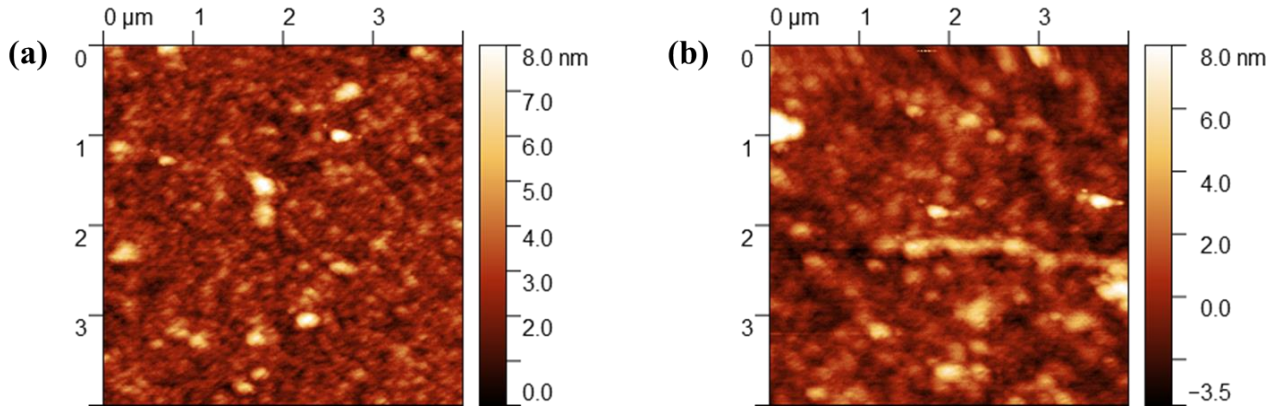

Figure 2-26 AFM height images (4 µm × 4 µm) of PTB7-Th: PzDP16-BDT blend films spin-coated on PEDOT: PSS/ITO substrates processed with (a) chlorobenzene (b) dichlorobenzene.

Further, the molecular orientation of the polymer PzDP16-BDT films was investigated by using the reflective X-ray diffraction technique (**Figure 2-27**). XRD patterns of different annealing temperature showed no appreciable diffraction peaks, indicating amorphous morphology. The poor crystallinity is likely caused by those redundant side chains so that steric hindrance disturbs the conjugation of the backbone, resulting in intrinsic disordered packing property.[110] In generally, poor crystallinity is related to low charge-transport character, which was further investigated by SCLC measurement with the same fabrication in the previous chapter (**Figure 2-28**). The hole-only and electron-only mobilities were calculated to

be 1.10 × 10^{-5} cm^2 V^{-1} s^{-1} and 2.39 × 10^{-7} cm^2 V^{-1} s^{-1}, respectively. (**Figure 2-29**) Thus, the lower electron mobility of the PTB7-Th: PzDP16-BDT blend is still one of the key limiting factors in the performance of PSCs.

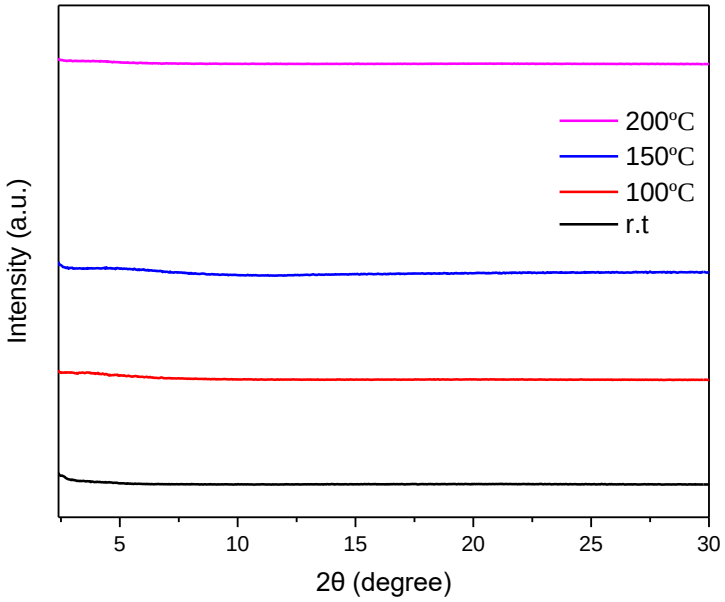

Figure 2-27 XRD spectra obtained from the spin-coated PzDP16-BDT thin films on DDTS-modified SiO_2/Si substrates annealed at different temperatures.

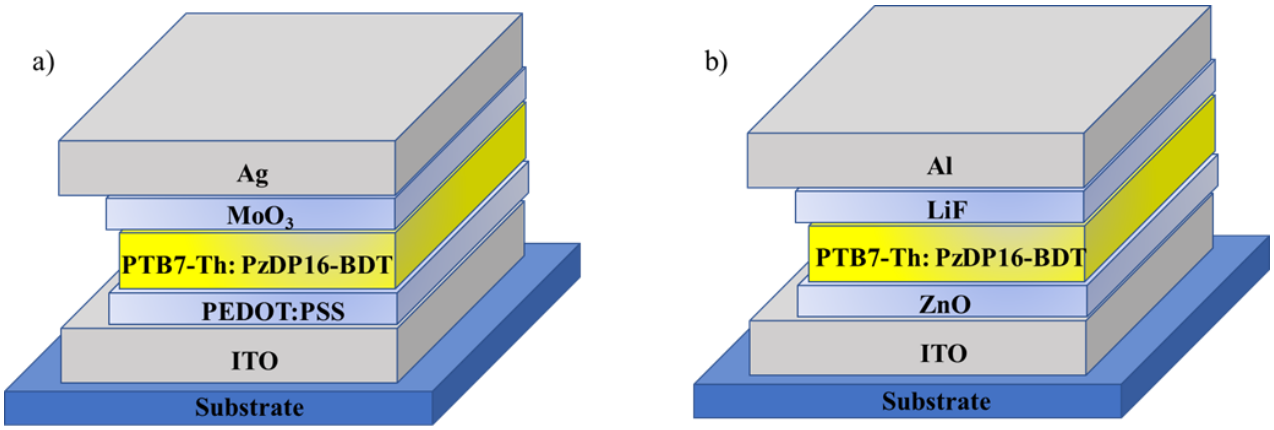

Figure 2-28 Schematic representation of the SCLC devices structure: a) hole-only; b) electron-only.

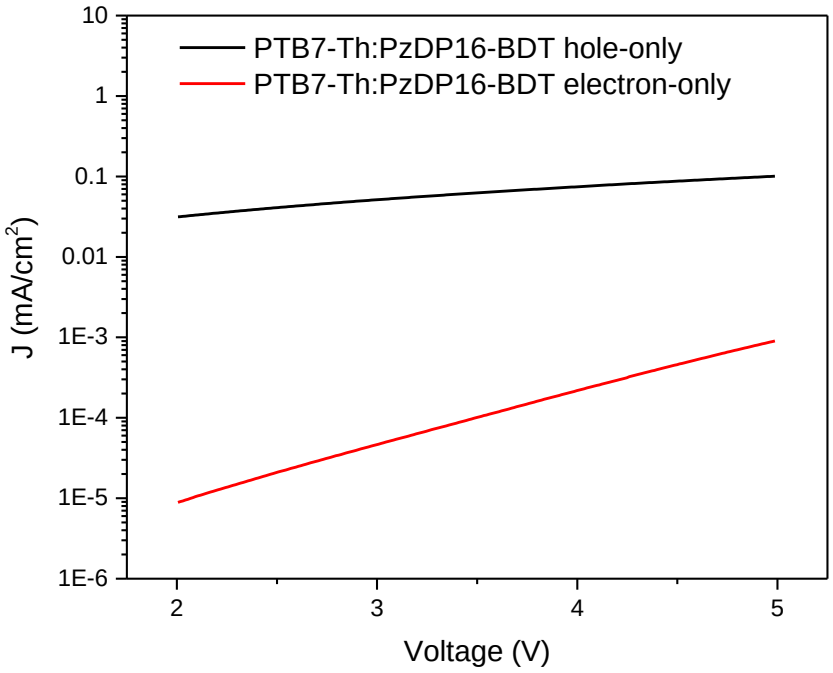

Figure 2-29 The J-V characteristics of the electron-only and hole-only devices for PTB7-Th: PzDP16-BDT.

2.5 Conclusion

In conclusion, two PzDP-based conjugated polymers named as PzDP24-T and PzDP16-BDT were designed and synthesized, which demonstrated suitable solubility by optimizing different lengths of side chain. With the electron-deficient effect of pyrrolinone groups, the PzDP24-T and PzDP16-BDT exhibited lower LUMO (-3.94 eV and -3.91 eV) compared with DPP-based polymers with same donor linkages. The lower LUMO energy levels can facilitate electron injection and thus provide stable n-type performance, which is necessary for the acceptor of all-PSCs. Herein, PzDP24-T showed n-type dominant charge transport properties in OTFTs with electron mobility up to 2.9×10^{-2} cm^2 V^{-1} $s^{-1}cm^2$ V^{-1} s^{-1}, whereas PzDP16-BDT exhibited ambipolar charge transport behavior with balanced electron/hole mobilities up to 2.2×10^{-3} cm^2 V^{-1} $s^{-1}/2.5 \times 10^{-3}$ cm^2 V^{-1} s^{-1}. When the polymers applied in PSCs, a PCE of 0.3% was recorded in the PSC device based on PTB7-Th/PzDP24-T. AFM images suggested there were

large phase preparation with large RMS roughness present in polymer blends, which might be due to poor miscibility at nanometer scale. This has limited the charge generation that happens at the D-A interface, and thus led to a very low J_{SC}. On the other hand, a smaller domain size and smoother roughness could be observed in PTB7-Th/PzDP16-BDT blend, and the PCE of devices based on PTB7-Th/PzDP16-BDT improved to 1.57%. However, through XRD and SCLC studies, we found that both PzDP24-T and PzDP16-BDT exhibited intrinsic disordered packing property thus leading to unbalanced charge transport in the polymer blends, which might have negative impact on the performance of those all-PSC devices. Therefore, to further improve the performance of PzDP-based polymers as acceptor in OSCs, the future work should focus on introducing higher planar unit into the polymer backbone (such as thiophene-vinylene-thiophene) and tuning the lengths of side chain to obtain an eligible balance between crystallinity and solubility.

2.6 Experimental

2.6.1 Materials and Characterization

All chemicals were purchased from commercial sources and used without further purification. Computational simulations were performed with density function theory (DFT) calculation with the 6-311G + (d, p) basis set and all the orbital pictures were obtained using Gauss-View 5.0 software. GPC measurements were performed on a Waters SEC system using 1,2,4-trichlorobezene as eluent and polystyrene as standards at 140 °C. TGA measurements were carried out on a TA Instruments SDT 2960 at a scan rate of 10 °C min^{-1} under nitrogen. The UV-Vis-IR absorption spectra of polymers were recorded on a Thermo Scientific model GENESYS™ 10S VIS spectrophotometer. Cyclic voltammetry (CV) data were obtained on a CHI600E electrochemical analyzer using an Ag/AgCl reference electrode and two Pt disk electrodes as the working and counter electrodes in a 0.1 M tetrabutylammonium hexafluorophosphate solution in acetonitrile at a scan rate of 100 mV s^{-1}. Ferrocene was used as the reference, which has a HOMO energy value of -4.8 eV. NMR data was recorded with a Bruker DPX 300 MHz spectrometer with chemical shifts relative to tetramethyl silane (TMS, 0 ppm). Transmission XRD measurements were carried out on a Bruker Smart 6000 CCD 3-

circle D8 diffractometer with a Cu RA (Rigaku) X-ray source (λ = 0.15406 nm) and the polymer flakes stacked between two Mylar substrates. Atomic force microscopy (AFM) images were taken on polymer thin films spin-coated on the DDTS-modified SiO_2/Si substrates with a Dimension 3100 scanning probe microscope

2.6.2 Fabrication and Characterization of OTFT Devices

A bottom-gate bottom-contact (BGBC) configuration was used for all OTFT devices. The preparation procedure of the substrate and device is as follows. A heavily n-doped SiO_2/Si wafer with ~ 300 nm-thick SiO_2 was patterned with gold source and drain pairs by conventional photolithography and thermal deposition. Then the substrate was treated with air plasma, followed by cleaning with acetone and isopropanol in an ultra-sonic bath. Subsequently, the substrate was placed in a solution of dodecyl trichlorosilane (DDTS) in toluene (3 % in toluene) at room temperature for 20 min. The substrate was washed with toluene and dried under a nitrogen flow. Then a polymer solution in chloroform (5 mg/ml) was spin-coated onto the substrate at 3000 rpm for 60 s to give a polymer film (~ 40 nm), which was further subject to thermal annealing at different temperatures for 20 min in a glove box. All the OTFT devices have a channel length (L) of 30 μm and a channel width (W) of 1000 μm, and were characterized in the same glove box using an Agilent B2912A Semiconductor Analyzer. The hole and electron mobilities are calculated in the saturation regime according to the following equation:

$$I_{DS} = \frac{\mu C_i W}{2L}(V_G - V_T)^2$$

where I_{DS} is the drain-source current, μ is charge carrier mobility, C_i is the gate dielectric layer capacitance per unit area (~ 11.6 nF cm^{-2}), V_G is the gate voltage, V_T is the threshold voltage, L is the channel length (30 μm), and W is the channel width (1000 μm).

2.6.3 Fabrication and Characterization of All-PSC Devices

All all-PSC devices were fabricated using the conventional configuration ITO/PEDOT: PSS/PTB7-Th: polymer acceptor/LiF/Al. ITO glass substrates were sonicated in water, acetone and IPA. Then the substrates were treated with plasma cleaning. A thin layer of PEDOT: PSS

(Al 4083) was deposited through spin coating at 4000 rpm and dried subsequently at 150 °C for 20 min in air. Then the substrates were transferred to a nitrogen glove box, where the polymer blend layer (~ 140 nm) was spin-coated onto the PEDOT: PSS layer. Finally, a thin layer of LiF (1 nm) and a layer of Al (100 nm) electrode were deposited in vacuum onto the substrate at P ≈ 5.0×10^{-6} Pa. The active area is 0.07 cm^2. The current density-voltage (J-V) characteristics of the all-PSCs were measured on an Agilent B2912A Semiconductor Analyzer with a Science Tech SLB300-A Solar Simulator. A 450 W xenon lamp and an air mass (AM) 1.5 filter were used as the light source.

2.6.4 Synthetic Procedures

General procedure for the synthesis of ethyl 2-(4-bromophenyl)-2-oxoacetate (Compound 1):

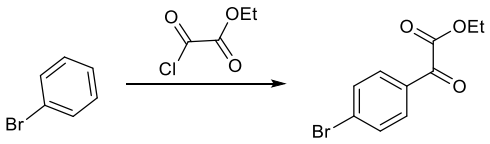

Anhydrous aluminum-trichloride (10 g, 0.075 mol) was added slowly to a stirred mixture of DCM (20 ml), ethyl 2-chloro-2-oxoacetate (10.24 g, 8.4 ml, 0.075 mol) and bromobenzene compound (7.85 g, 5.3 ml, 0.050 mol) cooled in an ice-bath, at such a rate as to maintain the reaction temperature below 10 ℃. After the addition was completed the reaction mixture was stirred at 10 ℃ for 1 hour and then at ambient temperature for 3 hours, after which it was poured carefully into a mixture of ice and water (150 ml). The aqueous layer was extracted with DCM (3 × 20 ml), and the organic layers was combined, dried by Na_2SO_4, filtered. After removing solvent, the product was purified by a very short column using hexane/DCM (1:1) and ethyl acetate, respectively.

Yield: 9.6 g, 75%.

^{1}H-NMR (300 MHz, chloroform-d, ppm) δ 7.90 (m, 2H), 7.66 (m, 2H), 4.45 (q, J = 7.1 Hz, 2H), 1.42 (t, J = 7.1 Hz, 3H)

General procedure for the synthesis of 1,4-diacetylpiperazine-2,5-dione (Compound 2):

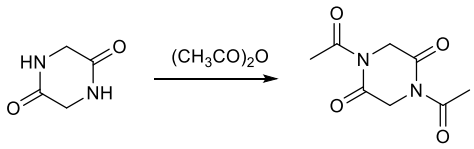

Glycine anhydride (11.41 g, 0.1 mol) was refluxed in acetic anhydride (50 mL) under argon for 11 h. The solvent was evaporated under reduced pressure, and the crude solid product was recrystallised from ethyl acetate and hexane and washed with methanol.

Yield: 16.0 g, 79%.

^{1}H-NMR (300 MHz, chloroform-d, ppm) δ 4.59 (s, 4H), 2.59 (s, 6H)

General procedure for the synthesis of diethyl 2,2'-(3,6-dioxopiperazine-2,5-diylidene) bis(2-(4-bromophenyl) acetate)) (Compound 3):

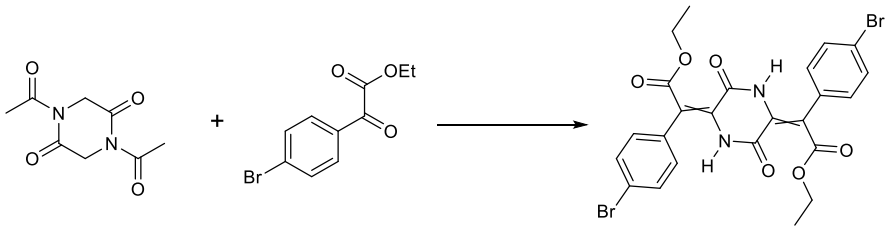

Under argon protection, a mixture of ethyl 2-(4-bromophenyl)-2-oxoacetate (3.86 g, 15 mmol), 1,4-diacetylpiperazine-2,5-dione (1.29 g, 6.5 mmol) and 3.5 ml triethylamine was heated at 55 - 60 ℃ overnight. After removing most of triethylamine under a reduced pressure, the residue was triturated and stirred in 10 ml of methanol for 12 h at room temperature, then filtered and washed with cold methanol to get a mixture of isomers.

Yield: 3.0 g, 79%.

^{1}H-NMR (300 MHz, chloroform-d, ppm) δ 11.91 - 11.75 (s, s, 1 + 2.2H), 8.05 - 6.96 (m, 25H), 4.34 - 4.13 (m, 12H), 1.35-1.15 (m, 18H).

General procedure for the synthesis of 3,7-bis(4-bromophenyl)dipyrrolo[2,3-b:2',3'-e]pyrazine-2,6 (1H,5H)-dione) (Compound 4):

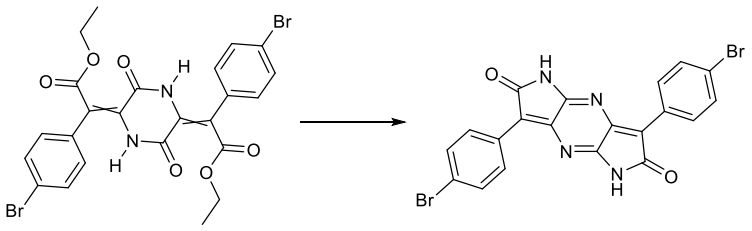

The precursors of (Compound 3) (3 g, 5 mmol) was heated in formamide (50 ml) at 150 ℃ overnight under argon protection. After cooling, 20 ml methanol was added, then washed by /DCM/acetone and filtered to give a dark red product.

Yield: 0.75 g, 25%.

^{1}H-NMR (DMSO-d_6, 300 MHz, ppm) δ 11.44 (s, 1H), 8.23 (d, 2H), 7.72 (d, 2H).

General procedure for the synthesis of 3,7-bis(4-bromophenyl)-1,5-bis(2-decyltetradecyl)dipyrrolo[2,3-b:2',3'-e]pyrazine-2,6(1H,5H)-dione (Compound 5-a):

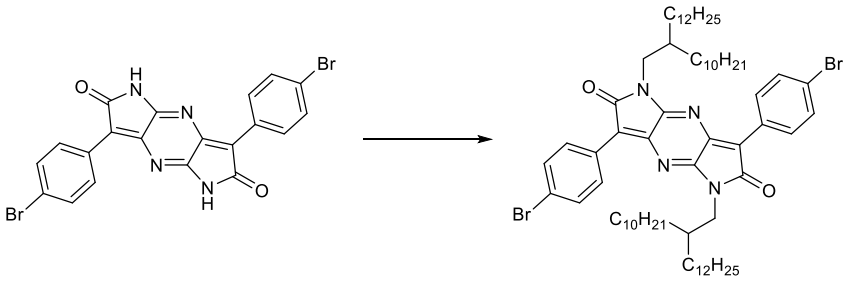

In a dry three-neck 25 ml round bottom flask, PzDP (Compound 3) (0.248 g. 0.5 mmol) and anhydrous K_2CO_3 (0.207 g, 1.5 mmol) were suspended in anhydrous N, N-dimethylformamide (DMF) (9 ml), Br-alky chain (1.55 mmol) was then added portionwise, and the reaction mixture was further stirred and heated overnight at 130 °C. The reaction mixture was allowed to cool down to room temperature, poured into water (80 ml), and stirred for 5 min. The product was extracted with ethyl acetate (40 ml × 3), then washed with water. Removal of the solvent afforded the crude product which was further purified using a silica-gel column (eluted with DCM: Hexane = 2:1 ~ 1:1). The residue was recrystallized with hot methanol.

Yield: 0.30 g, 51%.

^{1}H-NMR (300 MHz, chloroform-d, ppm) δ 8.37 (d, J = 8.7 Hz, 4H), 7.55 (d, J = 8.7 Hz, 4H),

3.62 (d, J = 7 Hz, 4H), 1.93 (s, 2H), 1.27 (m, 82H), 0.86 (t, J = 5.9 Hz, 12H).

Compounds 5-b to 5-e were synthesized with a similar synthetic procedure that was used for compound 5-a.

3,7-bis(4-bromophenyl)-1,5-bis(2-octyldodecyl)dipyrrolo[2,3-b:2',3'-e]pyrazine-2,6(1H,5H)-dione (Compound 5-b):

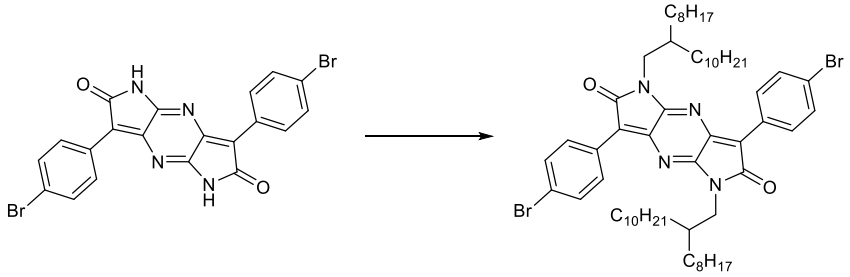

Yield: 0.32 g, 59%.

^{1}H-NMR (300 MHz, chloroform-d, ppm) δ 8.37(d, J = 8.7 Hz, 4H), 7.57 (d, J = 8.7 Hz, 4H), 3.63 (d, J = 7 Hz, 4H), 1.96 (s, 2H), 1.27 (m, 64H), 0.94 - 0.82 (m, 12H).

3,7-bis(4-bromophenyl)-1,5-bis(2-hexyldecyl)dipyrrolo[2,3-b:2',3'-e]pyrazine-2,6(1H,5H)-dione (Compound 5-c):

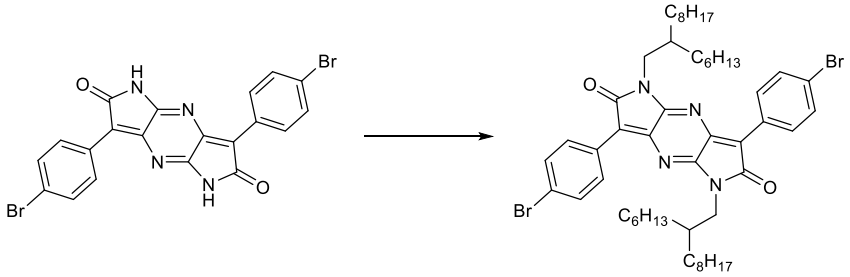

Yield: 0.28 g, 60%.

^{1}H-NMR (300 MHz, chloroform-d, ppm) δ 8.37 (d, J = 8.5 Hz, 4H), 7.57 (d, J = 8.6 Hz, 4H), 3.64 (d, J = 7.1 Hz, 4H), 1.94 (s, 2H), 1.28 (d, J = 22.1 Hz, 49H), 0.85 (t, J = 6.3 Hz, 12H).

3,7-bis(4-bromophenyl)-1,5-bis(2-butyloctyl)dipyrrolo[2,3-b:2',3'-e]pyrazine-

2,6(1H,5H)-dione (Compound 5-d):

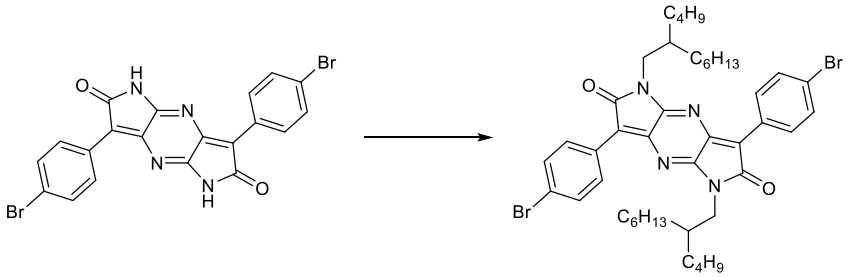

Yield: 0.26 g, 63%.

^{1}H-NMR (300 MHz, chloroform-d, ppm) δ 8.36 (d, J = 8.7 Hz, 4H), 7.56 (d, J = 8.7 Hz, 4H), 3.63 (d, J = 7.1 Hz, 4H), 1.94 (s, 2H), 1.27 (d, J = 22.0 Hz, 33H), 0.95 - 0.78 (m, 13H).

General procedure for the synthesis of polymer PzDP24-T:

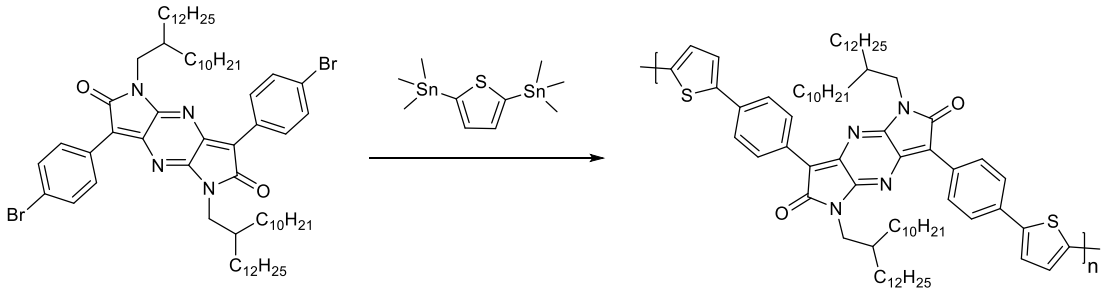

Compound 5-a (0.1306 g, 0.115 mmol) and 2,5-bis(trimethylstannyl)thiophene (0.0471 g, 0.115 mmol) were charged into a 25 ml flask. After degassing and refilling argon for 3 times, anhydrous toluene (6 ml) and bis(triphenylphosphine)palladium (II) dichloride (2 mg, 2.4% mol) were added and the reaction mixture was raised to 90 ℃ and stirred for 48 hours. After the mixture cold down, the mixture was poured into 100 ml methanol with stirring. After filtration, Soxhlet extraction by acetone, hexane and chloroform.

Yield:

Acetone extracted fraction: 0%.

Hexane extracted fraction: 10 mg, 8%.

Chloroform extracted fraction: 110 mg, 87%.

All PzDP-based Polymers were synthesized with a similar synthetic procedure that was used for PzDP24-T.

PzDP20-T:

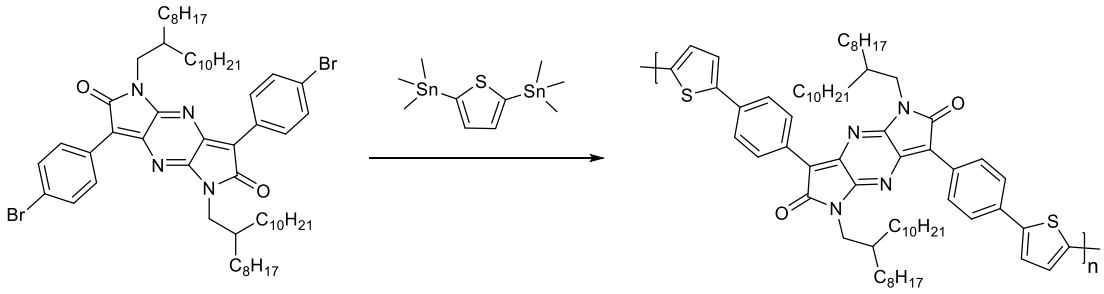

Yield:

Acetone extracted fraction: 0%.

Hexane extracted fraction: 0%.

Chloroform extracted fraction: 9 mg, 8%.

PzDP20-BDT:

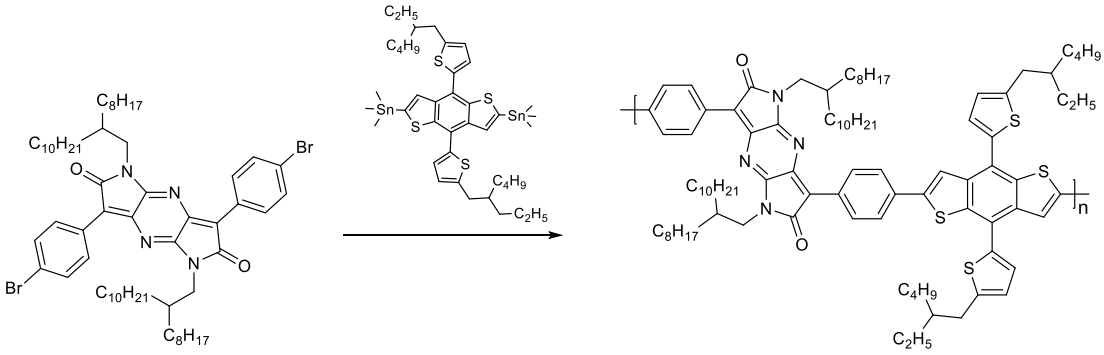

Yield:

Acetone extracted fraction: 0%.

Hexane extracted fraction: 100 mg, 88%.

Chloroform extracted fraction: 10 mg, 8%.

PzDP16-BDT:

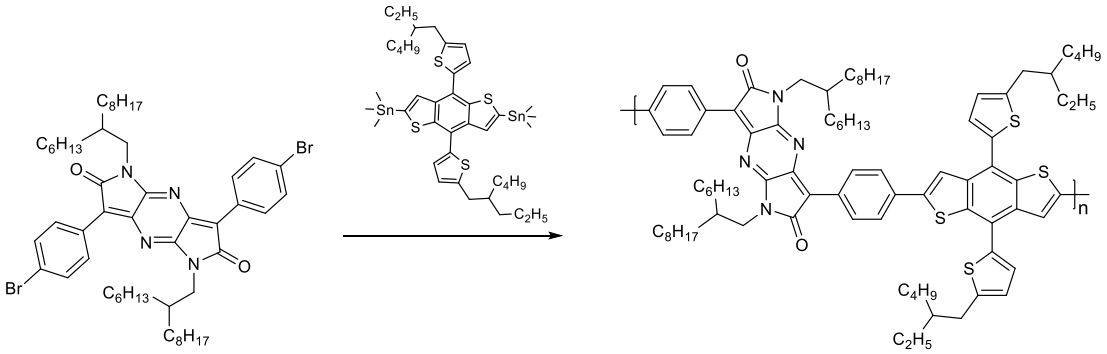

Yield:

Acetone extracted fraction: 0%.

Hexane extracted fraction: 0%.

Chloroform extracted fraction: 108 mg, 95%.

PzDP16-BDT:

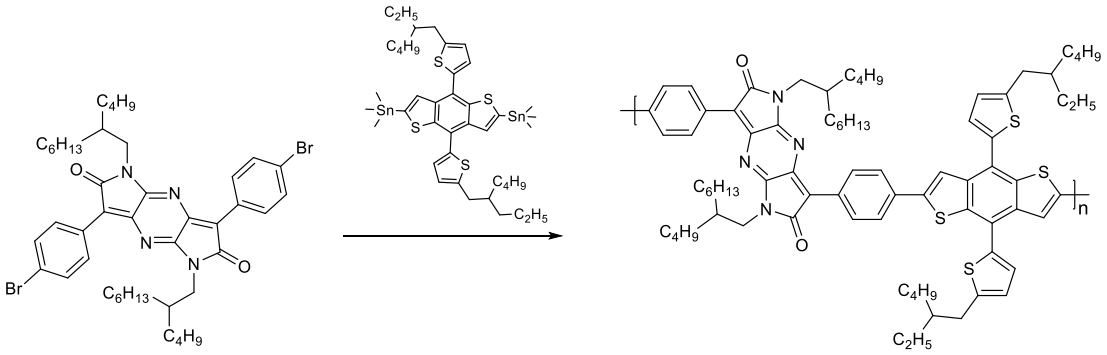

Yield:

Acetone extracted fraction: 0%.

Hexane extracted fraction: 0%.

Chloroform extracted fraction: 8 mg, 7%.

Chapter 3 Synthesis and Characterization of Novel Building Block TPT-based-polymer.

3.1 Introduction

The bulk heterojunction (BHJ) polymer solar cells, based on conjugated polymer donor and fullerene derivative acceptor, have attracted growing attraction due to their lightweight, low cost, flexible photovoltaic panels and potential application of mass-production.[111] Among the large variety of conjugated polymers donor materials, the most widely investigated one is regioregular poly(3-hexylthiophene) (P3HT).[112] However, the PCE of devices based on P3HT and PCBM blend, is limited by the relatively low V_{OC}, resulting from the high-lying HOMO level (-5 eV) of P3HT.[48] In addition, the relatively large bandgap of P3HT (~ 2.0 eV) causes inferior light harvest, which is unfavorable for high PCE.[47] Therefore, design and synthesis of novel photovoltaic polymers with deep HOMO energy level and broader absorption, is necessary to improve photovoltaic performance of PSCs. One of the successful methods to solve these issues is to alternate electron-withdrawing (acceptor) and electron-donating (donor) units in the polymer backbone, thereby reducing the bandgap. Besides, attaching electron-withdrawing segments on polymer backbone is efficient to modify a deep HOMO.[36][113] Functional groups containing nitrogen atom have been frequently utilized as electron-deficiency moieties to optimize molecular energy levels (HOMO and LUMO) of conjugated polymers.[114] For instance, quinoxaline, a heterocyclic conjugated unit with a ring complex made up of a benzene ring and a pyrazine ring, indicates significant electron-withdrawing property due to the strong electronegativity of the two nitrogen atoms in pyrazine. Quinoxaline-based polymers exhibited narrow band gaps and promising photovoltaic properties, which have achieved an outstanding PCE up to 11%.[115] However, pyridazine, as an isomeric structure with pyrazine, is one promising yet unexplored electron-deficient heterocycle for D-A conjugated copolymers with low-lying energy levels and narrow bandgap. In this work, a novel aromatic building block (TPT) with a pyridazine core have been designed and synthesized, and the characteristics of TPT-based polymer will be described.

The new aromatic compound TPT, namely 5,7-bis(octylthio)-1,4-di(thiophen-2-yl)thieno[3,4-

d]pyridazine, has a thieno-pyridazine core that incorporates two thiophene, where the substituted alkylthio chains could enable a good solubility for TPT-based polymers. As an analogue of pyrazine, pyridazine in the fused ring containing two electron-withdrawing nitrogen atoms provides high electron-accepting ability, which can be clearly observed in the computational simulation of TPT-Me molecule (**Figure 3-1**). The simulation results showed that the electrons of HOMO are averagely distributed in the entire molecule, whereas in the LUMO, the electrons are more concentrated around the thieno-pyridazine core. Meanwhile, the calculated HOMO and LUMO levels are -5.65 eV and -2.53 eV, respectively. The predicted low-lying energy levels indicate that the TPT moiety is a promising candidate to achieve deep HOMO for D-A polymers.

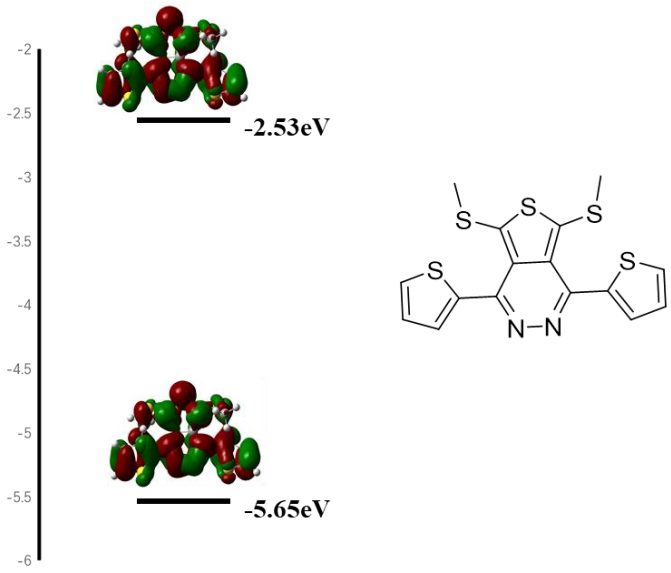

Figure 3-1 Predicted energy levels of TPT-Me.

3.2 Synthesis of Novel TPT Monomers and Related Polymer

As shown in **Scheme 3-1** and **3-3**, the TPT monomers can be easily prepared from simple ring closure procedure and condensation reactions (Route 1: non-brominated TPT) (Route 2: brominated TPT), their respective synthesis has been carried out as follows. Firstly, compound 1 was readily synthesized in excellent yields by one-step reaction of carbon disulfide and alkyl halide under mild reaction conditions in the presence of cesium carbonate as a basic system

and DMAc as the solvent.[116] In addition, we found that a trace amount of phase-transfer catalyst TBAI can improve the yield of desired product from 70% to 90%. Secondly, compound 2a-b was obtained by treating active the corresponding thiophene ketones with compound 1 in a mixture solvent (hexane/DFM, 5:1) with sodium hydride as the base.[117] Herein, the yield of 2a-b is very sensitive to the equivalent of sodium hydride. Therefore, systematic improvement was carried out in a series of experiment with different equivalent of sodium hydride, and the results are presented in **Table 3-1**.

Table 3-1 The compound 2a-b synthesis improvement results**.**

Experiment No.	Sodium hydride (eq)	Yield of 2a-b
1	1	25%
2	1.5	30%
3	2	10%
4	3	0

In addition, it is worth noticing that compound 2-b is not stable in silica gel and will partially decompose into thiol during silica gel column chromatography, which may arise from the weak acidity of silica gel surface. (**Figure 3-2**)

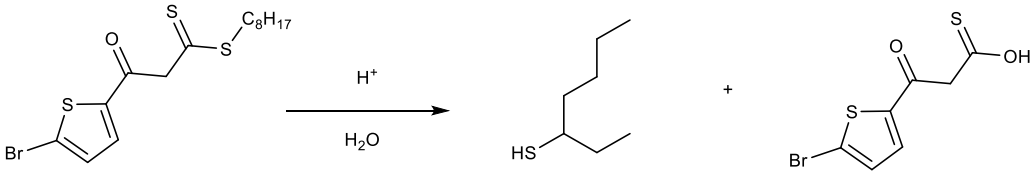

Figure 3-2 The compound 2-b can decompose into thiol in silica gel.

Thirdly, the synthesis of compound 3a-b involved an oxidative homodimerization reaction with N-chlorosuccinimide in DMSO.[118] Finally, compound 4a-b was synthesized through a condensation reaction with hydrazine monohydrate in acetic acid.[119]

In preliminary attempt, we had synthesized non-brominated TPT compound 4-a via route 1 and attempted to obtain brominated monomer 4-b by brominating 4-a. However, neither bromination in 4-a nor 3-a could yield related brominated product 4-b or 3-b in different

conditions (**Scheme 3-2**). We suspected the alkylthio might be oxidized by bromination reagent: NBS or Br_2, which have failed the reactions. Therefore, we tuned to route 2, which is outlined in **Scheme 3-3**. The replacement of 2-acetyl-thiophene by 2-acetyl-5-bromothiophene allows the avoidance of subsequent bromination reactions, which achieved brominated monomer 4-b successfully.

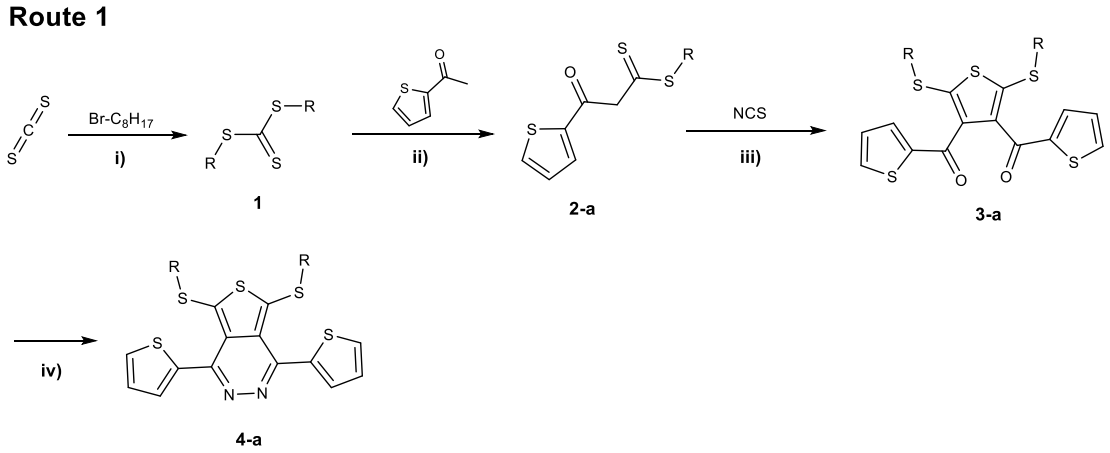

Scheme 3-1 Synthetic route towards non-brominated TPT.

Reaction conditions: i) DMAc/$CsCO_3$/r.t/overnight, 90%; ii) DMF/hexane (1:5)/NaH /r.t/12 h, 30%; iii) DMSO/100 °C/8.5 h, 42%; iv) NH_2-NH_2/100 °C /4 h, 66%.

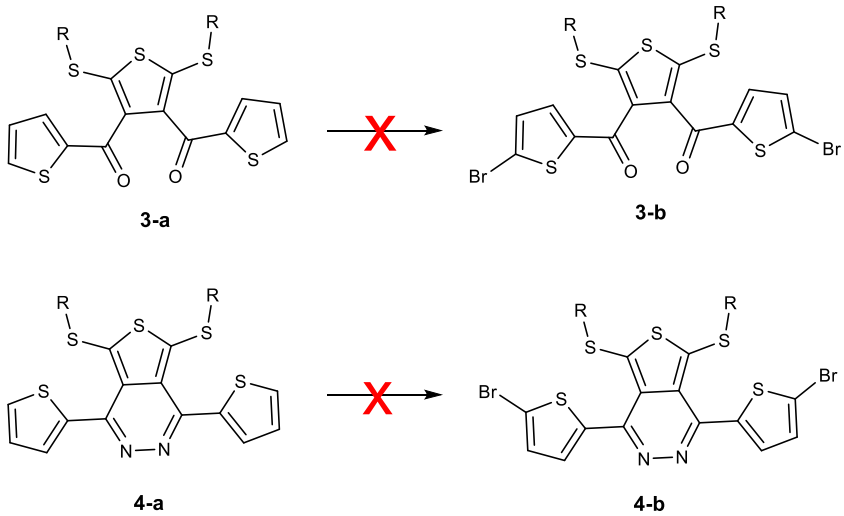

Scheme 3-2 Bromination of 3-a and 4-a.

Reaction conditions: 1. DCM/NBS/r.t; 2. Chloroform/NBS/40-60 °C; 3. DMF/NBS/r.t; 4. DCM/Br_2/r.t

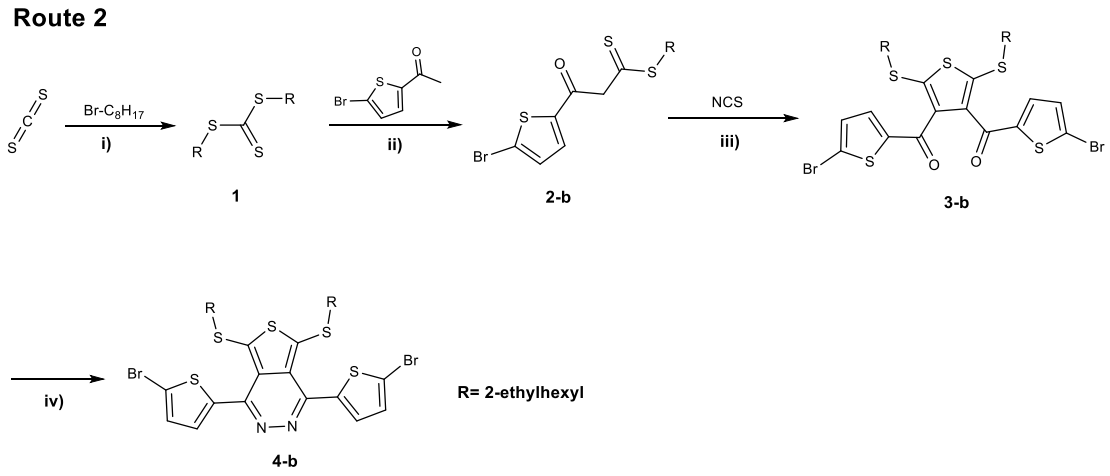

Scheme 3-3 Synthetic route towards brominated TPT.

Reaction conditions: i) DMAc/$CsCO_3$/r.t/overnight, 90%; ii) DMF/hexane (1:5)/NaH/r.t/12 h, 30%; iii) DMSO/100 °C/8.5 h, 42%; iv) NH_2-NH_2/100 °C/4 h, 66%.

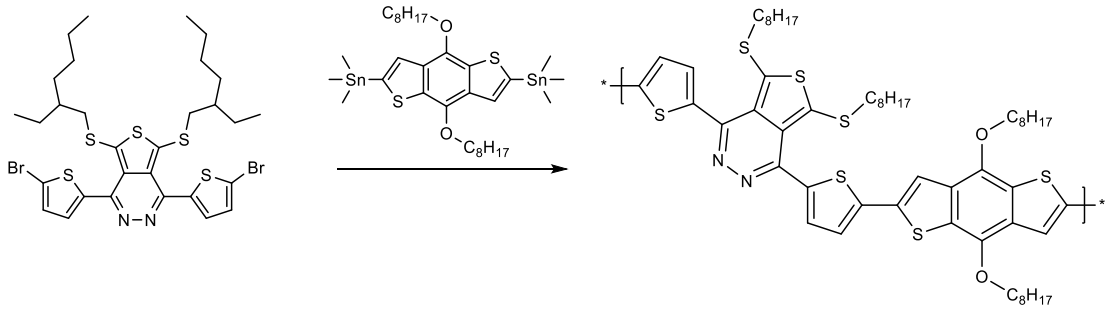

Scheme 3-4 Synthetic route towards TPT-BDT polymer.

Reaction conditions: Toluene/Pd $(PPh_3)_4$/90-110 °C/48 h, 52%.

The brominated TPT (compound 4-b) was then polymerized with comonomer BDT and TT by Stille coupling polymerization reactions. In spite of numerous attempts, only polymer TPT-BDT was obtained with toluene as the solvent and Pd $(PPh_3)_4$ as the catalyst with relatively low yield (52%) (**Scheme 3-4**). The low yield suggested that the polymer had low molecular weight, which could be partially explained by a strong interaction of the pyridazine unit with the palladium catalyst. Indeed, pyridazines have been evidenced as a strong metal-coordinating ligand.[120][121] Thurs, during the polymerization reaction, pyridazine moiety of TPT can trap the palladium catalyst so that the efficiency of polymerization is limited (**Figure 3-3**).

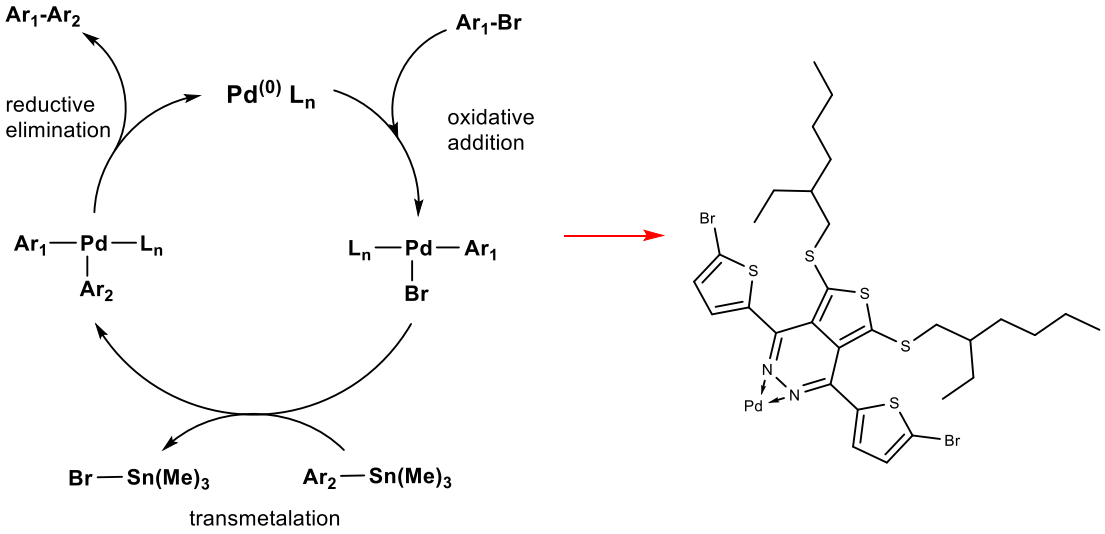

Figure 3-3 The complex of palladium with TPT monomer can occur during the polymerization reaction.

3.3 Characterization of TPT-BDT

TPT-BDT polymer show good solution processability in several common solvent, such as chloroform, chlorobenzene and o-dichlorobenzene. The molecular weight of the TPT-BDT polymer is 10.7 kDa (Mn) with a PDI of 3.1, which was measured by gel permeation chromatography (GPC) using 1,2,4-trichlorobenzene as eluent under 140 °C and monodispersed polystyrene as standard (**Figure 3-4**). The reason of the relatively low molecular weight has been discussed above.

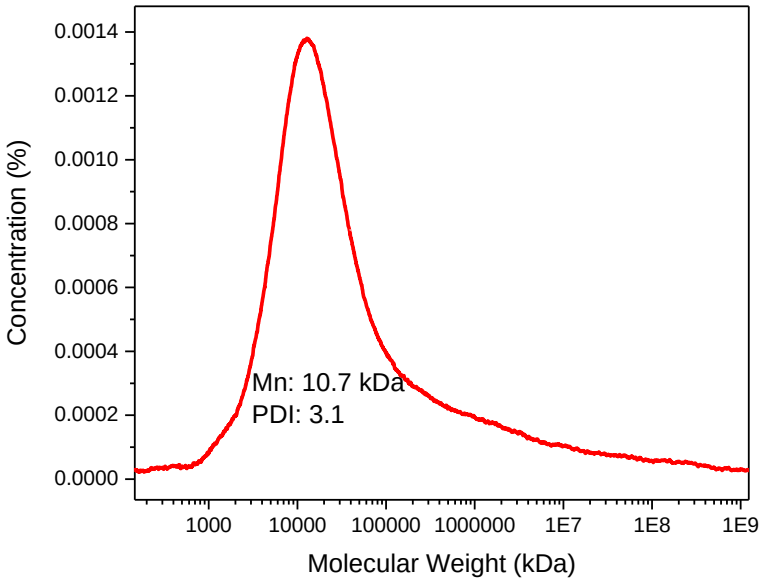

Figure 3-4 The molecular weight distribution for TPT-BDT obtained by HT-GPC.

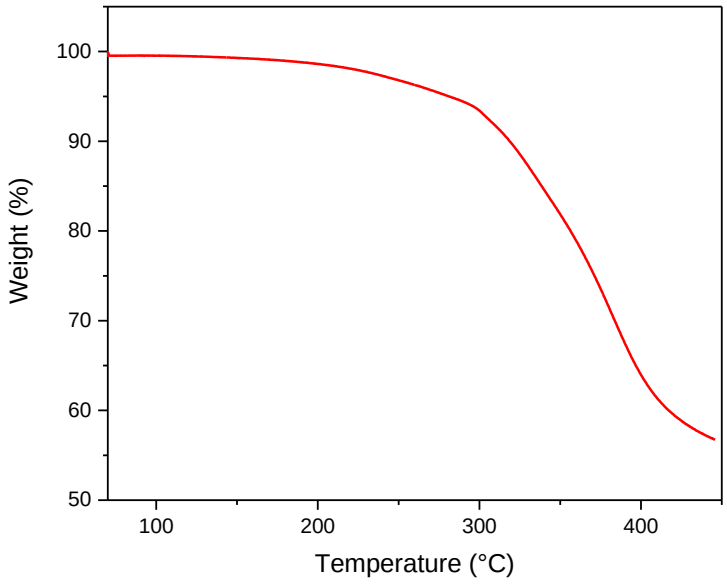

Figure 3-5 TGA curve of TPT-BDT measured with a heating rate of 10 °C min^{-1} under nitrogen.

The TPT-BDT polymer was also characterized by thermogravimetric analyses (TGA). As shown by **Figure 3-5**, TPT-BDT polymer exhibits a good thermal stability up to 300 °C.

The UV-Vis-IR absorption spectra of the polymer TPT-BDT is shown in **Figure 3-6**. There are two absorption peaks can be observed in the absorption spectrum of the film. The peak at 388 nm should be attributed to π–π* transition along the conjugated backbones of the polymer, while the shoulder peak at 503 nm should be attributed to interchain π–π* transition due to the π–π stacking of the backbones.[122] Compared to the solution absorption, both peaks of thin film absorption were red-shifted from 380 nm to 388 nm and 496 nm to 503 nm. The red-shifting suggests TPT-BDT polymer has a more coplanar conformation and stronger intermolecular interactions in the solid state (thin film). The optical bandgap was calculated to be 1.89 eV according to onset absorption of the solid state.

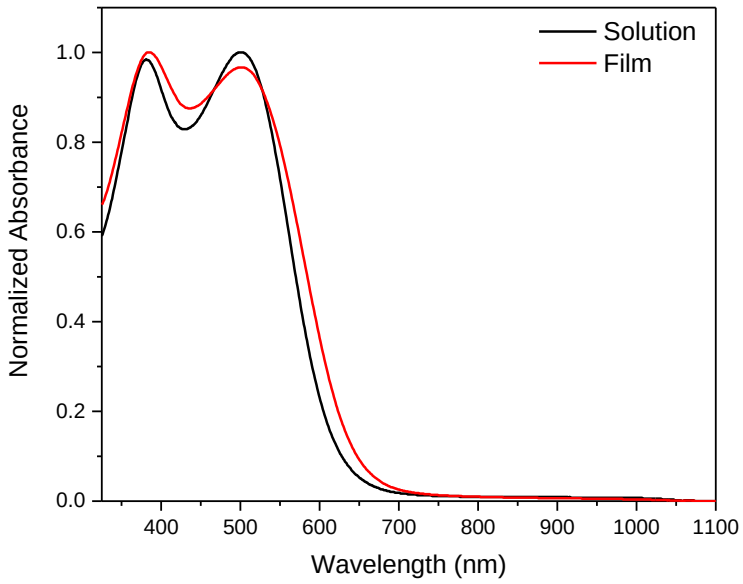

Figure 3-6 The UV-Vis-IR absorption spectra of TPT-BDT in diluted solution (chloroform) and in thin film.

Cyclic voltammetry measurement was used to investigate the HOMO/LUMO levels of the TPT-BDT polymer (**Figure 3-7**). Based on the onset oxidation potentials, the HOMO is

estimated to be -5.55 eV. Due to the absence of reduction peaks, the LUMO was determined by combining HOMO with the optical bandgap, obtaining a LUMO energy level of -3.66 eV. When compared to the analogue backbones with pyrazine rings, such as quinoxaline and thieno-pyrazine based polymers, the TPT-BDT polymer has lower or approximate energy levels (**Figure 3-8**). These results suggest the utilization of pyridazine unit is a good method to modulate the HOMO and LUMO of conjugated polymers.

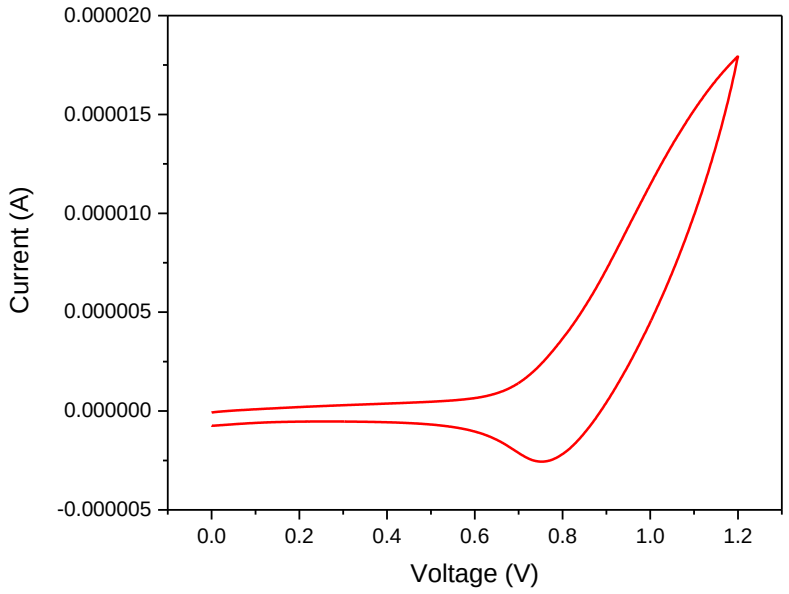

Figure 3-7 Cyclic voltammogram of PzDP16-BDT in a 0.1 M tetrabutylammonium hexafluorophosphate solution in acetonitrile.

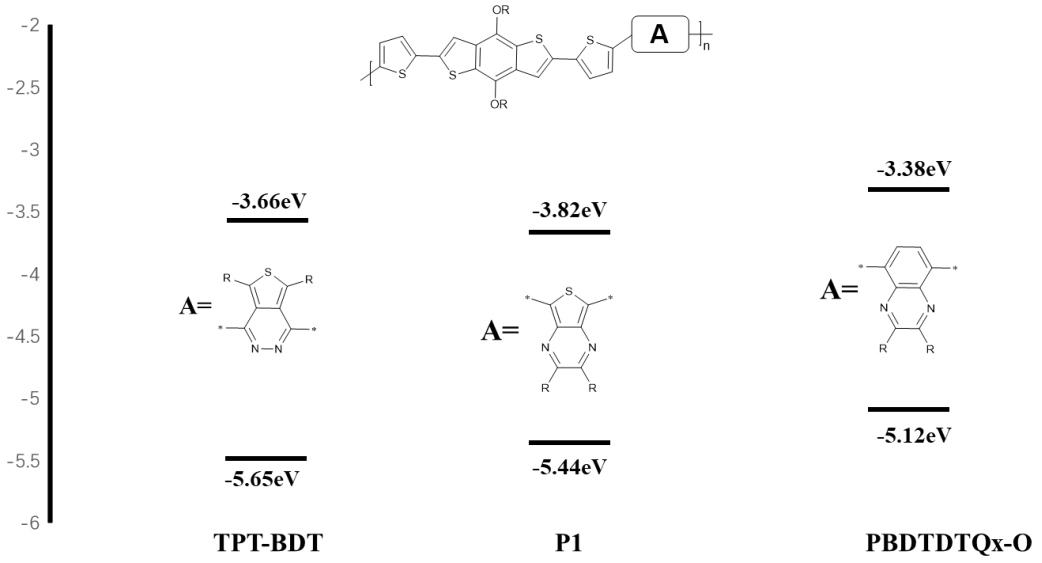

Figure 3-8 The energy levels of TPT-BDT and the polymers with analogue backbones (P1 and PBDTDTQx-O).

The numbers of P1 and PBDTDTQx-O can be found from the reference.[123][124]

Further, The TPT-BDT polymer was characterized as the channel semiconductor in bottom-contact, bottom-gate OTFTs with gold being the drain and source electrodes and p-doped silicon wafer being gate electrode. However, OTFT devices with TPT-BDT thin films showed almost no performance for hole/electron mobilities at different annealed temperature. The computational simulations showed a highly twisted backbone for TPT-BDT polymer, which could limit carrier charge-transport properties. For example, Brédas found that torsion angles along the main chains that larger than about 40 ° have a significant negative effect on the electronic properties.[125] However, the computational simulations showed that the torsion angle between thiophene and thieno-pyridazine core in TPT-Me is as high as 66 ° (**Figure 3-9**). Hence, such a large torsion angle of TPT monomer might prevent charge delocalization over the polymer backbone and co-facial π-π interactions between polymer chains, thereby impairing mobilities.

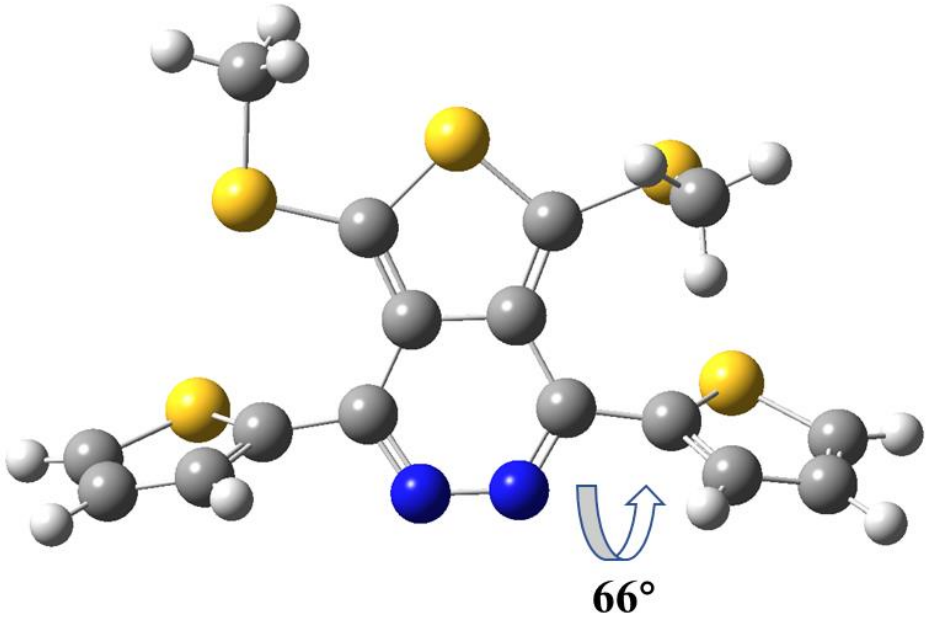

Figure 3-9 The geometry of TPT-Me.

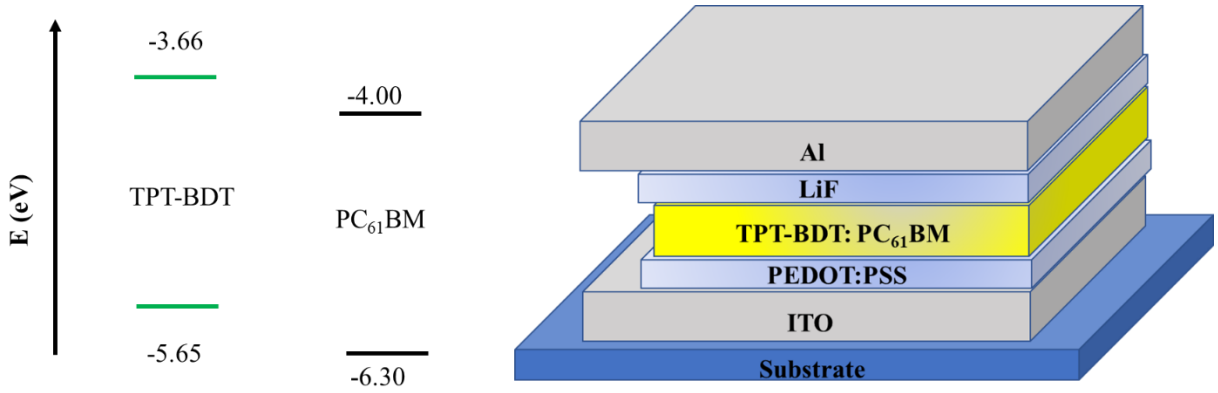

Figure 3-10 The energy level alignment of the TPT-BDT and $PC_{61}BM$**[126]**; b) Schematic representation of the solar cell device structure.

Further, to investigate the photovoltaic properties of TPT-BDT, the PSCs were fabricated with a conventional device architecture of ITO/PEDOT: PSS/TPT-BDT: $PC_{61}BM$/LiF/Al (**Figure 3-10**) and were characterized under the illumination of AM 1.5 G (100 mW cm^{-2}). **Table 3-2, 3-3** and **3-4** displays the photovoltaic performance of the PSC devices with different fabrication

conditions. Firstly, the donor/acceptor (TPT-BDT/$PC_{61}BM$) weight ratios were optimized in the range from 1.5:1, 1:1 to 1:1.5. It can be noticed that all the PSCs devices with different D/A weight ratios exhibited relatively low photovoltaic performance. The optimum D/A weight ratio was found to be 1:1.5, and the corresponding results showed the highest PCE of 0.11% with V_{OC} of 0.66 V, J_{SC} of 0.74 mA cm^{-2}, and FF of 24% (**Figure 3-11**). After that, the optimized D/A ratio (1:1.5) was carried out to study the impact of active layer thickness and thermal annealing on the photovoltaic performance of the PSCs based on TPT-BDT/$PC_{61}BM$. **Table 3-3** showed the relationship between photovoltaic performance of the PSCs with difference active layer thickness. We can see that the photovoltaic performance of the PSCs was not sensitive to the active layer thickness in the range of 70 - 170 nm, where the overall PCEs were nearly unchanged. However, the PCE of the PSCs slightly decreased with the thermal annealing at 100 °C, and 150 °C for 15 min, indicating that the thermal annealing is not required for the PSCs based on TPT-BDT/$PC_{61}BM$.

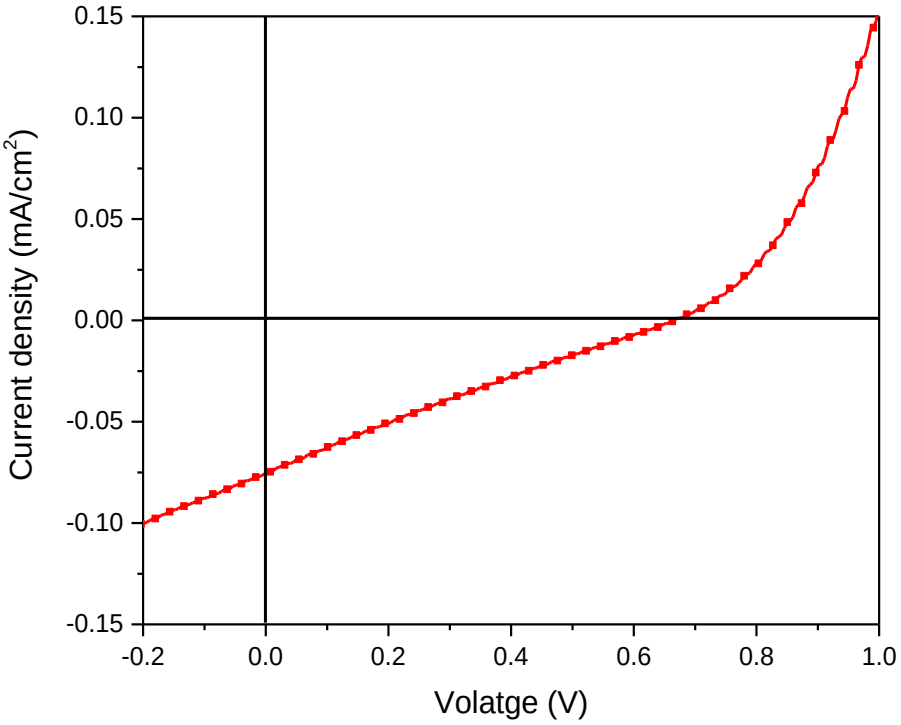

Figure 3-11 The J-V characteristic for the solar cell device based on TPT-BDT: $PC_{61}BM$. The active layer (1:1.5 weight ratio) was spin-coated using a solution (10 mg/ml) in chloroform at 2000 rpm.

Table 3-2 The optimization of donor/acceptor ratio.

Donor/Acceptor ratio	J_{SC} (mA/cm^2)	V_{OC} (V)	FF	PCE (%)
1:1	0.54	0.64	0.24	0.08
1:1.5	0.74	0.66	0.24	0.11
1.5:1	0.31	0.68	0.25	0.05

Table 3-3 The optimization of active layer thickness.

Thickness (nm)	Donor/Acceptor ratio	J_{SC} (mA/cm^2)	V_{OC} (V)	FF	PCE (%)
70	1:1.5	0.70	0.60	0.25	0.11
113	1:1.5	0.74	0.66	0.24	0.11
170	1:1.5	0.66	0.66	0.24	0.11

Table 3-4 Device performance optimization through post-treatment.

Thermal annealing (°C)	Donor/Acceptor ratio	J_{SC} (mA/cm^2)	V_{OC} (V)	FF	PCE (%)
None	1:1.5	0.74	0.66	0.24	0.11
100	1:1.5	0.55	0.67	0.24	0.09
150	1:1.5	0.68	0.65	0.24	0.10

The poor performance of TPT-BDT/$PC_{61}BM$ might be mainly caused by the relatively low molecular weight of TPT-BDT polymer. The study of the impact of polymer molecular weight

on performance of OPV has been previous reported in literature. For example, Pavel have demonstrated that lowering the molecular weight of P3HTs can dramatically decrease the performance of P3HT/PCBM bulk heterojunction solar cells. Compared to the devices made of high-molecular-weight P3HT, the devices with low molecular weight P3HT exhibited a reduction of the V_{OC} and FF by 50% as well as a decrease in the J_{SC} by a factor of 5 - 10.[127] Similarly, Ding also found that the increase of Mn of PTB7-Th could improve the performance of PTB7-Th/$PC_{61}BM$ based cells due to better morphology and lower density of recombination centers.[128] Hence, to further improve the performance of solar cell based on TPT-based polymer, the foremost focus should be placed on the polymerization optimization to obtain high molecular weight polymers.

3.4 Conclusion

In summary, we have presented the synthesis of new pyridazine-based conjugated monomer TPT for the first time. The electron-withdrawing monomer TPT has been prepared conveniently in a few steps involving condensation reaction and simple purification procedures. The related polymer TPT-BDT suggests that introducing pyridazine unit can efficiently modulate HOMO/LUMO compared with the analogue backbones with pyridine. However, DFT simulation showed a highly twisted backbone for TPT structure, which might be the reason of the poor charge carrier charge-transport properties in OTFT application. When the polymer TPT-BDT was applied as donor in PSCs with $PC_{61}BM$ as acceptor, all devices showed very poor performance (~ 0.11%). The low PCEs might be caused by the relatively low molecular weight, because the pyridazine unit has a strong interaction with palladium catalyst during polymerization reaction and thus limits the efficiency of the polymerization reaction.

3.5 Experimental

3.5.1 Materials and Characterization

All chemicals were purchased from Sigma-Aldrich and used without further purification. The DFT calculation, GPC measurement, TGA measurement, UV-Vis-IR absorption spectra, cyclic voltammetry (CV) and NMR data were obtained with the same conditions as that

described in Chapter 2.

3.5.2 Fabrication and Characterization of OTFT and Solar Cell Devices

The device fabrication procedures used for testing TPT-BDT copolymer were same as that described in Chapter 2 for PzDP-based polymers.

3.5.3 Synthetic Procedures

General procedure for the synthesis of bis(2-ethylhexyl) carbonotrithioate (Compound 1):

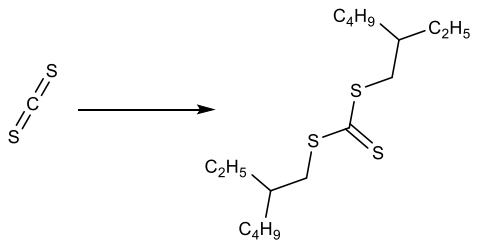

A mixture of CS_2 (1.52 g, 20.0 mmol) and Cs_2CO_3 (6.52 g, 20.0 mmol) in DMAc (20 ml) was stirred at r.t for 30 min, and then 2-ethylhexyl bromine (3.86 g, 20.0 mmol) in DMAc (5 ml) was added. Stirring of the reaction mixture was continued at 25 °C overnight hours. Then 40 ml water was added to the mixture. The product was extracted by 25 ml × 3 ethyl acetate, and then dried by vacuo. The crude product was filtered by a thin silica gel layer to get a light-yellow oil.

Yield: 3.0 g, 90%.

^{1}H NMR (300 MHz, chloroform-d, ppm) δ 3.38 (d, J = 7.9 Hz, 4H), 1.79 - 1.59 (m, 2H), 1.49 - 1.18 (m, 16H), 0.87 (m, 12H).

General procedure for the synthesis of 2-ethylhexyl 3-(5-bromothiophen-2-yl)-3-oxopropanedithioate (Compound 2-b):

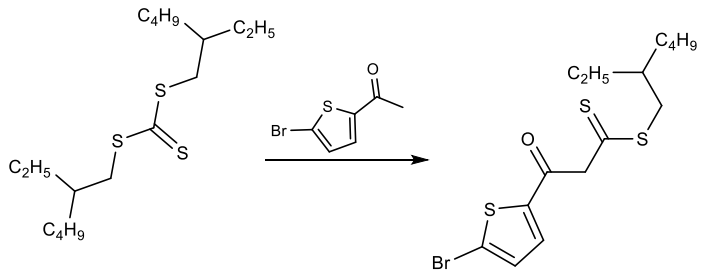

2-Acetyl-5-bromo-thiophene (2.05 g, 10 mmol) was added to a suspension of NaH (60% suspension in mineral oil, 0.6 g, 15 mmol) in DMF/hexane solvent mixture (1:4, 30 ml). After 1 hour, di(2-ethylhexyl) trithiocarbonate (3.34 g, 10 mmol) was slowly added to the reaction mixture and stirred well for 12 h. After completion of the reaction (monitored by TLC), the reaction mixture was acidified with 1M HCl (20 ml). The product was extracted with dichloromethane (2 × 30 ml) followed by washing with brine (2 × 25 ml) and dried over anhydrous sodium sulfate. The solvent was evaporated under vacuum and the residue obtained was purified by column chromatography over a very short silica gel using hexane/DCM (5:1) as eluent to give a yellow oil without further purify.

Yield: 1.3 g, 30%.

^{1}H NMR (300 MHz, chloroform-d, ppm) δ 7.45 (s, 1H), 7.08 (t, J = 4.2 Hz, 1H), 6.69 (s, 1H), 3.25 (d, J = 6.3 Hz, 2H), 1.69 (h, J = 6.3 Hz, 1H), 1.51 - 1.13 (m, 12H), 0.88 (s, 12H).

General procedure for the synthesis of (2,5-bis((2-ethylhexyl)thio)thiophene-3,4-diyl)bis((5-bromothiophen-2-yl)methanone) (Compound 3-b):

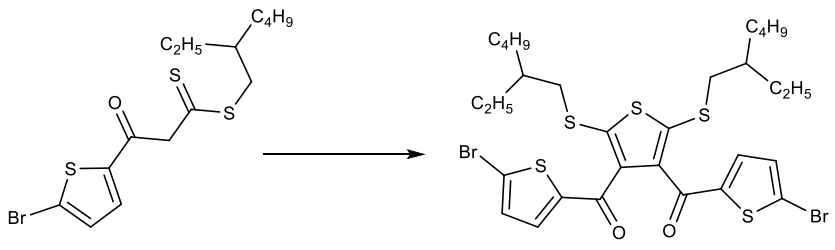

To a stirring solution of 2-ethylhexyl 3-(5-bromothiophen-2-yl)-3-oxopropanedithioate in DMSO (8 ml), NCS (0.17 g, 1.3 mmol, 0.5 eq) was added at room temperature and the reaction mixture was stirred for 30min. The flask containing the reaction was transferred to an oil bath at 100 °C for 12 h. After completion of the reaction (monitored by TLC), water was added. The content was extracted with dichloromethane (2 × 10 ml). The combined extract was dried over anhydrous Na_2SO_4 and the solvent was evaporated under vacuum. The crude residue thus obtained was purified by column chromatography over silica gel using DCM/hexane as eluent to afford an orange oil.

Yield: 0.42 g, 43%.

^{1}H NMR (300 MHz, chloroform-d, ppm) δ 7.12 (d, J = 4.1 Hz, 2H), 6.99 (d, J = 4.1 Hz, 2H), 2.94 (d, J = 6.2 Hz, 4H), 1.47 - 1.11 (m, 20H), 0.96 - 0.77 (m, 12H).

General procedure for the synthesis of 1,4-bis(5-bromothiophen-2-yl)-5,7-bis((2-ethylhexyl)thio)thieno[3,4-d]pyridazine (Compound 4-b):

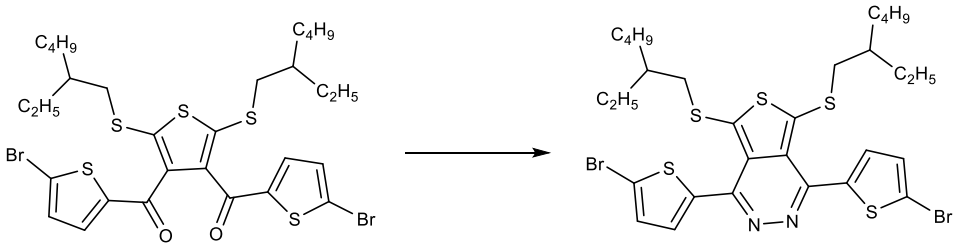

To the solution of the 3,4-diacylthiphene (0.5 g, 0.66 mmol) in acetic acid (12 ml) was added hydrazine monohydrate 3 ml, and the resulting mixture at 100 ℃ 4 h under nitrogen. After cooling down to r.t, acetic acid was quenched by $NaHCO_3$ solution. 50 ml DCM was added to the crude product and washed by water (50 ml × 3). The organic layer was dried by Na_2SO_4 and concentrated. Then the product was purified by through a silica gel column with the eluent (hexane/EA = 5:1) to give a dark red viscous oil.

Yield: 0.33 g, 66%.

^{1}H NMR (300 MHz, chloroform-d, ppm) δ 7.29 (d, J = 3.9 Hz, 2H), 7.11 (d, J = 3.9 Hz, 2H), 2.76 (d, J = 6.2 Hz, 4H), 1.42 (s, 2H), 1.39 - 1.03 (m, 20H), 0.97 - 0.72 (m, 13H).

General procedure for the synthesis of TPT-BDT:

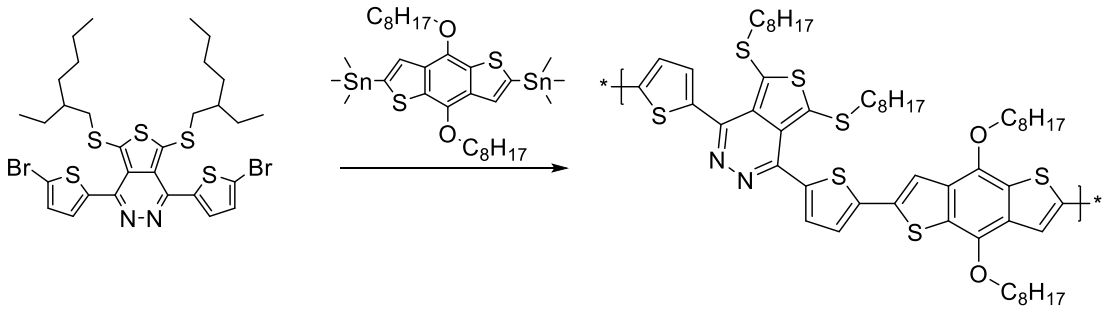

Compound 4-b (0.100 g, 133.9 μmol) and benzol-bithiophene (0.103 g, 133.9 μmol) were charged into a 25 ml flask. After degassing and refilling argon for 3 times, anhydrous toluene (6 ml) and Pd $(PPh_3)_4$ (5.5%, 8.5 mg,7.35 μmol) in 1 ml toluene were added and the reaction mixture was raised to 110 ℃ and stirred for 48 hours. After the mixture cold down, the mixture was poured into 100 ml methanol with stirring and filtered. Soxhlet extraction by acetone, hexane and chloroform.

Yield:

Acetone extracted fraction: 15 mg, 14%.

Hexane extracted fraction: 30 mg, 30%.

Chloroform extracted fraction: 54 mg, 52%.

Chapter 4 Summary and Future work

In conclusion, this thesis presents the design and synthesis of two electron-deficient moieties PzDP and TPT by utilizing electron-withdrawing nitrogen atoms, and the characterization of several related polymers semiconductor were described.

In Chapter 2, a series of alkyl-substituted PzDP monomers were prepared and incorporated into D-A copolymers. Two PzDP-based polymers, PzDP24-T and PzDP16-BDT, were synthesized and demonstrated suitable solubility and HOMO/LUMO levels. In addition, PzDP24-T showed n-type dominant charge transport properties in OTFTs with electron mobility up to 2.9×10^{-2} cm^2 V^{-1} $s^{-1}cm^2$ V^{-1} s^{-1}, whereas PzDP16-BDT exhibited ambipolar charge transport behavior with balanced electron/hole mobilities up to 2.2×10^{-3} cm^2 V^{-1} s^{-1}/ 2.5×10^{-3} cm^2 V^{-1} s^{-1}. When the polymers were used as acceptor in all-PSCs with PTB7-Th as donor, the PzDP24-T based devices showed very poor performance (the highest PCE 0.3%). AFM images of PTB7-Th: PzDP24-T indicated a large phase-separated fabric structure with a large RMS roughness, which is unfavorable for charge generation that happens at the D-A interface. The poor morphology might result from the limited solubility of PzDP24-T polymer, leading to an insufficient D/A intermixing. For PTB7-Th: PzDP16-BDT blend, the morphology was significantly improved with smaller domain size and smoother roughness. Meanwhile, an improvement of PCE as high as 1.57% was realized for PzDP16-BDT based devices. Moreover, XRD measurement suggested both PzDP24-T and PzDP16-BDT films are rather disordered in solid state, which has negative impact on charge-transport. Further, SCLC measurement of the blends exhibited unbalanced charge unbalanced charge due to low electron mobilities, which could partially limited FF.

For future work on the PzDP-based materials should focus on reducing the domain sizes of phase separation, such as using cosolvents and processing additives (DIO). Second, optimizing the backbone structure by introducing higher planar donor, such as thiophene-vinylene-thiophene, could increase the crystallinity for better charge transport, which is favorable to increase both short-circuit current density (J_{SC}) and fill factor (FF).[105] On the other hand, the length of side chains also needs to be tuned to obtain a well balance between crystallinity

and solubility.

In Chapter 3, the novel pyridazine-based conjugated monomer TPT and related polymer TPT-BDT are presented, which is the first time to synthesis and incorporate into D-A copolymer for the structure. The electron-withdrawing monomer TPT have been prepared in good yields and in a few steps involving condensation reaction and simple purification procedures. However, due to the strong interaction of the pyridazine unit with the palladium catalyst during polymerization reaction, the molecular weight of TPT-BDT polymer was relatively low. Compared to the polymers with the analogue backbones, the use of a pyridazine core instead of or pyridine core, is a good way to modulate the HOMO, LUMO of conjugated polymers. TPT-BDT has a highly twisted backbone with torsion angles as high as 66 °, which leaded to the poor charge carrier charge-transport properties in OTFT application. When the polymer was incorporated as a donor in solar cell with $PC_{61}BM$ as acceptor, all devices showed very poor performance around 0.11%. The low molecular weight is expected to be the main reason for these unfavorable PCEs.

For future direction on the TPT-based materials, the work should be concentrated on the polymerization methods to get high molecular weight polymers. Using new palladium catalyst with strong ligand might prevent the pyridazine core from trapping palladium metal, leading to higher efficiency for polymerization reaction. Besides, incorporating the precursor (3-b) of TPT monomer into polymerization before condensation reaction with hydrazine monohydrate could obtain high molecular weight polymers.

Appendix

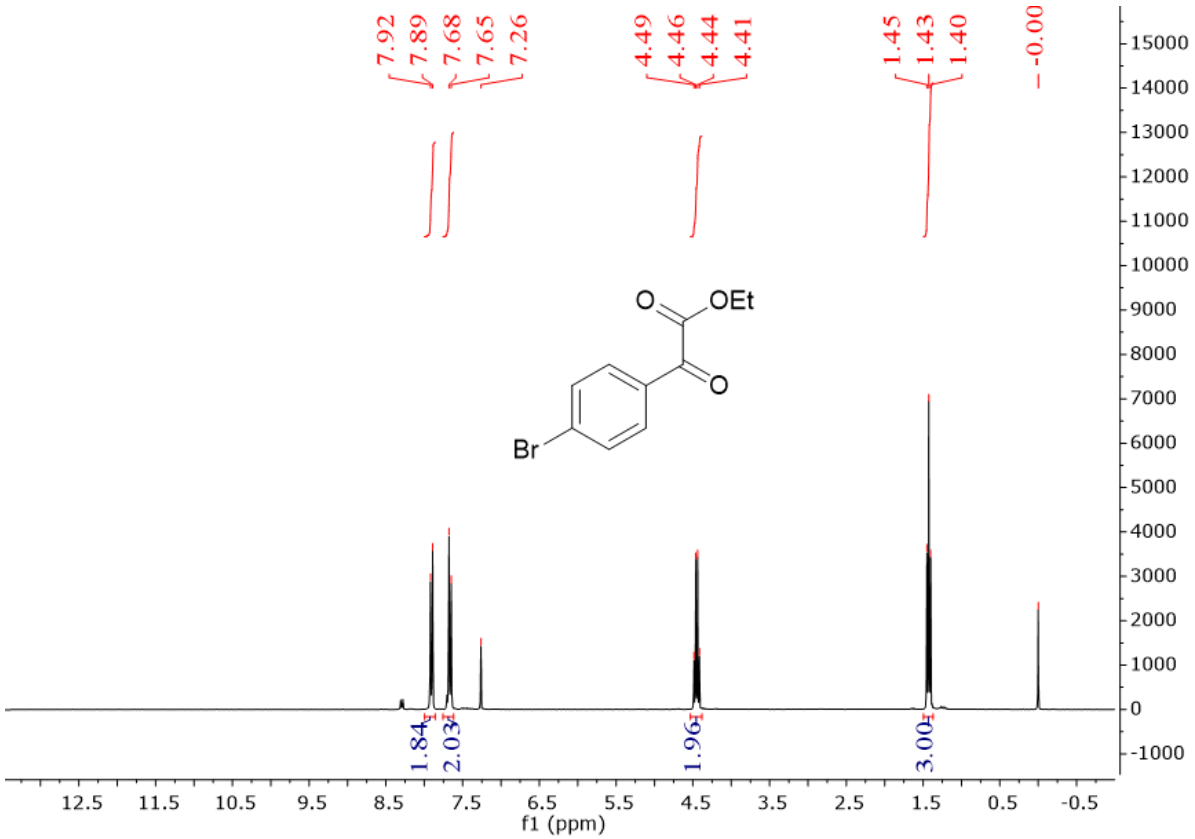

Figure A-1 300 MHz ^{1}H NMR spectrum for ethyl 2-(4-bromophenyl)-2-oxoacetate (Compound 1).

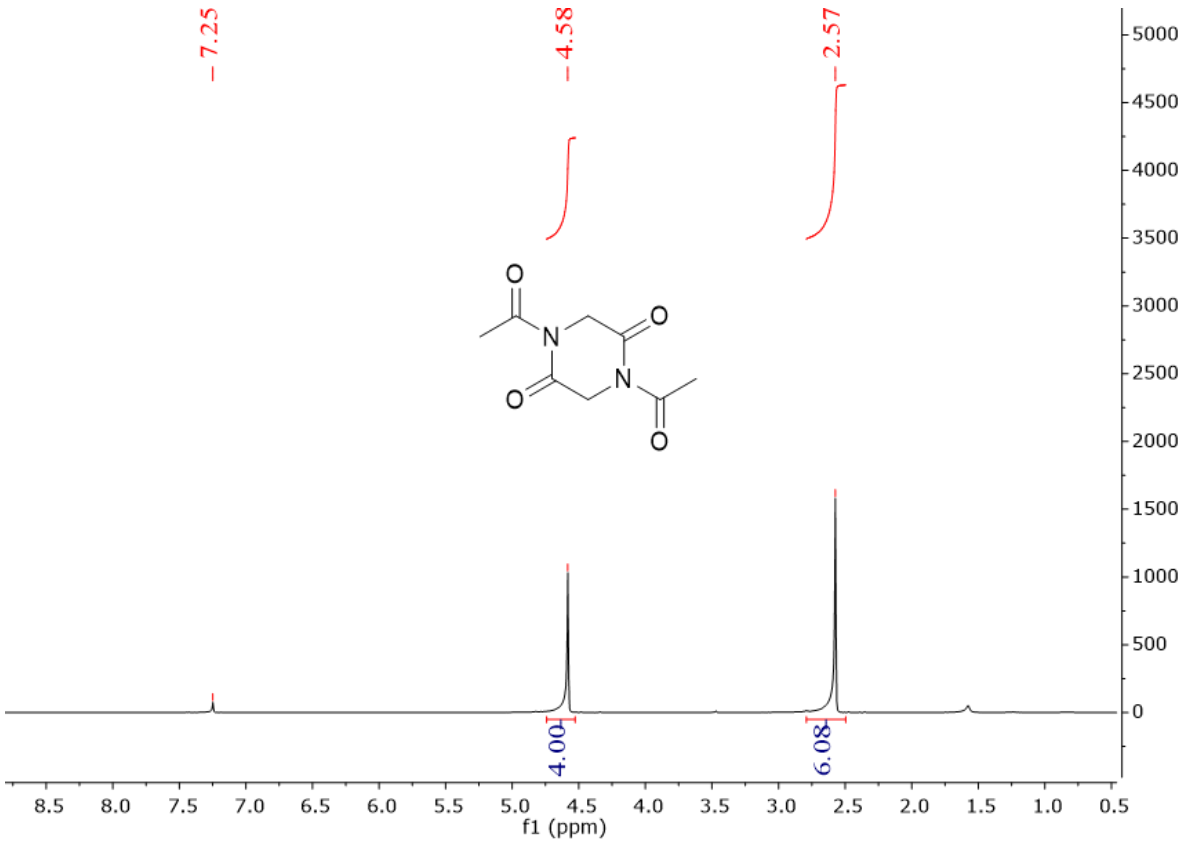

Figure A-2 300 MHz ^{1}H NMR spectrum for 1,4-diacetylpiperazine-2,5-dione (Compound 2).

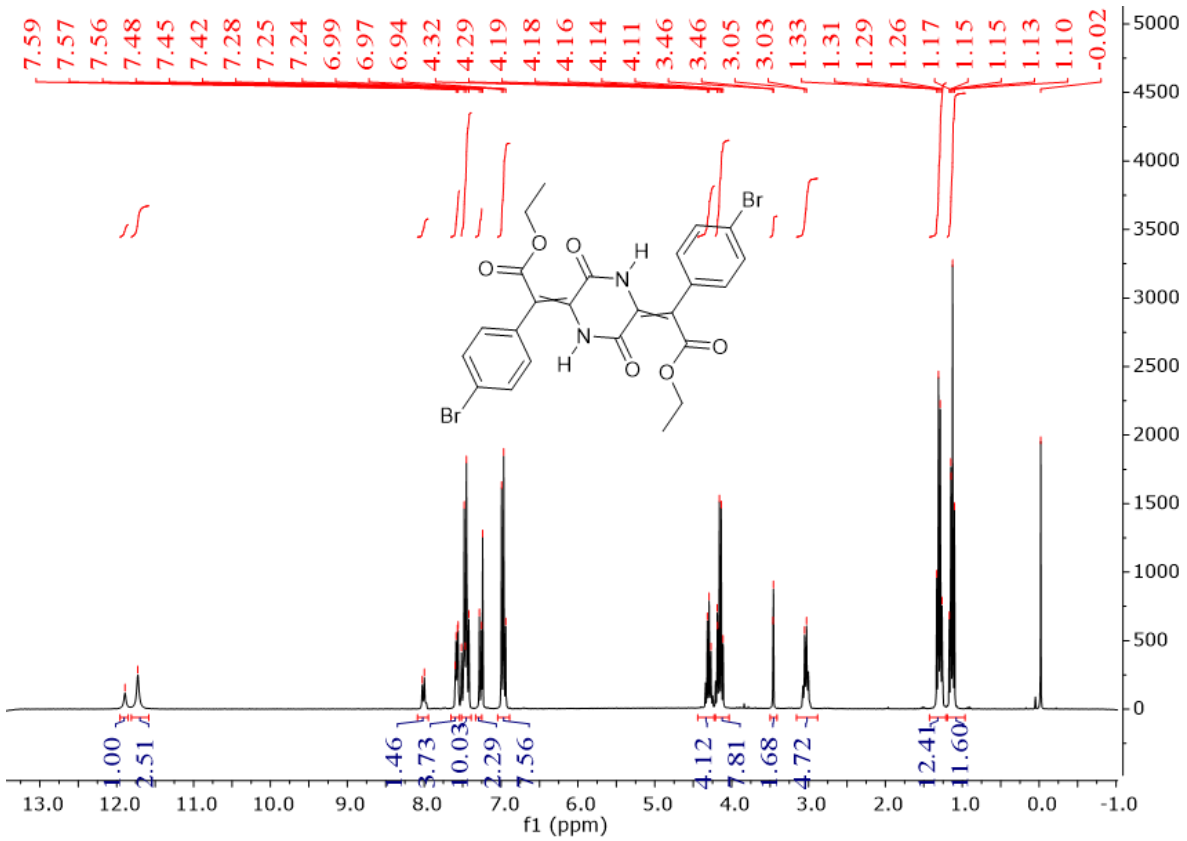

Figure A-3 300 MHz ^{1}H NMR spectrum for diethyl 2,2'-(3,6-dioxopiperazine-2,5-diylidene) bis(2-(4-bromophenyl) acetate)) (Compound 3).

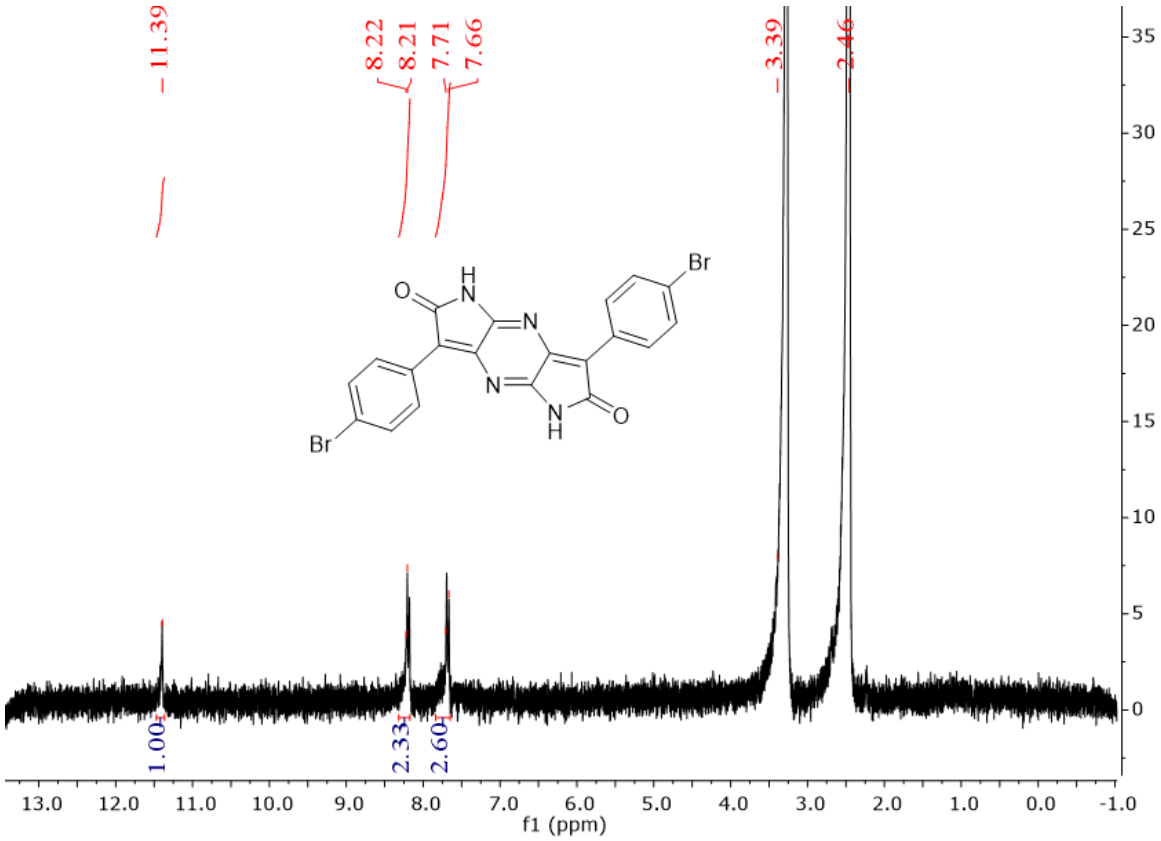

Figure A-4 300 MHz ^{1}H NMR spectrum for 3,7-Bis(4-bromophenyl)dipyrrolo[2,3-b:2',3'-e]pyrazine-2,6 (1H,5H)-dione) (Compound 4).

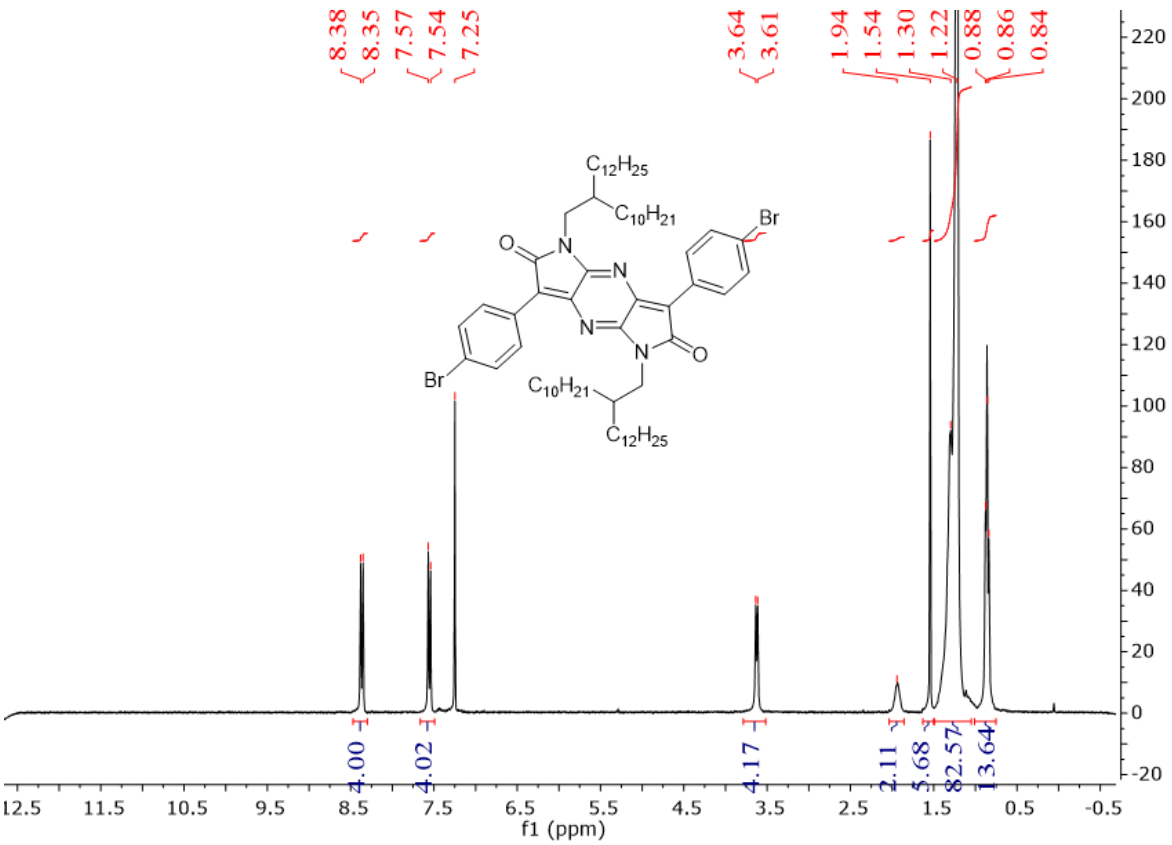

Figure A-5 300 MHz ^{1}H NMR spectrum for 3,7-bis(4-bromophenyl)-1,5-bis(2-decyltetradecyl)dipyrrolo[2,3-b:2',3'-e]pyrazine-2,6(1H,5H)-dione (Compound 5-a).

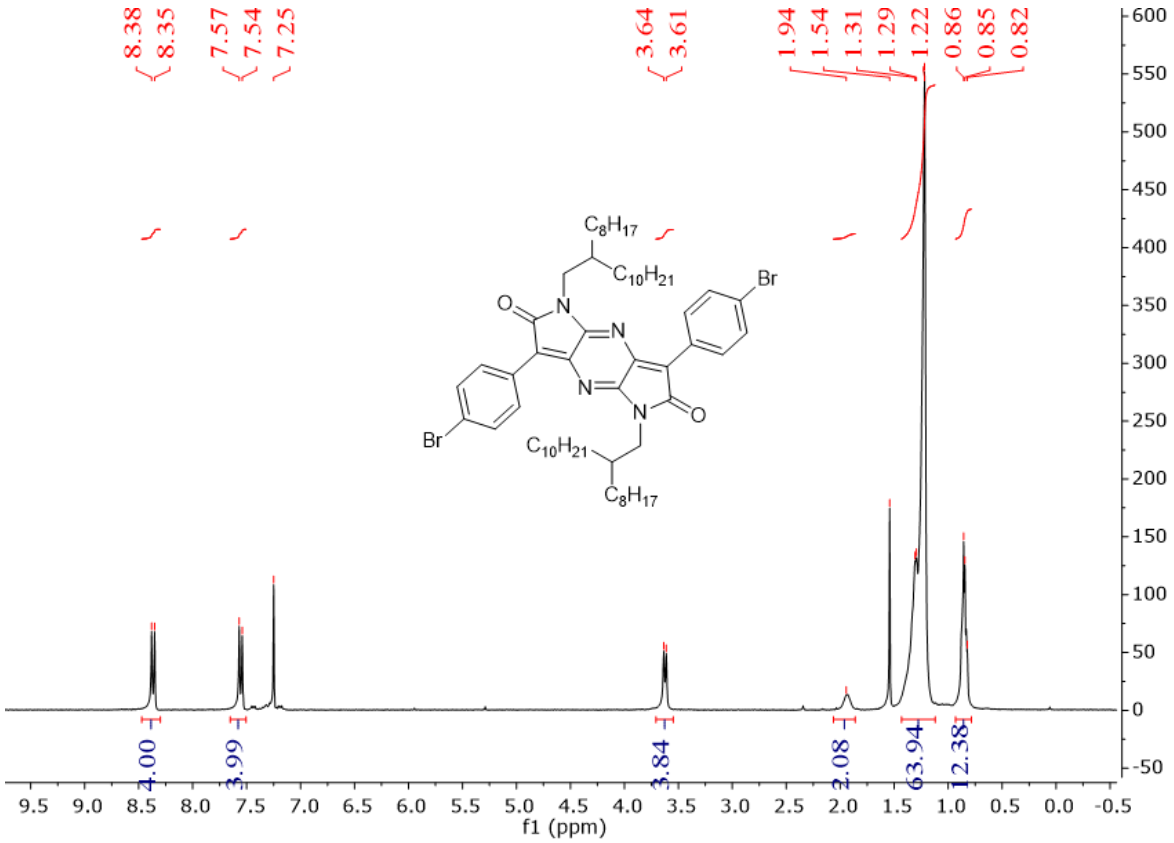

Figure A-6 300 MHz ^{1}H NMR spectrum for 3,7-bis(4-bromophenyl)-1,5-bis(2-octyldodecyl)dipyrrolo[2,3-b:2',3'-e]pyrazine-2,6(1H,5H)-dione (Compound 5-b).

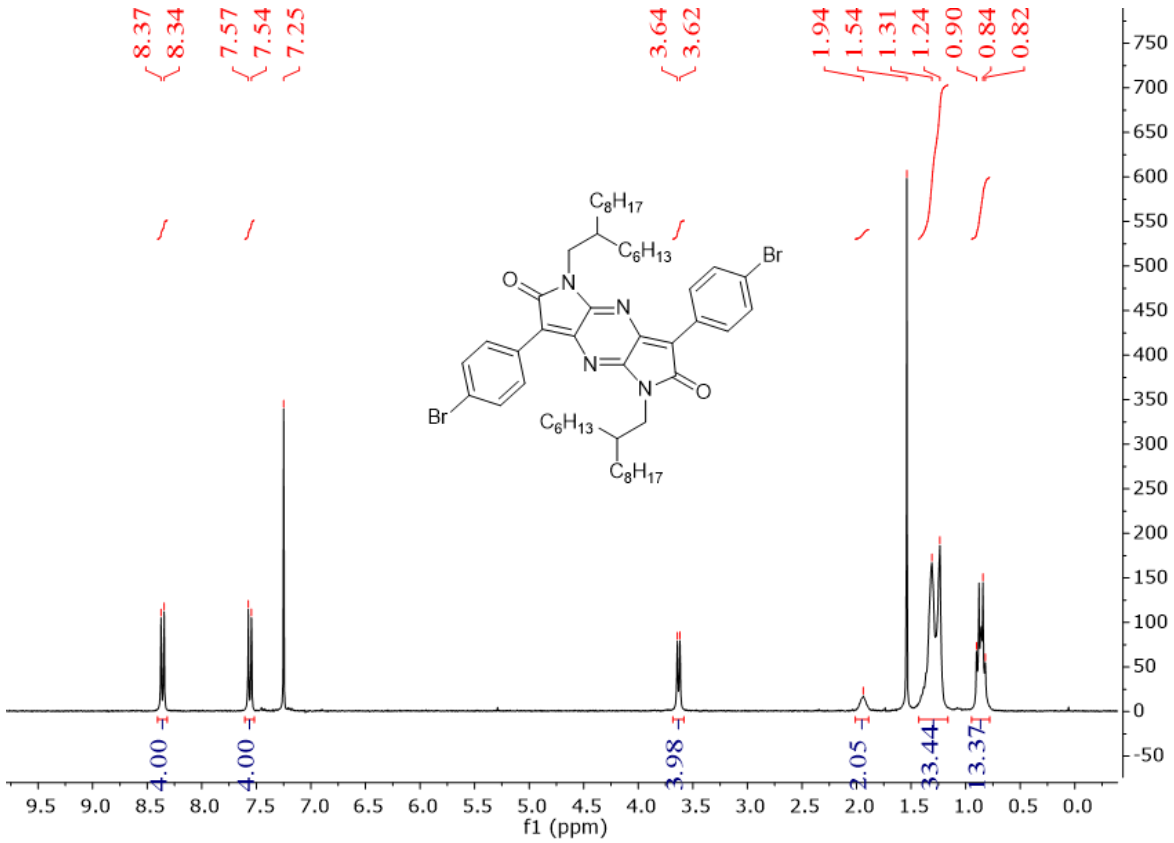

Figure A-7 300 MHz ^{1}H NMR spectrum for 3,7-bis(4-bromophenyl)-1,5-bis(2-hexyldecyl) dipyrrolo[2,3-b:2',3'-e] pyrazine-2,6(1H,5H)-dione (Compound 5-c).

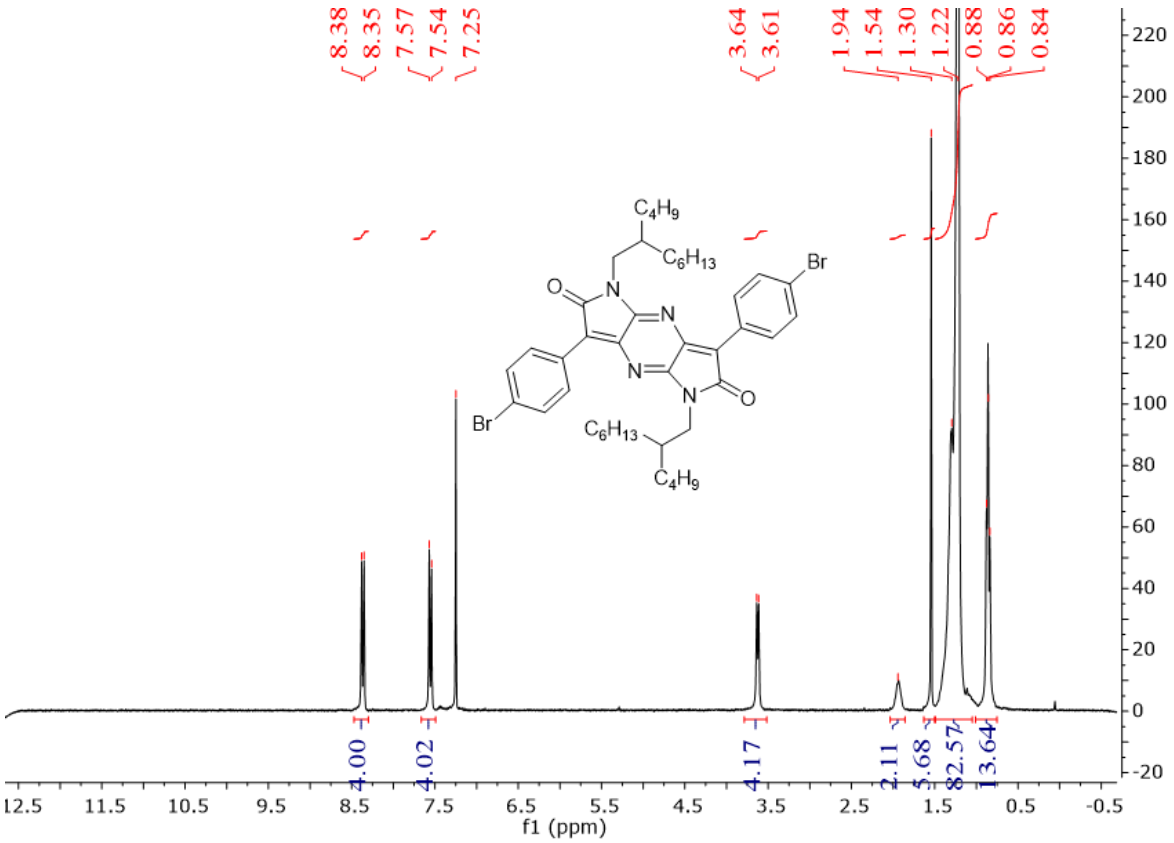

Figure A-8 300 MHz ^{1}H NMR spectrum for 3,7-bis(4-bromophenyl)-1,5-bis(2-butyloctyl) dipyrrolo[2,3-b:2',3'-e] pyrazine-2,6(1H,5H)-dione (Compound 5-d).

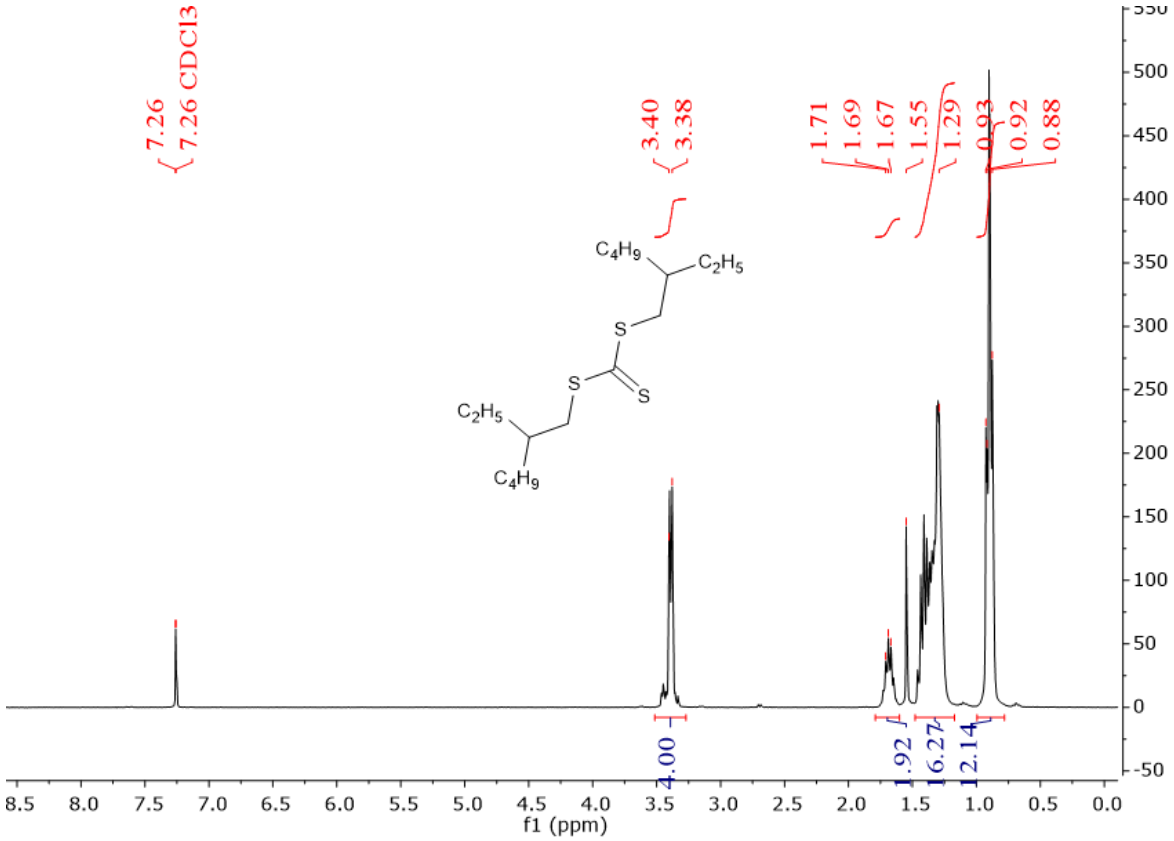

Figure A-9 300 MHz ^{1}H NMR spectrum for bis(2-ethylhexyl) carbonotrithioate (Compound 1).

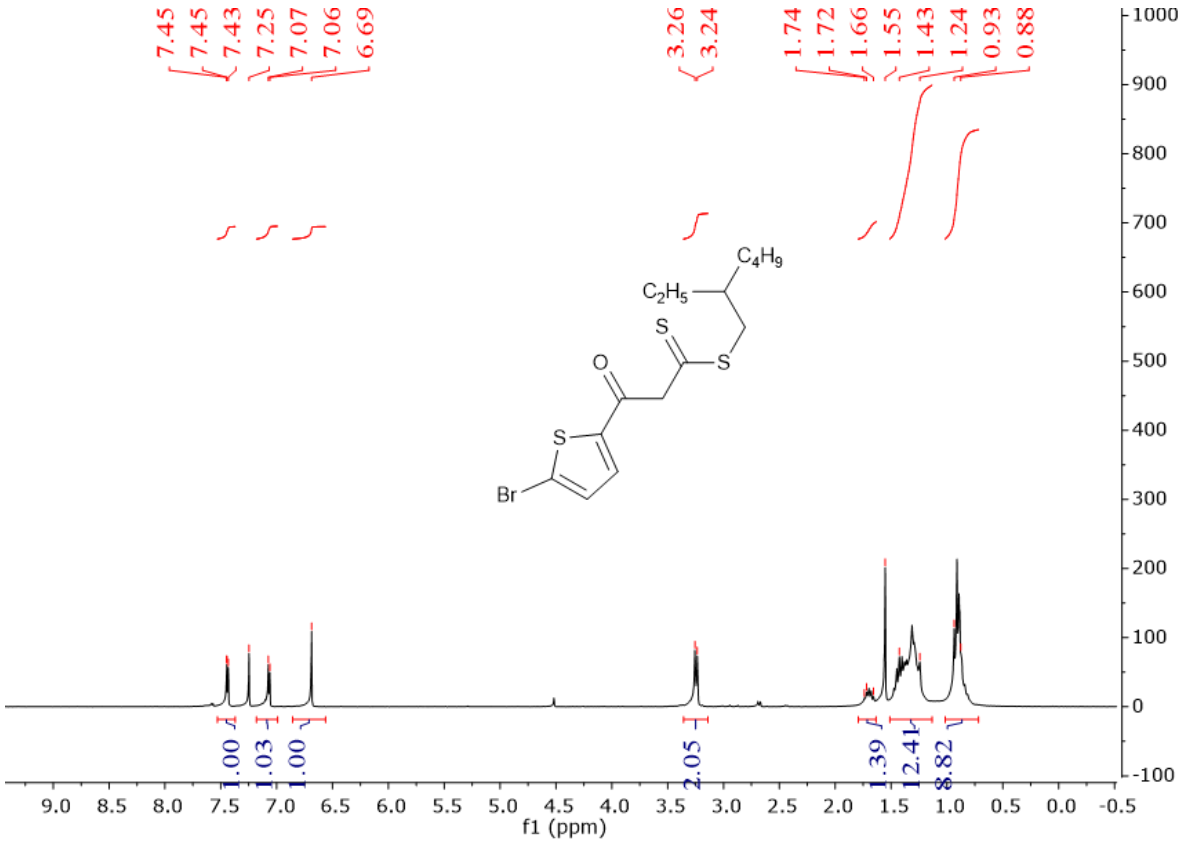

Figure A-10 300 MHz ^{1}H NMR spectrum for 2-ethylhexyl 3-(5-bromothiophen-2-yl)-3-oxopropanedithioate (Compound 2-b).

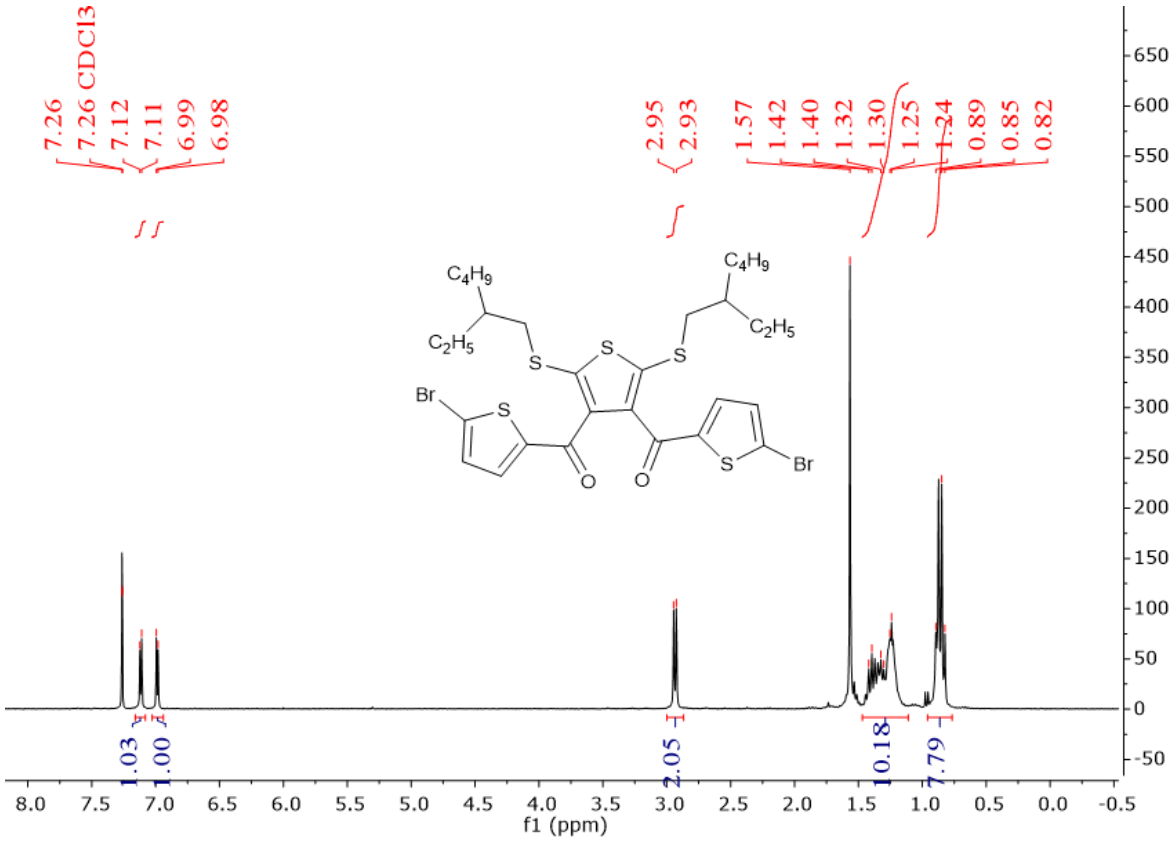

Figure A-11 300 MHz ^{1}H NMR spectrum for 2,5-bis((2-ethylhexyl)thio)thiophene-3,4-diyl)bis((5-bromothiophen-2-yl)methanone) (Compound 3-b).

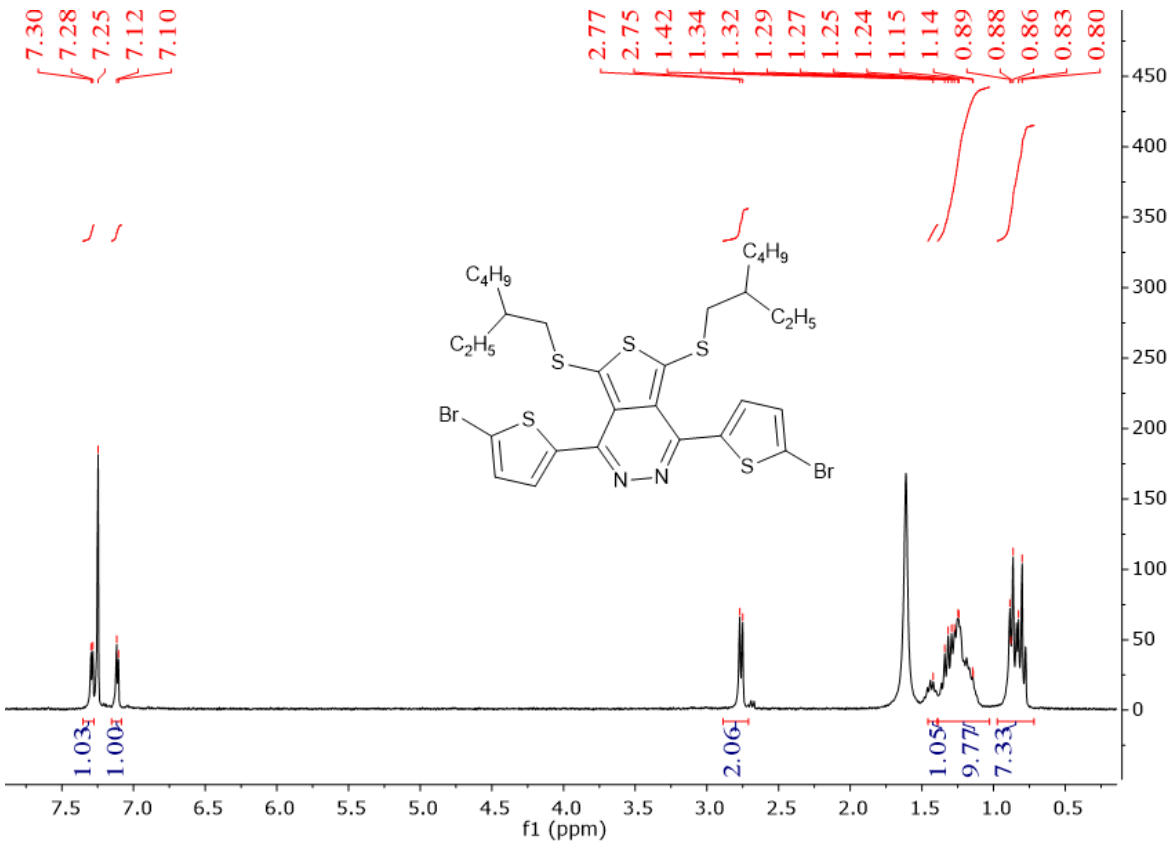

Figure A-12 300 MHz ^{1}H NMR spectrum for 1,4-bis(5-bromothiophen-2-yl)-5,7-bis((2-ethylhexyl)thio)thieno[3,4-d]pyridazine (Compound 4-b).

Bibliography

[1] "Extreme Fossil Fuels," *Oil Change International*.

[2] "Drought under global warming: a review - Dai - 2011 - Wiley Interdisciplinary Reviews: Climate Change - Wiley Online Library."

[3] N. Armaroli and V. Balzani, "The Future of Energy Supply: Challenges and Opportunities," *Angewandte Chemie International Edition*, vol. 46, no. 1–2, pp. 52–66, Jan. 2007.

[4] "Climate Change & Solar Energy | LetsGoSolar.com," *Lets Go Solar*. .

[5] B. Parida, S. Iniyan, and R. Goic, "A review of solar photovoltaic technologies," *Renewable and Sustainable Energy Reviews*, vol. 15, no. 3, pp. 1625–1636, Apr. 2011.

[6] "Photovoltaic Dreaming 1875--1905: First Attempts At Commercializing PV," *CleanTechnica*, 31-Dec-2014.

[7] M. Askari, V. Mirzaei Mahmoud Abadi, and M. Mirhabibi, "Types of Solar Cells and Application," *American Journal of Optics and Photonics*, vol. 3, p. 2015, Aug. 2015.

[8] M. A. Green, "Crystalline and thin-film silicon solar cells: state of the art and future potential," *Solar Energy*, vol. 74, no. 3, pp. 181–192, Mar. 2003.

[9] Masuko, K., M. Shigematsu, T. Hashiguchi, D. Fujishima, M. Kai, N. Yoshimura, T. Yamaguchi, "Achievement of More Than 25 #x0025; Conversion Efficiency With Crystalline Silicon Heterojunction Solar Cell," *IEEE Journal of Photovoltaics*, vol. 4, no. 6, pp. 1433–1435, Nov. 2014.

[10] R. M. Swanson, "A vision for crystalline silicon photovoltaics," *Progress in Photovoltaics: Research and Applications*, vol. 14, no. 5, pp. 443–453.

[11] A. G. Aberle, "Thin-film solar cells," *Thin Solid Films*, vol. 517, no. 17, pp. 4706–4710, Jul. 2009.

[12] M. A. Green, K. Emery, Y. Hishikawa, W. Warta, and E. D. Dunlop, "Solar cell efficiency tables (version 39)," *Progress in Photovoltaics: Research and Applications*, vol. 20, no. 1, pp. 12–20.

[13] J. Yan and B. R. Saunders, "Third-generation solar cells: a review and comparison of polymer:fullerene, hybrid polymer and perovskite solar cells," *RSC Advances*, vol. 4, no. 82, pp. 43286–43314, 2014.

[14] H. Hoppe and N. S. Sariciftci, "Organic solar cells: An overview," *Journal of Materials Research*, vol. 19, no. 7, pp. 1924–1945, Jul. 2004.

[15] Liu, Yongsheng, Xiangjian Wan, Fei Wang, Jiaoyan Zhou, Guankui Long, Jianguo Tian, Jingbi You, Yang Yang, and Yongsheng Chen. n.d, "Spin-Coated Small Molecules for High Performance Solar Cells," *Advanced Energy Materials*, vol. 1, no. 5, pp. 771–775.

[16] M. Hiramoto and Y. Shinmura, “Organic Solar Cells,” in *Springer Handbook of Electronic and Photonic Materials*, Springer, Cham, 2017, pp. 1–1.

[17] “The 3% Renewable Energy ‘Tipping Point’.,” *Debunk House*, 27-Jun-2017. .

[18] “How Solar Cells Work -- Components & Operation Of Solar Cells −.” How-solar-cells-work-components-operation-of-solar-cells.

[19] N. Yeh and P. Yeh, “Organic solar cells: Their developments and potentials,” *Renewable and Sustainable Energy Reviews*, vol. 21, pp. 421–431, May 2013.

[20] C. G. Bottenfield, F. Wei, H. J. Park, L. J. Guo, and G. Li, “Investigation of Printing-Based Graded Bulk-Heterojunction Organic Solar Cells,” *Energy Technology*, vol. 3, no. 4, pp. 414–422.

[21] C. W. Tang, “Two-layer organic photovoltaic cell,” *Appl. Phys. Lett.*, vol. 48, no. 2, pp. 183–185, Jan. 1986.

[22] N. S. Sariciftci, L. Smilowitz, A. J. Heeger, and F. Wudl, “Semiconducting polymers (as donors) and buckminsterfullerene (as acceptor): photoinduced electron transfer and heterojunction devices,” *Synthetic Metals*, vol. 59, no. 3, pp. 333–352, Aug. 1993.

[23] F. Zhang, D. Wu, Y. Xu, and X. Feng, “Thiophene-based conjugated oligomers for organic solar cells,” *J. Mater. Chem.*, vol. 21, no. 44, pp. 17590–17600, Nov. 2011.

[24] T. Ameri, G. Dennler, C. Lungenschmied, and C. J. Brabec, “Organic tandem solar cells: A review,” *Energy Environ. Sci.*, vol. 2, no. 4, pp. 347–363, Mar. 2009.

[25] G. Yu, J. Gao, J. C. Hummelen, F. Wudl, and A. J. Heeger, “Polymer Photovoltaic Cells: Enhanced Efficiencies via a Network of Internal Donor-Acceptor Heterojunctions,” *Science*, vol. 270, no. 5243, pp. 1789–1791, Dec. 1995.

[26] N. Marinova, S. Valero, and J. L. Delgado, “Organic and perovskite solar cells: Working principles, materials and interfaces,” *Journal of Colloid and Interface Science*, vol. 488, pp. 373–389, Feb. 2017.

[27] Meng, Lingxian, Yamin Zhang, Xiangjian Wan, Chenxi Li, Xin Zhang, Yanbo Wang, and Xin Ke, “Organic and solution-processed tandem solar cells with 17.3% efficiency,” *Science*, p. eaat2612, Aug. 2018.

[28] Bi, Yan-Gang, Jing Feng, Jin-Hai Ji, Fang-Shun Yi, Yun-Fei Li, Yue-Feng Liu, Xu-Lin Zhang, and Hong-Bo Sun, “Nanostructures induced light harvesting enhancement in organic photovoltaics,” *Nanophotonics*, vol. 7, no. 2, pp. 371–391, 2018.

[29] Kumaresan, Prabakaran, Sureshraju Vegiraju, Yamuna Ezhumalai, Shueh Lin Yau, Choongik Kim, Wen-Hsi Lee, and Ming-Chou Chen, “Fused-Thiophene Based Materials for Organic Photovoltaics and Dye-Sensitized Solar Cells,” *Polymers*, vol. 6, no. 10, pp. 2645–2669, Oct. 2014.

[30] V. I. Arkhipov, P. Heremans, and H. Bässler, “Why is exciton dissociation so efficient at the interface between a conjugated polymer and an electron acceptor?,” *Appl. Phys. Lett.*, vol. 82, no. 25, pp. 4605–4607, Jun. 2003.

[31] K. A. Mazzio and C. K. Luscombe, “The future of organic photovoltaics,” *Chem. Soc. Rev.*, vol. 44, no. 1, pp. 78–90, Dec. 2014.

[32] “Organic Photovoltaics (OPV) Tutorial,” *Sigma-Aldrich*.

[33] Wehenkel, DJ (Dominique), “Physical processes in organic solar cells.” Technische Universiteit Eindhoven, 2012.

[34] S. R. Cowan, A. Roy, and A. J. Heeger, “Recombination in polymer-fullerene bulk heterojunction solar cells,” *Phys. Rev. B*, vol. 82, no. 24, p. 245207, Dec. 2010.

[35] Scharber, M. C., D. Mühlbacher, M. Koppe, P. Denk, C. Waldauf, A. J. Heeger, and C. J. Brabec, “Design Rules for Donors in Bulk-Heterojunction Solar Cells—Towards 10 % Energy-Conversion Efficiency,” *Advanced Materials*, vol. 18, no. 6, pp. 789–794.

[36] Chen, Hsiang-Yu, Jianhui Hou, Shaoqing Zhang, Yongye Liang, Guanwen Yang, Yang Yang, Luping Yu, Yue Wu, and Gang Li, “Polymer solar cells with enhanced open-circuit voltage and efficiency,” *Nature Photonics*, vol. 3, no. 11, pp. 649–653, Nov. 2009.

[37] Guo, Xugang, Nanjia Zhou, Sylvia J. Lou, Jeremy Smith, Daniel B. Tice, Jonathan W. Hennek, and Rocío Ponce Ortiz, “Polymer solar cells with enhanced fill factors,” *Nature Photonics*, vol. 7, no. 10, pp. 825–833, Oct. 2013.

[38] Deshmukh, Kedar D., Rukiya Matsidik, Shyamal K. K. Prasad, Luke A. Connal, Amelia C. Y. Liu, Eliot Gann, Lars Thomsen, Justin M. Hodgkiss, Michael Sommer, and Christopher R. McNeill, “Tuning the Molecular Weight of the Electron Accepting Polymer in All-Polymer Solar Cells: Impact on Morphology and Charge Generation,” *Advanced Functional Materials*, vol. 28, no. 18, p. 1707185.

[39] J.-M. Nunzi, “Organic photovoltaic materials and devices,” *Comptes Rendus Physique*, vol. 3, no. 4, pp. 523–542, Jan. 2002.

[40] W. Shockley and H. J. Queisser, “Detailed Balance Limit of Efficiency of p-n Junction Solar Cells,” *Journal of Applied Physics*, vol. 32, no. 3, pp. 510–519, Mar. 1961.

[41] M. Muntwiler, Q. Yang, W. A. Tisdale, and X.-Y. Zhu, “Coulomb Barrier for Charge Separation at an Organic Semiconductor Interface,” *Phys. Rev. Lett.*, vol. 101, no. 19, p. 196403, Nov. 2008.

[42] L. Lu, T. Zheng, Q. Wu, A. M. Schneider, D. Zhao, and L. Yu, “Recent Advances in Bulk Heterojunction Polymer Solar Cells,” *Chem. Rev.*, vol. 115, no. 23, pp. 12666–12731, Dec. 2015.

[43] M. C. Scharber and N. S. Sariciftci, “Efficiency of bulk-heterojunction organic solar cells,” *Progress in Polymer Science*, vol. 38, no. 12, pp. 1929–1940, Dec. 2013.

[44] C. J. Brabec, S. E. Shaheen, C. Winder, N. S. Sariciftci, and P. Denk, “Effect of LiF/metal electrodes on the performance of plastic solar cells,” *Appl. Phys. Lett.*, vol. 80, no. 7, pp. 1288–1290, Feb. 2002.

[45] I. Etxebarria, J. Ajuria, and R. Pacios, “Solution-processable polymeric solar cells: A review on materials, strategies and cell architectures to overcome 10%,” *Organic Electronics*, vol. 19, pp. 34–60, Apr. 2015.

[46] M. Reyes-Reyes, K. Kim, and D. L. Carroll, “High-efficiency photovoltaic devices based on annealed poly(3-hexylthiophene) and 1-(3-methoxycarbonyl)-propyl-1-phenyl-(6,6)C61 blends,” *Appl. Phys. Lett.*, vol. 87, no. 8, p. 083506, Aug. 2005.

[47] M. Helgesen, R. Søndergaard, and F. C. Krebs, “Advanced materials and processes for polymer solar cell devices,” *J. Mater. Chem.*, vol. 20, no. 1, pp. 36–60, Dec. 2009.

[48] Fan, Qunping, Wenyan Su, Xia Guo, Bing Guo, Wanbin Li, Youdi Zhang, Kun Wang, Maojie Zhang, and Yongfang Li, “A New Polythiophene Derivative for High Efficiency Polymer Solar Cells with PCE over 9%,” *Advanced Energy Materials*, vol. 6, no. 14, p. 1600430, Jul. 2016.

[49] Svensson, M., F. Zhang, S. C. Veenstra, W. J. H. Verhees, J. C. Hummelen, J. M. Kroon, O. Inganäs, and M. R. Andersson, “High-Performance Polymer Solar Cells of an Alternating Polyfluorene Copolymer and a Fullerene Derivative,” *Advanced Materials*, vol. 15, no. 12, pp. 988–991.

[50] K. Müllen and W. Pisula, “Donor–Acceptor Polymers,” *J. Am. Chem. Soc.*, vol. 137, no. 30, pp. 9503–9505, Aug. 2015.

[51] H. A. M. van Mullekom, J. A. J. M. Vekemans, E. E. Havinga, and E. W. Meijer, “Developments in the chemistry and band gap engineering of donor–acceptor substituted conjugated polymers,” *Materials Science and Engineering: R: Reports*, vol. 32, no. 1, pp. 1–40, Feb. 2001.

[52] A. J. Heeger, “Semiconducting polymers: the Third Generation,” *Chem. Soc. Rev.*, vol. 39, no. 7, pp. 2354–2371, Jun. 2010.

[53] Wan, Qun, Xia Guo, Zaiyu Wang, Wanbin Li, Bing Guo, Wei Ma, Maojie Zhang, and Yongfang Li, “10.8% Efficiency Polymer Solar Cells Based on PTB7-Th and PC71BM via Binary Solvent Additives Treatment,” *Advanced Functional Materials*, vol. 26, no. 36, pp. 6635–6640.

[54] Z. Xiao, X. Jia, and L. Ding, “Ternary organic solar cells offer 14% power conversion efficiency,” *Science Bulletin*, vol. 62, no. 23, pp. 1562–1564, Dec. 2017.

[55] A. Facchetti, “Polymer donor–polymer acceptor (all-polymer) solar cells,” *Materials Today*, vol. 16, no. 4, pp. 123–132, Apr. 2013.

[56] J. Hou, O. Inganäs, R. H. Friend, and F. Gao, “Organic solar cells based on non-fullerene acceptors,” *Nature Materials*, vol. 17, no. 2, pp. 119–128, Jan. 2018.

[57] Lin, Yuze, Jiayu Wang, Zhi-Guo Zhang, Huitao Bai, Yongfang Li, Daoben Zhu, and Xiaowei Zhan, “An Electron Acceptor Challenging Fullerenes for Efficient Polymer Solar Cells,” *Advanced Materials*, vol. 27, no. 7, pp. 1170–1174.

[58] Ponomarev, A. N., M. E. Yudovich, V. A. Nikitin, D. V. Nikitin, V. T. Barchenko, V. N.

Sobol', K. B. Strel'nikov, N. A. Charykov, A. I. Myshkov, and V. I. Sergeev, "Some features of analysis of solutions of fullerenes C<Subscript>60</Subscript> and C<Subscript>70</Subscript> by their absorption spectra," *Opt. Spectrosc.*, vol. 88, no. 2, pp. 195–196, Feb. 2000.

[59] C.-Z. Li, H.-L. Yip, and A. K.-Y. Jen, "Functional fullerenes for organic photovoltaics," *J. Mater. Chem.*, vol. 22, no. 10, pp. 4161–4177, Feb. 2012.

[60] V. A. Trukhanov and D. Y. Paraschuk, "Non-fullerene acceptors for organic solar cells," *Polym. Sci. Ser. C*, vol. 56, no. 1, pp. 72–83, Sep. 2014.

[61] W. Chen and Q. Zhang, "Recent progress in non-fullerene small molecule acceptors in organic solar cells (OSCs)," *J. Mater. Chem. C*, vol. 5, no. 6, pp. 1275–1302, Feb. 2017.

[62] M. Jørgensen, K. Norrman, and F. C. Krebs, "Stability/degradation of polymer solar cells," *Solar Energy Materials and Solar Cells*, vol. 92, no. 7, pp. 686–714, Jul. 2008.

[63] E. M. Speller, "The significance of fullerene electron acceptors in organic solar cell photo-oxidation," *Materials Science and Technology*, vol. 33, no. 8, pp. 924–933, May 2017.

[64] A. Anctil, C. W. Babbitt, R. P. Raffaelle, and B. J. Landi, "Material and Energy Intensity of Fullerene Production," *Environ. Sci. Technol.*, vol. 45, no. 6, pp. 2353–2359, Mar. 2011.

[65] Li, Zhaojun, Xiaofeng Xu, Wei Zhang, Xiangyi Meng, Zewdneh Genene, Wei Ma, and Wendimagegn Mammo, "9.0% power conversion efficiency from ternary all-polymer solar cells," *Energy Environ. Sci.*, vol. 10, no. 10, pp. 2212–2221, Oct. 2017.

[66] E. Zhou, J. Cong, Q. Wei, K. Tajima, C. Yang, and K. Hashimoto, "All-Polymer Solar Cells from Perylene Diimide Based Copolymers: Material Design and Phase Separation Control," *Angewandte Chemie International Edition*, vol. 50, no. 12, pp. 2799–2803.

[67] T. Earmme, Y.-J. Hwang, N. M. Murari, S. Subramaniyan, and S. A. Jenekhe, "All-Polymer Solar Cells with 3.3% Efficiency Based on Naphthalene Diimide-Selenophene Copolymer Acceptor," *J. Am. Chem. Soc.*, vol. 135, no. 40, pp. 14960–14963, Oct. 2013.

[68] J. Yang, B. Xiao, A. Tang, J. Li, X. Wang, and E. Zhou, "Aromatic-Diimide-Based n-Type Conjugated Polymers for All-Polymer Solar Cell Applications," *Advanced Materials*, vol. 0, no. 0, p. 1804699.

[69] "Fig. 5 Chemical structures for P3HT, PBDTTT-C, PC 61 BM, and PC 71 BM.," *ResearchGate*.

[70] "THE ANALYSIS OF NUCLEAR MAGNETIC RESONANCE SPECTRA: III. PYRIDINE AND DEUTERATED PYRIDINES - Canadian Journal of Chemistry."

[71] L. E. Maley, "Application of gel permeation chromatography to high and low

molecular weight polymers," *Journal of Polymer Science Part C: Polymer Symposia*, vol. 8, no. 1, pp. 253–268, Jan. 1965.

[72] "Differential scanning calorimetry of polymers : physics, chemistry, analysis, technology (Book, 1994) [WorldCat.org]."

[73] Li, Heng, Meng Li, Lijun Zhang, Xiang Zhang, Yundi Ma, Bing Yu, Qiang Wei, and Shuhua Yin, "Dipyridylbenzene as a charming sensitizer to significantly enhance the photocatalytic activity of titanium dioxide," *Applied Catalysis B: Environmental*, vol. 232, pp. 472–480, Sep. 2018.

[74] B. W. D'Andrade, S. Datta, S. R. Forrest, P. Djurovich, E. Polikarpov, and M. E. Thompson, "Relationship between the ionization and oxidation potentials of molecular organic semiconductors," *Organic Electronics*, vol. 6, no. 1, pp. 11–20, Feb. 2005.

[75] "Understanding density functional theory (DFT) and completing it in practice: AIP Advances: Vol 4, No 12."

[76] H. P. Klug and L. E. Alexander, *X-Ray Diffraction Procedures: For Polycrystalline and Amorphous Materials, 2nd Edition*. 1974.

[77] G. Binnig, C. F. Quate, and C. Gerber, "Atomic Force Microscope," *Phys. Rev. Lett.*, vol. 56, no. 9, pp. 930–933, Mar. 1986.

[78] H. Benten, D. Mori, H. Ohkita, and S. Ito, "Recent research progress of polymer donor/polymer acceptor blend solar cells," *J. Mater. Chem. A*, vol. 4, no. 15, pp. 5340–5365, Apr. 2016.

[79] C. R. Newman, C. D. Frisbie, D. A. da Silva Filho, J.-L. Brédas, P. C. Ewbank, and K. R. Mann, "Introduction to Organic Thin Film Transistors and Design of n-Channel Organic Semiconductors," *Chem. Mater.*, vol. 16, no. 23, pp. 4436–4451, Nov. 2004.

[80] Guo, Xia, Chaohua Cui, Maojie Zhang, Lijun Huo, Ye Huang, Jianhui Hou, and Yongfang Li, "High efficiency polymer solar cells based on poly(3-hexylthiophene)/indene-C70 bisadduct with solvent additive," *Energy Environ. Sci.*, vol. 5, no. 7, pp. 7943–7949, Jun. 2012.

[81] Y. Lin and X. Zhan, "Non-fullerene acceptors for organic photovoltaics: an emerging horizon," *Materials Horizons*, vol. 1, no. 5, pp. 470–488, 2014.

[82] Chávez, Patricia, Ibrahim Bulut, Sadiara Fall, Olzhas Ibraikulov, Christos Chochos, Jérémy Bartringer, and Thomas Heiser, "An Electron-Transporting Thiazole-Based Polymer Synthesized Through Direct (Hetero)Arylation Polymerization," *Molecules*, vol. 23, no. 6, p. 1270, May 2018.

[83] Xie, Ruihao, Zhiming Chen, Yan Liu, Zhenfeng Wang, Zhongxin Chen, Lei Ying, Fei Huang, and Yong Cao, "Cross-conjugated n-type polymer acceptors for efficient all-polymer solar cells," *Chem. Commun.*, vol. 54, no. 18, pp. 2204–2207, Feb. 2018.

[84] W. Li, K. H. Hendriks, M. M. Wienk, and R. A. J. Janssen, "Diketopyrrolopyrrole Polymers for Organic Solar Cells," *Acc. Chem. Res.*, vol. 49, no. 1, pp. 78–85, Jan.

2016.

[85] “Small-Bandgap Polymer Solar Cells with Unprecedented Short-Circuit Current Density and High Fill Factor - Choi - 2015 - Advanced Materials - Wiley Online Library.”

[86] W. Li, Y. An, M. M. Wienk, and R. A. J. Janssen, “Polymer–polymer solar cells with a near-infrared spectral response,” *J. Mater. Chem. A*, vol. 3, no. 13, pp. 6756–6760, Mar. 2015.

[87] W. Li, W. S. C. Roelofs, M. Turbiez, M. M. Wienk, and R. A. J. Janssen, “Polymer Solar Cells with Diketopyrrolopyrrole Conjugated Polymers as the Electron Donor and Electron Acceptor,” *Advanced Materials*, vol. 26, no. 20, pp. 3304–3309, May 2014.

[88] H. D. Hoechstetter, “Heterocyclische verbindungen,” DE3918178A1, 06-Dec-1990.

[89] ong, Wei, Bin Sun, Chang Guo, Jonathan Yuen, Yuning Li, Shaofeng Lu, Chun Huang, and Antonio Facchetti, “Dipyrrolo[2,3-b:2′,3′-e]pyrazine-2,6(1H,5H)-dione based conjugated polymers for ambipolar organic thin-film transistors,” *Chem. Commun.*, vol. 49, no. 5, pp. 484–486, Dec. 2012.

[90] Q. Meng, Y. Sun, V. Ratovelomanana-Vidal, J. P. Genêt, and Z. Zhang, “CeCl3·7H2O: An Effective Additive in Ru-Catalyzed Enantioselective Hydrogenation of Aromatic α-Ketoesters,” *J. Org. Chem.*, vol. 73, no. 10, pp. 3842–3847, May 2008.

[91] D. Farran, I. Parrot, L. Toupet, J. Martinez, and G. Dewynter, “Transannular rearrangement of activated 2,5-diketopiperazines: a key route to original scaffolds,” *Org. Biomol. Chem.*, vol. 6, no. 21, pp. 3989–3996, Oct. 2008.

[92] Hong, Wei, Chang Guo, Yuning Li, Yan Zheng, Chun Huang, Shaofeng Lu, and Antonio Facchetti, “Synthesis and thin-film transistor performance of benzodipyrrolinone and bithiophene donor-acceptor copolymers,” *J. Mater. Chem.*, vol. 22, no. 41, pp. 22282–22289, Oct. 2012.

[93] “Fluorescent H-aggregates of an asymmetrically substituted mono-amino Zn(ii) phthalocyanine - Dalton Transactions (RSC Publishing).”

[94] Y. Li, P. Sonar, L. Murphy, and W. Hong, “High mobility diketopyrrolopyrrole (DPP)-based organic semiconductor materials for organic thin film transistors and photovoltaics,” *Energy Environ. Sci.*, vol. 6, no. 6, pp. 1684–1710, May 2013.

[95] Bijleveld, Johan C., Arjan P. Zoombelt, Simon G. J. Mathijssen, Martijn M. Wienk, Mathieu Turbiez, Dago M. de Leeuw, and René A. J. Janssen, “Poly(diketopyrrolopyrrole−terthiophene) for Ambipolar Logic and Photovoltaics,” *J. Am. Chem. Soc.*, vol. 131, no. 46, pp. 16616–16617, Nov. 2009.

[96] “PCE10 (PBDTTT-EFT),” *Ossila*..

[97] W. Ma, C. Yang, X. Gong, K. Lee, and A. J. Heeger, “Thermally Stable, Efficient Polymer Solar Cells with Nanoscale Control of the Interpenetrating Network Morphology,” *Advanced Functional Materials*, vol. 15, no. 10, pp. 1617–1622, Oct.

2005.

[98] Y. Wang, H. Benten, S. Ohara, D. Kawamura, H. Ohkita, and S. Ito, “Measurement of Exciton Diffusion in a Well-Defined Donor/Acceptor Heterojunction based on a Conjugated Polymer and Cross-Linked Fullerene Derivative,” *ACS Appl. Mater. Interfaces*, vol. 6, no. 16, pp. 14108–14115, Aug. 2014.

[99] G. Ren, E. Ahmed, and S. A. Jenekhe, “Non-Fullerene Acceptor-Based Bulk Heterojunction Polymer Solar Cells: Engineering the Nanomorphology via Processing Additives,” *Advanced Energy Materials*, vol. 1, no. 5, pp. 946–953, Oct. 2011.

[100] i, Gang, Vishal Shrotriya, Jinsong Huang, Yan Yao, Tom Moriarty, Keith Emery, and Yang Yang, “High-efficiency solution processable polymer photovoltaic cells by self-organization of polymer blends,” in *Materials for Sustainable Energy*, 0 vols., Co-Published with Macmillan Publishers Ltd, UK, 2010, pp. 80–84.

[101] “Role of balanced charge carrier transport in low band gap polymer:Fullerene bulk heterojunction solar cells - Kotlarski - 2011 - Journal of Polymer Science Part B: Polymer Physics - Wiley Online Library.”.

[102] C. Zhu and L. Fang, “Locking the Coplanar Conformation of π-Conjugated Molecules and Macromolecules Using Dynamic Noncovalent Bonds,” *Macromolecular Rapid Communications*, vol. 39, no. 2, p. 1700241, Jun. 2017.

[103] Z. Yan, B. Sun, and Y. Li, “Novel stable (3E,7E)-3,7-bis(2-oxoindolin-3-ylidene)benzo[1,2-b:4,5-b′]difuran-2,6(3H,7H)-dione based donor–acceptor polymer semiconductors for n-type organic thin film transistors,” *Chem. Commun.*, vol. 49, no. 36, pp. 3790–3792, Apr. 2013.

[104] Erb, T., U. Zhokhavets, G. Gobsch, S. Raleva, B. Stühn, P. Schilinsky, C. Waldauf, and C. J. Brabec, “Correlation Between Structural and Optical Properties of Composite Polymer/Fullerene Films for Organic Solar Cells,” *Advanced Functional Materials*, vol. 15, no. 7, pp. 1193–1196, Jul. 2005.

[105] H.-C. Liao, C.-C. Ho, C.-Y. Chang, M.-H. Jao, S. B. Darling, and W.-F. Su, “Additives for morphology control in high-efficiency organic solar cells,” *Materials Today*, vol. 16, no. 9, pp. 326–336, Sep. 2013.

[106] Schubert, Marcel, Brian A. Collins, Hannah Mangold, Ian A. Howard, Wolfram Schindler, Koen Vandewal, and Steffen Roland, “Correlated Donor/Acceptor Crystal Orientation Controls Photocurrent Generation in All-Polymer Solar Cells,” *Advanced Functional Materials*, vol. 24, no. 26, pp. 4068–4081, Jul. 2014.

[107] L. Huo and J. Hou, “Benzo[1,2-b:4,5-b′]dithiophene-based conjugated polymers: band gap and energy level control and their application in polymer solar cells,” *Polym. Chem.*, vol. 2, no. 11, pp. 2453–2461, Oct. 2011.

[108] Hou, Jianhui, Mi-Hyae Park, Shaoqing Zhang, Yan Yao, Li-Min Chen, Juo-Hao Li, and Yang Yang, “Bandgap and Molecular Energy Level Control of Conjugated Polymer Photovoltaic Materials Based on Benzo[1,2-b:4,5-b′]dithiophene,”

Macromolecules, vol. 41, no. 16, pp. 6012–6018, Aug. 2008.

[109] T. Lei, J.-H. Dou, and J. Pei, "Influence of Alkyl Chain Branching Positions on the Hole Mobilities of Polymer Thin-Film Transistors," *Advanced Materials*, vol. 24, no. 48, pp. 6457–6461, Dec. 2012.

[110] Fan, Qunping, Wenyan Su, Xia Guo, Yan Wang, Juan Chen, Chennan Ye, Maojie Zhang, and Yongfang Li, "Side-chain engineering for efficient non-fullerene polymer solar cells based on a wide-bandgap polymer donor," *J. Mater. Chem. A*, vol. 5, no. 19, pp. 9204–9209, May 2017.

[111] S. K. Hau, H.-L. Yip, and A. K.-Y. Jen, "A Review on the Development of the Inverted Polymer Solar Cell Architecture," *Polymer Reviews*, vol. 50, no. 4, pp. 474–510, Oct. 2010.

[112] Y. Li, "Molecular Design of Photovoltaic Materials for Polymer Solar Cells: Toward Suitable Electronic Energy Levels and Broad Absorption," *Acc. Chem. Res.*, vol. 45, no. 5, pp. 723–733, May 2012.

[113] S. C. Price, A. C. Stuart, L. Yang, H. Zhou, and W. You, "Fluorine Substituted Conjugated Polymer of Medium Band Gap Yields 7% Efficiency in Polymer−Fullerene Solar Cells," *J. Am. Chem. Soc.*, vol. 133, no. 12, pp. 4625–4631, Mar. 2011.

[114] Wang, Tao, Liuliu Feng, Jun Yuan, Lihui Jiang, Wei Deng, Zhi-Guo Zhang, Yongfang Li, and Yingping Zou, "Side-chain fluorination on the pyrido[3,4-b]pyrazine unit towards efficient photovoltaic polymers," *Sci. China Chem.*, vol. 61, no. 2, pp. 206–214, Feb. 2018.

[115] M. Liu, Y. Gao, Y. Zhang, Z. Liu, and L. Zhao, "Quinoxaline-based conjugated polymers for polymer solar cells," *Polym. Chem.*, vol. 8, no. 32, pp. 4613–4636, Aug. 2017.

[116] N. Aoyagi, B. Ochiai, H. Mori, and T. Endo, "Mild and Efficient One-Step Synthesis of Trithiocarbonates Using Minimum Amount of CS2," *Synlett*, vol. 2006, no. 4, pp. 636–638, Mar. 2006.

[117] R. K. Verma, G. K. Verma, K. Raghuvanshi, and M. S. Singh, "An expedient route to highly functionalized 2H-chromene-2-thiones via ring annulation of β-oxodithioesters catalyzed by InCl3 under solvent-free conditions," *Tetrahedron*, vol. 67, no. 3, pp. 584–589, Jan. 2011.

[118] B. J. Ramulu, A. Nagaraju, S. Chowdhury, S. Koley, and M. S. Singh, "Metal-Free Reagent Dependent S S and C C Homocoupling of α-Enolic Dithioesters at Room Temperature: Direct Access to Fully Substituted Symmetrical Thiophenes via Chemoselective Paal–Knorr Approach," *Advanced Synthesis & Catalysis*, vol. 357, no. 2–3, pp. 530–538, Feb. 2015.

[119] "Synthesis of New Pyridazine-Based Monomers and Related Polymers for Photovoltaic Applications - Gendron - 2010 - Macromolecular Rapid Communications

- Wiley Online Library."

[120] J. W. Slater, D. P. Lydon, N. W. Alcock, and J. P. Rourke, "Doubly Cyclometalated Pyridazines: Contrasting Behavior with Palladium and Platinum," *Organometallics*, vol. 20, no. 21, pp. 4418–4423, Oct. 2001.

[121] "A meso-Helical Coordination Polymer from Achiral Dinuclear [Cu2(H3CCN)2(μ-pydz)3][PF6]2 and 1,3-Bis(diphenylphosphanyl)propane—Synthesis and Crystal Structure of $\rm{^{1}_{\infty }}${[Cu(μ-pydz)2][PF6]} (pydz=pyridazine)," *Chemistry – A European Journal*, vol. 7, no. 18, pp. 4007–4011, Sep. 2001.

[122] H.-Y. Chen, J. Hou, A. E. Hayden, H. Yang, K. N. Houk, and Y. Yang, "Silicon Atom Substitution Enhances Interchain Packing in a Thiophene-Based Polymer System," *Advanced Materials*, vol. 22, no. 3, pp. 371–375, Jan. 2010.

[123] Duan, Ruomeng, Long Ye, Xia Guo, Ye Huang, Peng Wang, Shaoqing Zhang, Jianping Zhang, Lijun Huo, and Jianhui Hou, "Application of Two-Dimensional Conjugated Benzo[1,2-b:4,5-b′]dithiophene in Quinoxaline-Based Photovoltaic Polymers," *Macromolecules*, vol. 45, no. 7, pp. 3032–3038, Apr. 2012.

[124] M. Lu, W. Wang, L. Liang, S. Yan, and Q. Ling, "Synthesis of D–A low-bandgap polymer-based thieno[3,4-b]pyrazine and benzo[1,2-b:4,5-b′]dithiophene for polymer solar cells," *Polym. Bull.*, vol. 74, no. 2, pp. 603–614, Feb. 2017.

[125] J. L. Brédas, G. B. Street, B. Thémans, and J. M. André, "Organic polymers based on aromatic rings (polyparaphenylene, polypyrrole, polythiophene): Evolution of the electronic properties as a function of the torsion angle between adjacent rings," *J. Chem. Phys.*, vol. 83, no. 3, pp. 1323–1329, Aug. 1985.

[126] Schulz, Gisela L, Marta Urdanpilleta, Roland Fitzner, Eduard Brier, Elena Mena-Osteritz, Egon Reinold, and Peter Bäuerle. "Optimization of solution-processed oligothiophene:fullerene based organic solar cells by using solvent additives," *Beilstein J Nanotechnol*, vol. 4, pp. 680–689, Oct. 2013.

[127] P. Schilinsky, U. Asawapirom, U. Scherf, M. Biele, and C. J. Brabec, "Influence of the Molecular Weight of Poly(3-hexylthiophene) on the Performance of Bulk Heterojunction Solar Cells," *Chem. Mater.*, vol. 17, no. 8, pp. 2175–2180, Apr. 2005.

[128] Ding, Z., J. Kettle, M. Horie, S. W. Chang, G. C. Smith, A. I. Shames, and E. A. Katz, "Efficient solar cells are more stable: the impact of polymer molecular weight on performance of organic photovoltaics," *J. Mater. Chem. A*, vol. 4, no. 19, pp. 7274–7280, May 2016.